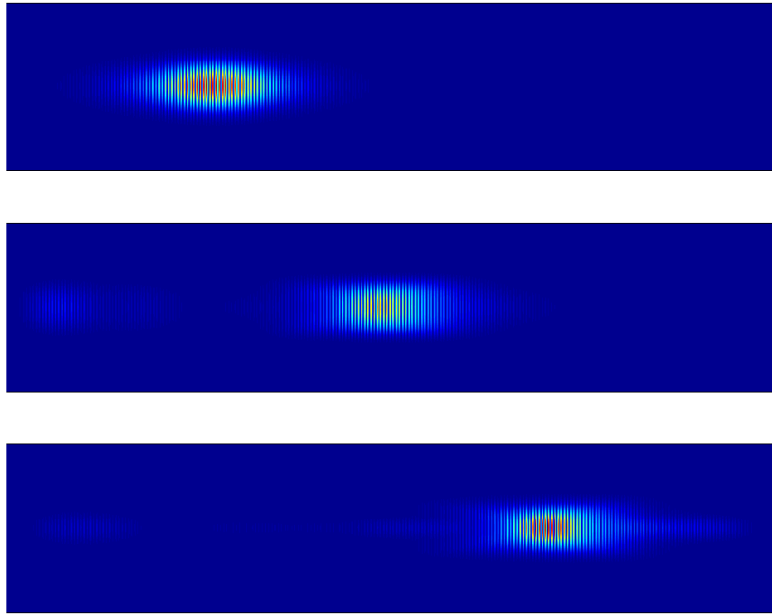


Coherent Momentum State Manipulation of Matter Waves



Dissertation der Fakultät für Physik
der
Ludwig-Maximilians-Universität München

vorgelegt von
Sierk Pötting

München, den 01. Juni 2004

1. Gutachter: Prof. H. Walther
 2. Gutachter: Prof. A. Schenzle
- Tag der mündlichen Prüfung: 20. Dezember 2004

For Tessa and our little son Oskar

Abstract

This dissertation presents a theoretical analysis of methods to manipulate and control the momentum state of coherent matter waves. Of particular interest is the coherent acceleration of a quantum-degenerate atomic system, which, as a direct consequence of the form of the de Broglie wavelength, results in tunable source of matter waves. Such sources are of considerable importance for a number of potential applications in the field of atom optics, including the development of highly sensitive gyroscopes, accelerometers, gravity gradiometers or atom lithography and holography, as well as for potential uses in integrated atom optics.

Our basic setup consists of a Bose-Einstein condensate in a moving optical lattice created by a pair of frequency-chirped counterpropagating laser beams acting as a “conveyor belt” for ultracold atoms. Whereas the acceleration of ultracold but non-condensed atoms in such a lattice was demonstrated earlier, we extend this scheme to the case of Bose-Einstein condensates.

As a first step, we investigate the acceleration efficiency for various acceleration rates and nonlinear interaction strengths. We find parameter regimes where efficient acceleration is possible, i.e. all atoms are accelerated to the same velocity and the initially sharp momentum distribution and thus its monochromaticity is preserved. However, in general we identify switch-on effects of the lattice, dynamical loss and nonlinear effects to be responsible for deterioration of the monochromaticity of the condensate: On the one hand, switch-on effects and dynamical loss induce a coupling of the initially populated momentum mode to other modes, thereby distributing the momentum over several modes. On the other hand, the nonlinear release of mean field energy during the acceleration process causes the mode profile itself to broaden, also leading to a contamination of the initial monochromaticity.

As a second step, we discuss ways to improve this scheme by removing the restriction of constant accelerations. We employ genetic algorithms to optimize the time-dependent motion of the lattice. We show that with such flexibility, it is possible to achieve a fast and highly efficient coherent acceleration of condensates, even when mean-field effects cannot be neglected. The same scheme also enables the creation of arbitrary coherent superposition states in momentum space. The technique is thus suitable for building highly efficient momentum state beam splitters.

In addition to simply accelerating condensates, it is desirable for many potential applications to transport atomic wave packets without dispersion over large distances. This can be achieved by launching bright atomic solitons, where the effects of the nonlinearity counterbalance the dispersion. Placing a Bose-Einstein condensate with repulsive interactions in a lattice, one can create a negative effective mass. Under these circumstances bright and stable soliton solutions exist, so-called *gap solitons*. After a careful analysis of the soliton properties, we use the tools we developed for condensate acceleration and demonstrate two feasible schemes to excite the solitons.

Experimental data released after publication of our results demonstrating the acceleration of Bose-Einstein condensates in moving lattices [1, 2] and the very recent observation of atomic gap solitons [3] indicates that our theoretical analysis

was timely and indeed experimentally feasible.

As an outlook, we briefly comment on a new direction in the field of atom optics that holds promise for future applications: the use of quantum degenerate Fermi gases. In atomic as well as in optical physics one often encounters situations where there exists a coupling between several modes of a system. Here, we illustrate the “toy model” of a fermionic coupler where transitions between two internal states are induced by Raman coupling. Due to Fermi statistics and interatomic interactions, this is a simple example of a nonlinear multimode coupler. Investigation of this system consisting of only a few fermions already clearly illustrates the basic differences between bosonic and fermionic dynamics and sheds light on the role of two-body collisions. Understanding the basic mechanisms of this system is a first step towards more sophisticated coherent control of fermionic systems.

Zusammenfassung

In der vorliegenden Arbeit berichten wir über theoretische Analysen zur Manipulation und Steuerung des Impulszustandes von kohärenten Materiewellen. Insbesondere betrachten wir die Möglichkeit, Bose-Einstein Kondensate kohärent zu beschleunigen, was uns ermöglicht, die de Broglie Wellenlänge der Materiewelle zu wählen. Diese einstellbaren kohärenten Atomstrahlquellen versprechen großen Nutzen in einer Vielzahl von Anwendungen, z.B. beim Einsatz in integrierten Atomensoren.

Wir betrachten ein Bose-Einstein Kondensat in einem sich räumlich bewegenden optischen Gitter. Zunächst untersuchen wir die Beschleunigungsdynamik für verschiedene konstante Beschleunigungsraten des Gitters und unterschiedliche Mean-Field-Energien des Kondensats. Wir identifizieren dynamische Verlustprozesse und nichtlineare Effekte, die zu einer Verbreiterung der anfänglich sehr scharfen Impulsverteilung führen und somit den monochromatischen Charakter bzw. die Kohärenz des Kondensats vermindern. Der Parameterbereich, in dem das gesamte Kondensat effizient beschleunigt werden kann, ist eingeschränkt. Deswegen betrachten wir im nächsten Schritt komplexe zeitabhängige Bewegungen des optischen Gitters, die nicht nur zu einer konstanten Beschleunigung führen. Mit Hilfe so genannter *Genetischer Algorithmen* optimieren wir diese zusätzlichen Freiheitsgrade des Gitters, so dass Kondensate mit hohen Mean-Field-Energien schnell und effizient beschleunigt werden können. Zusätzlich zeigen wir, dass dieses Verfahren zur Generierung von beliebigen kohärenten Superpositionen von Impulsmoden genutzt werden kann. Dieses ermöglicht u.a. die Konstruktion von nichtlinearen Atomstrahlteilern. Außer der Beschleunigung von Kondensaten ist es oft wünschenswert, atomare Wellenpakete ohne Dispersion über weite Strecken zu transportieren. Wir zeigen, dass in unserem System die Möglichkeit besteht, helle atomare *Gap Solitonen* zu erzeugen. Durch das periodische Gitter kann man dem Kondensat eine negative effektive Masse zuschreiben, deren dispersive Wirkung durch die repulsive interatomare Wechselwirkung ausbalanciert wird. Wir untersuchen detailliert die Eigenschaften der Gap Solitonen und entwickeln Methoden zur Anregung, die auf den Ergebnissen der zuvor dargestellten optimierten Beschleunigung von Kondensaten basieren.

Nach der Veröffentlichung unserer Analysen wurden experimentelle Ergebnisse bekannt, die sowohl die Beschleunigung von Bose-Einstein Kondensaten in optischen Gittern als auch die Anregung von Gap Solitonen zeigen. Dies deutet darauf hin, dass unsere theoretischen Ansätze zur rechten Zeit ein Gebiet von hohem praktischen Interesse beleuchtet haben.

In einem abschließenden Ausblick betrachten wir kurz entartete Fermi Gase, die ein neuer Forschungsschwerpunkt in der Atomoptik sind. Da sowohl in der Atomphysik als auch in der Optik gekoppelte Systeme häufig eine fundamentale Rolle spielen, untersuchen wir die Dynamik von zwei gekoppelten internen Zuständen eines kalten Fermi Gases in einer harmonischen Falle. Auf Grund von Fermi-Statistik und Stoßprozessen zwischen den Atomen handelt es sich hierbei um eine einfache Version eines nichtlinearen Vielmoden-Kopplers. Ein Grundverständnis

der Dynamik dieses Systems ist ein wichtiger Schritt, Methoden zur gezielten, kohärenten Manipulation von fermionischen Systemen zu entwickeln.

Contents

1	Introduction	1
1.1	Recent developments	2
1.1.1	Coherent atomic sources: Atom lasers	2
1.1.2	Atomic waveguides	3
1.1.3	Atomic sensors	5
1.2	Dissertation work	7
1.2.1	Motivation and overview	7
1.2.2	Publications	8
2	The Model System	9
2.1	Stationary Gross-Pitaevskii equation	9
2.2	Ground state properties	11
2.2.1	Thomas-Fermi approximation	11
2.2.2	Gaussian variational calculation	12
2.3	Time-dependent Gross-Pitaevskii equation	13
2.3.1	Reduction to one dimension	14
2.4	Optical lattices	15
2.4.1	Laser geometry	15
2.4.2	Lattice potential	15
2.4.3	Recoil units	18
2.5	Periodic potentials and band structure	18
2.5.1	Dispersion curve	19
2.5.2	Atomic motion in the lattice	19
2.5.3	Bloch oscillations	22
2.5.4	Landau-Zener tunneling	22
3	Acceleration in Optical Lattices	25
3.1	Accelerated optical lattice	26
3.2	Classical point particles	27
3.3	Bloch oscillations of ultracold atoms	28
3.4	Condensate acceleration	30
3.4.1	Quasimodes	33
3.4.2	Sequential Bragg resonances	34
3.5	Loss mechanisms in condensate acceleration	36
3.5.1	Initial loss: Sudden lattice switch-on	36
3.5.2	Dynamical loss	37
3.6	Nonlinear effects	39
3.7	Recent experiments	39

4	Optimized Acceleration	43
4.1	Genetic algorithms	43
4.1.1	The control parameter	44
4.1.2	The mating operators	46
4.1.3	Randomness in offspring production	47
4.1.4	Operator selection	47
4.2	Optimized coherent acceleration	48
4.3	Coherent superposition engineering	50
5	Dispersion-free Transport: Gap Solitons	55
5.1	Introduction to atomic solitons	56
5.1.1	Dark atomic solitons	56
5.1.2	Bright atomic solitons	58
5.2	Momentum state gap solitons	58
5.2.1	Coupled-mode equations	59
5.2.2	Solitary wave solutions	60
5.2.3	Gap soliton properties	61
5.2.4	Multiple scales solutions	65
5.3	Numerical propagation studies	67
5.3.1	Propagation in one dimension	67
5.3.2	Propagation in three dimensions	67
5.4	Excitation of gap solitons	73
5.4.1	Bragg pulse excitation	73
5.4.2	Genetic algorithm excitation	74
6	Outlook: Fermions	79
6.1	Degenerate Fermi gases	79
6.1.1	Cooling of fermions	79
6.1.2	The BCS-BEC crossover	80
6.2	The fermionic Raman coupler	81
6.2.1	The model system	81
6.2.2	Equations of motion	82
6.3	Linear dynamics	83
6.4	Collisions	84
6.4.1	Fermions	86
6.4.2	Bosons	87
7	Summary and Conclusion	93
A	Numerical Methods	95
A.1	Discretization	95
A.2	Nonlinear ground state method	96
A.3	Split-operator method	97
A.4	Split-operator method for one-dimensional GPE	98
A.5	Finite-difference scheme for cylindrical symmetry	99
B	Details of Genetic Algorithm	101
C	Method of Multiple Scales	105
C.1	Properties of the linear eigensolutions	105
C.2	Nonlinear envelope equation	105
C.3	General soliton solution	108
C.4	Stationary soliton solution	108
D	Complete list of publications	109

CONTENTS

ix

Curriculum vitae

121

Acknowledgments

123

Chapter 1

Introduction

One of the most striking features of quantum mechanics is the wave-like character of massive particles. It was first noticed by de Broglie that not only light, but all matter should be regarded as waves, with the so-called de Broglie wavelength $\Lambda = h/p$, where p is the particle momentum [4]. This groundbreaking result enabled the transfer of concepts from wave optics with light to the domain of massive particles. This led to the development of the field of de Broglie optics [5], that describes the propagation, reflection, refraction, diffraction and interference of matter waves.

In contrast to the subfields of electron optics [6] and neutron optics [7] with well-established applications such as e.g. electron microscopy and neutron interferometry, we focus on particle waves consisting of neutral atoms. The breakthrough in this field of *atom optics* was sparked by the rapid progress in laser cooling over the past twenty years [8]. The decrease of the momentum of the atoms by controlling the atomic motion by laser light eliminated problems associated with the small de Broglie wavelength of atoms at room temperature. Subsequently, many atom-optical elements, including mirrors, gratings, resonators and interferometers were successfully demonstrated.

Another milestone was then reached by the achievement of Bose-Einstein condensation in dilute gases of neutral atoms [9, 10, 11], where a macroscopic quantum object with an extremely narrow momentum spread is created in the ground state of a trap. Coherent extraction of atoms from trapped condensates led to the matter wave equivalent of the optical laser, the *atom laser* [12, 13, 14, 15]. These sources of monochromatic matter waves are bright and enabled the transition from linear to nonlinear atom optics due to the intrinsic many-body interactions within the condensate. First experiments were carried out soon after the first successful condensation, demonstrating that many concepts known from nonlinear optics have indeed a matter wave equivalent, such as e.g. atomic four-wave mixing [16], phase-coherent amplification [17, 18], dark atomic solitons [19, 20] and matter wave superradiance [21].

Despite many similarities between optical and atom optical concepts, there are also differences. The most obvious one is that in atom optics the conventional roles of light and matter are reversed. Specifically, in atom optics, light is usually used to control and manipulate atomic trajectories and the quantum state. More profound, however, are the structural differences between photons and atoms: Atoms, in contrast to photons, are e.g. massive particles, they exhibit a rich internal structure, they possess a magnetic moment and a specific polarizability, and are thus sensitive to many external fields. These properties allow for excellent manipulation and custom-tailored control of atomic matter waves.

Current research tries to harness these exceptional properties in order to move the field of atom optics towards applications. A major goal is to build compact

atomic interferometric devices that outperform state-of-the-art optical sensors. Single components to reach this ambitious goal have already successfully been tested: On the one hand, free-space atom optical sensors - based on atomic interference - were shown to be able to compete with state-of-the-art optical devices [22]. On the other hand, the increased need to control samples of atoms in confined geometries led to the successful guiding of ultracold atoms as well as of Bose-Einstein condensates on lithographically fabricated magnetic waveguides [23, 24, 25, 26, 27]. The current challenge is to seamlessly combine these various approaches, since highly sensitive waveguide interferometers with bright and coherent atomic sources still remain to be demonstrated.

Besides sensor applications, a variety of other fields can benefit substantially from the manipulation of quantum degenerate atomic wave packets or beams with finely tuned potentials. In some of these fields, new applications are based on the substitution of laser light by atomic de Broglie waves. Tuning the velocity of a beam of condensed atoms leads to a tunable source of de Broglie waves. These are expected to overcome the limitations of conventional laser light when used e.g. in atomic lithography [28, 29] or even in proposed schemes for atomic holography [30]. Other fields, such as quantum information processing and computation, exploit properties that are unique to coherent matter. Among those applications that do not have a counterpart in quantum optics, one finds newly developed and very promising schemes for quantum computation, where controlled collisions between atoms in neighboring sites of an optical lattice are used to generate multi-particle entanglement [31, 32].

In the following Section 1.1 we briefly review the basic building blocks on the road towards microfabricated atomic sensors. This serves the purpose of conveying a deeper understanding of these topics so that in Section 1.2, the dissertation work and its outline can be embedded into this context. In particular, we summarize the concepts of the atom laser in Section 1.1.1, give an overview over atomic waveguides in Section 1.1.2, and introduce the basic principles of atomic sensors in Section 1.1.3.

1.1 Recent developments

1.1.1 Coherent atomic sources: Atom lasers

Although the idea of an atom laser as a source of coherent matter waves has been investigated before the demonstration of Bose-Einstein condensation [33, 34, 35], the experimental pursuit became practical only after the availability of condensates. This is due to the fact that the main prerequisite for a laser is readily fulfilled after the condensation: The condensate in the trap is a macroscopically populated single quantum state and thus the stimulated emission - as needed in optical lasers to transfer many photons into a single cavity mode - is taken care of by the condensation procedure. The remaining step towards a working atom laser is an output coupler that coherently extracts atoms from the trap. Since the condensate atoms all have the same energy and hence the same de Broglie wavelength, the resulting beam of matter waves is expected to be monochromatic. For atoms, monochromaticity means that the momentum spread of the beam is narrow so that the beam is highly directional and propagates without much spreading. In terms of coherence, monochromaticity is equivalent to first-order coherence [36, 37]. Just as most applications of optical lasers rely solely on this degree of coherence, it is also expected to be sufficient for many applications of atom lasers, including atomic interferometers that will be described in Section 1.1.3.

The first atom laser was demonstrated by the MIT group [12], where the output coupler was realized by inducing spin-flips from magnetically trapped to untrapped

states. Gravity then accelerated the extracted atoms away from the trap, as shown in Fig. 1.1(a). In order to compensate for variations of the frequency needed to flip the spins, caused by fluctuations of the confining magnetic field, the rf-field was pulsed on a time scale short compared to these fluctuations. The pulsed nature of the output coupler limited the coherence length of the atomic beam to the coherence length of the condensate. An improvement of this scheme is described in Ref. [15], where stabilization of the magnetic trapping field allows for a continuous extraction of atoms, as can be seen in Fig. 1.1(b). Measurements showed that this CW-outcoupling indeed preserved the spatial coherence. The coherence length was determined to be on the order of several millimeters [38]. Reference [14] followed a slightly different approach in building an output coupler by using pulsed optical Raman transitions to transfer atomic population from trapped to untrapped states. Choosing the angle between the two Raman lasers gives the possibility of varying the imparted momentum to the atoms between 0 and $2n\hbar k_L$, with n the order of the Raman process and k_L the wave vector of the laser. In this way it is possible to choose the de Broglie wavelength of the matter wave beam, resulting in a widely tunable atom laser. Furthermore, the pulse sequence can be arranged so that the released wave packets strongly overlap and the extraction is quasi-continuous, as illustrated in Fig. 1.1(c). A fourth type of atom laser, as described in Ref. [13], is essentially an example of a mode-locked atom laser. A Bose-Einstein condensate is trapped in an optical lattice under the influence of gravity. This tilted lattice potential is shallow enough for atoms to tunnel out of the individual potential wells. Since the condensate covers several lattice sites, the extracted atoms are phase-coherent but differ by the gravitational energy separation between the wells. Such a comb of signals in the frequency domain results in a train of short pulses in the time domain. Figure 1.1(d) shows a snapshot of such a train of equidistant pulses. Subsequently, experiments with atom lasers were successfully carried out, demonstrating reflection, focusing and storage of an atomic laser beam in a resonator [39]. Furthermore, Ref. [40] describes the construction of a continuous source of Bose-Einstein condensed atoms, that could be combined with CW-outcoupling in order to create a truly continuous atom laser.

1.1.2 Atomic waveguides

After many trap configurations for neutral atoms had been developed, it was a logical step to move from free-space atom optics towards controlled guiding of atoms in confined geometries. Based on the success of optical fibers and microfabricated waveguides, efforts were launched to develop similar devices for neutral atoms. First concepts were based on hollow core fibers, where either the red-detuned center of the fundamental mode [41] or the blue-detuned evanescent fields on the inner walls of the fiber guided the atoms [42]. Successful guiding involving both schemes was demonstrated in Refs. [43, 44, 45, 46]. Another group used a hollow core fiber with current carrying wires arranged around the core so that the magnetic field guided the atoms in the center of the fiber [47]. The major breakthrough in guiding neutral atoms then came with the use of lithographically patterned current-carrying wires, so-called *atom chips*. As in free-space magnetic traps, atoms with a magnetic quantum number m_F interacting with a magnetic field $\mathbf{B}(\mathbf{r})$ experience a potential

$$V(\mathbf{r}) = m_F g_F \mu_B \cdot \mathbf{B}(\mathbf{r}), \quad (1.1)$$

with μ_B the Bohr magneton and g_F the g -factor. Weak-field seeking atoms, with $m_F g_F > 0$, are attracted towards the minimum of the potential. In contrast to free-space atom optics or hollow core fiber waveguides, the guiding potential is now generated by wires that can basically be placed in arbitrary patterns on the sub-

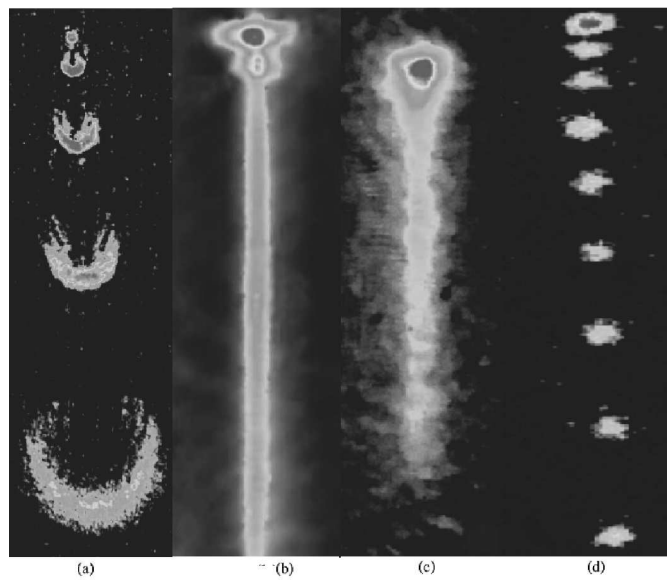


Figure 1.1: Output of different atom lasers based on extraction of atoms from Bose-Einstein condensates: (a) *MIT laser* [12] based on pulsed rf-induced spin-flips; (b) *Munich laser* [15] based on continuous rf-induced spin-flips; (c) *NIST laser* [14] based on pulsed optical Raman transitions; (d) *Yale laser* [13] based on tunneling in an optical lattice. The atoms are extracted from condensates shown at the top, the coherent atomic beams travel downwards.

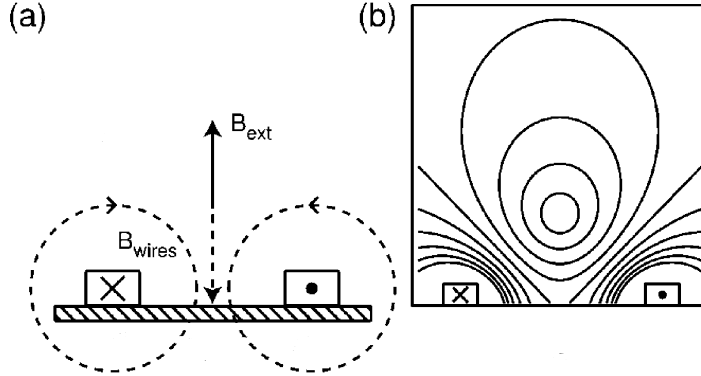


Figure 1.2: Two-wire magnetic atom waveguide: (a) The currents in the two wires are in opposite directions, each creating a spherical magnetic field B_{wires} centered around the wires; additionally, an external magnetic field B_{ext} is applied. (b) The resulting potential exhibits a minimum between the two wires where the atoms can be guided. Due to the external magnetic field the potential minimum is shifted away from the substrate. Schematic from Ref. [24].

strate. Figure 1.2 shows schematically how current-carrying wires generate a guiding potential for weak-field seeking atoms. The lithographical fabrication process enables the design of a broad variety of potentials, custom-tailored to applications, such as e.g. miniature quadrupole and Ioffe-Pritchard traps, magnetic lattices, interferometers, storage rings, etc. [48]. Furthermore, these devices occupy very little space and are fairly robust against external disturbances.

At first, experiments have been carried out with ultracold but non-condensed atoms, among those the demonstration of transport and merging clouds of atoms with the help of a conveyor belt potential [25]. Then, Bose-Einstein condensates have been created directly on the atom chips [26, 27]. By now, it became almost a standard procedure to guide condensates in miniature waveguides.

A possible drawback of substrate-based magnetic waveguides is the interaction of the cold atoms with the nearby *hot* surface [49]. Indeed, Ref. [50] measured the fragmentation of trapped condensates caused by spatial fluctuations of surface currents and confirmed radio-frequency spin-flip transitions due to surface noise predicted in Ref. [51]. However, since the disturbing fluctuations are mainly of technical nature and they decrease with increasing distance of the cloud to the surface, they can successfully be suppressed. As a consequence, it was recently found that decoherence is indeed not an issue, and coherent manipulation of internal states of neutral atoms in a magnetic microchip trap was demonstrated [52, 53].

The development of microfabricated waveguides for ultracold atoms may not only lead to various new applications, reaching from sensor applications and integrated atomic clocks to controlled quantum information processing. It might also prove useful in the study of fundamental issues requiring tightly confined one-dimensional potential, such as e.g. needed for the realization of a Tonks-Girardeau gas [54, 55, 56].

1.1.3 Atomic sensors

The use of integrated optical sensors has grown rapidly over the past years, since they offer new abilities, compact sizes and most often superior performance [57]. In

this section, we show that the use of matter waves instead of light is even more promising for future sensor applications due to a potential increase in sensitivity.

Common sensors based on interferometry rely on the detection of a phase difference created between two paths of the interferometer. This phase shift is caused by the interaction with the external field that is to be probed. For illustration purposes, we consider a Mach-Zehnder interferometer shown in Figure 1.3 as a basic setup. An initial atomic wave function ψ_0 is coherently split into two parts ψ_1 and ψ_2 that evolve along the two interferometer paths. At a second beam splitter they are then combined and detected. A 50% beam splitter leads to outgoing wave functions $\psi_{\pm} = 2^{-1/2}(\psi_1 \pm \psi_2)$. Writing the stationary wave functions in terms of amplitude and phase,

$$\psi_i(\mathbf{r}) \approx A_i e^{i\phi_i(\mathbf{r})}, \quad (1.2)$$

with $i = 1, 2$ and $A_i, \phi_i(\mathbf{r})$ real-valued, we evaluate the atomic density at the detectors to

$$|\psi_{\pm}|^2 \propto 1 \pm \cos(\Delta\phi), \quad (1.3)$$

where we assumed $A_1 = A_2$. The phase difference accumulated by the wave functions along the two interferometer paths is denoted by $\Delta\phi = \phi_2 - \phi_1$. Using the WKB approximation of the stationary Schrödinger equation, i.e. the quantum mechanical version of Hamilton's ray optics, one finds the phase difference $\Delta\phi$ to be proportional to the difference of the classical actions accumulated along the two paths [5, 36]. The WKB approximation is valid for weak perturbations and enables us to explicitly calculate the phase difference for various external fields.

For illustration purposes we consider an interferometer sensitive to rotations. As shown in Fig. 1.3 we assume the interferometer to rotate at a constant frequency Ω . The phase difference created in these *gyroscopes* is due to the fact that in one arm of the interferometer the atoms are copropagating with the rotation, in the other arm they are counterpropagating. This phase shift is the so-called *Sagnac effect*. For the atomic case, the phase shift in the WKB approximation is given by $\Delta\phi_a = 2M\Omega A/\hbar$ [5], with M the mass of the atoms and A the area enclosed by the interferometer loop. In an optical fiber gyroscope with light of wavelength λ and frequency ω , the Sagnac shift is evaluated to $\Delta\phi_o = 8\pi\Omega A/\lambda c$, with c the speed of light [57]. The ratio between the atomic and optical case is then

$$\frac{\Delta\phi_a}{\Delta\phi_o} \propto \frac{Mc^2}{\hbar\omega}. \quad (1.4)$$

Mainly due to the atomic mass, this ratio is typically on the order of 10^{11} . This means that, assuming everything else being equal, matter wave rotation sensors are more sensitive than optical fiber gyroscopes by roughly eleven orders of magnitude. However, besides the fact that optical fiber gyroscopes usually enclose a much larger area, matter wave sensors are suspected to suffer seriously from decoherence, reducing the staggering factor of 10^{11} . Nonetheless, the demonstration of an atomic gyroscope that performed as well as its state-of-the-art optical counterpart [58] shows that further research in atomic sensors might be fertile. Furthermore, there are applications that are unique to atomic sensors, since atoms interact with the environment in different ways than photons. An example for this is the demonstration of a gravity gradiometer [59], that is based on the acceleration of the atomic mass.

Possible future improvements of matter wave sensors include the use of bright and monochromatic atom lasers as a source of matter waves as well as the construction of squeezed states in order to achieve maximum sensitivity.

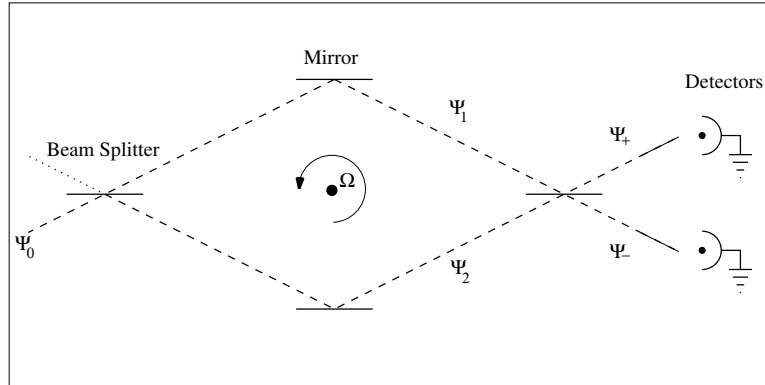


Figure 1.3: Schematic of a Mach-Zehnder interferometer. For illustration purposes the setup is assumed to rotate at a frequency Ω , the axis of rotation being oriented perpendicular to the plane of the interferometer.

1.2 Dissertation work

1.2.1 Motivation and overview

A basic requirement to successfully combine atom lasers and microfabricated waveguides to sensitive atom interferometers is the control of the atomic momentum. There are several reasons why coherent manipulation of the momentum state is an inevitable tool to achieve this:

- Changing the momentum state of the atom laser beam and thus changing its de Broglie wavelength makes it a tunable source of coherent atoms. In particular, controlled acceleration and deceleration of the atomic beam is necessary to impart the appropriate momentum.
- Controlling the momentum state supports efficient guiding on the microfabricated chips and can reduce loss due to tunneling out of the guiding potential.
- Engineering of arbitrary phase-dependent momentum state superpositions enables the shaping of non-dispersive wave packets (such as momentum state solitons) or the construction of highly efficient beam splitters for interferometers.

In this dissertation we propose various approaches that provide the desired momentum state control. We focus on techniques that are robust, experimentally feasible and preserve the monochromaticity of the atom beam or wave packet. Furthermore, we include the intrinsic nonlinear effects in our considerations.

In Chapter 2, we introduce our basic setup, consisting of a Bose-Einstein condensate in a moving optical lattice, which is created by a pair of frequency-chirped counterpropagating laser beams.

Using a constantly accelerated optical lattice, successful acceleration of ultracold but non-condensed atoms was reported in Refs. [60, 61, 62, 63, 64, 65] by means of *rapid adiabatic passage*. There, the moving lattice induced sequential coupling between neighboring momentum modes. In Chapter 3, we extend this scheme to Bose-Einstein condensates and investigate the acceleration efficiency for various acceleration rates and condensate sizes. Accordingly, we identify switch-on effects of the lattice and dynamical as well as nonlinear effects as the major mechanisms

responsible for loss of the initial monochromaticity. After publication of our work, two groups experimentally demonstrated the predicted behavior [1, 2, 66].

As a next step, in Chapter 4, we demonstrate how to improve the efficiency of the acceleration scheme by dropping the restriction of constant accelerations. Allowing for an arbitrary time-dependent frequency chirp of the lattice beams, we employ genetic algorithms to optimize the motion of the lattice. This permits a fast and highly efficient transfer between momentum modes, even for large condensates with high nonlinearities. We also demonstrate how to create arbitrary superposition states in momentum space by additionally optimizing for a prescribed relative phase between two modes.

In addition to accelerating condensates, it is desirable to transport atomic wave packets without dispersion. This can be achieved by creating solitons, where the nonlinearity cancels the dispersive effects. In Chapter 5, we show that by placing a Bose-Einstein condensate with repulsive interactions in a lattice, one can create a negative effective mass. Under these circumstances bright and stable soliton solutions exist, so-called *gap solitons*. Using the results from previous chapters, we also discuss how to excite these solitons.

We conclude by briefly considering a new direction in the field of atom optics: quantum degenerate Fermi gases. Chapter 6 contains an investigation of a “toy model” of a fermionic coupler, where internal states of trapped fermions are coupled by a light field. The system is a simple example of a nonlinear multimode coupler and illustrates clearly the difference between bosonic and fermionic dynamics. Understanding the basic mechanisms that influence the behavior of the system is a first step towards the extension of more sophisticated coherent manipulation schemes from bosons to fermions.

Chapter 7 then summarizes the results and provides an outlook on future research.

1.2.2 Publications

In direct context of this dissertation, the following articles have been published:

- *Coherent acceleration of Bose-Einstein condensates*,
S. Pötting, M. Cramer, C. H. Schwalb, H. Pu, and P. Meystre,
Phys. Rev. A **64**, 023604 (2001).
- *Momentum-state engineering and control in Bose-Einstein condensates*,
S. Pötting, M. Cramer, and P. Meystre,
Phys. Rev. A **64**, 063613 (2001).
- *Atomic Solitons in Optical Lattices*,
S. Pötting, P. Meystre, and E. M. Wright.
In *Nonlinear Photonic Crystals*, edited by R. E. Slusher and B. J. Eggleton
(Springer-Verlag, Heidelberg, 2003).
- *Raman coupler for a trapped two-component quantum-degenerate Fermi gas*,
S. Pötting, M. Cramer, W. Zhang, and P. Meystre,
Phys. Rev. A **65**, 063620 (2002).

Refer to Appendix D for a complete list of publications of the author that originated from research in the field of quantum and atom optics.

Chapter 2

The Model System

We base our investigations on the mean field theory of Bose-Einstein condensates at zero temperature. The Gross-Pitaevskii equation (GPE), provides an excellent description of many features of this system, as has been demonstrated in numerous experiments [13, 16, 19, 20, 67, 68, 69, 70, 71]. Although this approach does not capture intrinsic many-body effects such as higher-order coherence, it proves to be sufficient for momentum state control. In this chapter, we first derive the stationary GPE in Section 2.1 via a variational approach [72]. In Section 2.2, we then briefly work out the condensate ground state properties in a harmonic trap [72], since this often serves as a starting point for numerical simulations. In order to describe the dynamics of Bose-Einstein condensates, in Section 2.3 we derive the equation of motion in the mean field limit, the time-dependent GPE. We discuss its validity, and reduce it to one dimension, a step appropriate for the tight transverse confinement of the condensate considered throughout the dissertation.

At the core of the dissertation lies the manipulation of condensates with the help of time-dependent periodic optical potentials or optical lattices. Section 2.4 introduces the laser geometry used to generate a frequency-chirped lattice and derives the resulting time-dependent potential experienced by the atoms. We complete this section by introducing scaling parameters in lattice recoil units. Then, Section 2.5 reviews basic properties of optical lattices, including the band structure model, the concept of an effective mass, and summarizes effects such as Bloch oscillations and Landau-Zener tunneling [73, 74, 75]. This will prove useful for the physical interpretation of some of the processes we study.

2.1 Stationary Gross-Pitaevskii equation

To set the stage for our discussion, we first derive the stationary mean-field GPE for an atomic Bose-Einstein condensate, following Ref. [72]. The time-independent Schrödinger equation for a system of N bosonic atoms with many-body wave function $\Psi(\mathbf{r}_1, \dots, \mathbf{r}_N)$ is given by

$$H\Psi(\mathbf{r}_1, \dots, \mathbf{r}_N) = E\Psi(\mathbf{r}_1, \dots, \mathbf{r}_N), \quad (2.1)$$

where the N -particle wave function is normalized to unity ¹

$$\int d\mathbf{r}_1 \dots d\mathbf{r}_N |\Psi(\mathbf{r}_1, \dots, \mathbf{r}_N)|^2 = 1, \quad (2.2)$$

¹Integrations are always over the whole space unless stated otherwise.

and the Hamiltonian is given by

$$H = \sum_{i=1}^N \left[-\frac{\hbar^2}{2M} \nabla_i^2 + V(\mathbf{r}_i) \right] + \sum_{i<j}^N V(\mathbf{r}_i, \mathbf{r}_j). \quad (2.3)$$

We consider a dilute atomic gas so that we can restrict ourselves to one-body and two-body interactions. In Eq. (2.3), $V(\mathbf{r}_i)$ denotes the single-particle potential and $V(\mathbf{r}_i, \mathbf{r}_j)$ the two-particle potential. Our goal is to find the wave function that minimizes the energy functional

$$E[\Psi] = \int d\mathbf{r}_1 \dots d\mathbf{r}_N \Psi^* H \Psi. \quad (2.4)$$

Considering that in the fully condensed state at zero temperature all bosons are in the same ground state $\psi(\mathbf{r})$, we proceed by applying the Hartree or mean field approximation, where we assume that the N -particle wave function is a product of Hartree wave functions,

$$\Psi(\mathbf{r}_1, \dots, \mathbf{r}_N) = \prod_{i=1}^N \psi(\mathbf{r}_i), \quad (2.5)$$

where the wave function $\psi(\mathbf{r})$ is normalized to unity,

$$\int d\mathbf{r} |\psi(\mathbf{r})|^2 = 1. \quad (2.6)$$

We also consider a short-range pseudopotential of the form [76]

$$V(\mathbf{r}_i, \mathbf{r}_j) = U \delta(\mathbf{r}_i - \mathbf{r}_j), \quad (2.7)$$

where the interaction strength is given by

$$U = \frac{4\pi\hbar^2 a_s}{M}, \quad (2.8)$$

and a_s is the s-wave scattering length for atoms in their electronic ground state. In the framework of scattering theory it can be shown that this s-wave scattering is the major contribution for scattering of ultracold bosons [36]. With this explicit two-particle interaction and in the Hartree approximation we can write the energy functional from Eq. (2.4) as

$$E[\psi] = N \int d\mathbf{r} \left[\frac{\hbar^2}{2M} |\nabla\psi(\mathbf{r})|^2 + V(\mathbf{r}) |\psi(\mathbf{r})|^2 + \frac{N}{2} U |\psi(\mathbf{r})|^4 \right], \quad (2.9)$$

where we assumed a large number of atoms in the condensate so that $N - 1 \approx N$. The contributions to the total energy in Eq. (2.9) can be identified in their order of appearance as kinetic, potential and mean field energy. Minimizing the energy functional with respect to $\psi(\mathbf{r})$ leads to an equation for the nonlinear ground state wavefunction. In order to ensure constancy of the particle number we add the constraint

$$N[\psi] \equiv N \int d\mathbf{r} |\psi(\mathbf{r})|^2 - N = 0. \quad (2.10)$$

The constraint is incorporated with the help of a Lagrange multiplier μ , so that we minimize $E[\psi] - \mu N[\psi]$ with respect to ψ . We obtain the stationary GPE

$$\left[-\frac{\hbar^2}{2M} \nabla^2 + V(\mathbf{r}) \right] \psi(\mathbf{r}) + NU |\psi(\mathbf{r})|^2 \psi(\mathbf{r}) = \mu \psi(\mathbf{r}). \quad (2.11)$$

The Lagrange multiplier μ is the chemical potential. The stationary GPE is a mean field equation that describes one particle in the effective presence of $N - 1$ others.

2.2 Ground state properties

The solution of the stationary GPE from Eq. (2.11) determines the ground state of a condensate in a trapping potential $V(\mathbf{r})$. Since the solution agrees well with experimentally observed condensate states, it serves as a starting point for most of our numerical investigations. Here, we introduce two approximation methods that hold for large condensates and allow us to estimate the condensate size, atom number and chemical potential. On the one hand, the Thomas-Fermi approximation of Section 2.2.1 allows for accurate estimates of the wave function and the chemical potential. The wave function, however, suffers from a discontinuity of the first derivative at the edge of the cloud. On the other hand, the Gaussian variational approach in Section 2.2.2 yields a smooth wave packet and approximates the chemical potential fairly well. Although the shape of the wave function differs significantly from the actual solution, the smooth Gaussian estimate proved to be a good initial wave packet for numerical simulations.

In the following, we consider for concreteness a Bose-Einstein condensate in three-dimensional anisotropic harmonic oscillator traps with the potential given by

$$V(\mathbf{r}) = \frac{1}{2}M(\omega_x^2 x^2 + \omega_y^2 y^2 + \omega_z^2 z^2), \quad (2.12)$$

where the ω_i ($i = x, y, z$) are the harmonic trap frequencies.

2.2.1 Thomas-Fermi approximation

An accurate expression for the ground state energy may under appropriate conditions be obtained by neglecting the kinetic energy with respect to the interparticle interaction in the GPE Eq. (2.11). This is the case for fairly dense clouds with a large number of atoms, so that $N|\psi|^2$ is dominating the kinetic energy contribution. This approximation is reminiscent of the Thomas-Fermi approximation in the theory of atoms with large numbers of electrons, where complicated terms in the kinetic and electron-electron repulsion energy are replaced by simple functionals of the electron density [77]. It is therefore referred to by this name also in the context of Bose-Einstein condensates. The stationary GPE from Eq. (2.11) then reads

$$\mu\psi(\mathbf{r}) = \left[V(\mathbf{r}) + NU|\psi(\mathbf{r})|^2 \right] \psi(\mathbf{r}). \quad (2.13)$$

The condensate density then has the solution

$$|\psi(\mathbf{r})|^2 = \begin{cases} \frac{\mu - V(\mathbf{r})}{NU} & : \mu \geq V(\mathbf{r}) \\ 0 & : \text{else} \end{cases}. \quad (2.14)$$

For a harmonic potential in Eq. (2.12) this is an ellipsoid with semi-axes of length $R_i = \sqrt{2\mu/M\omega_i}$ ($i = x, y, z$). Scaling each coordinate by the respective axis length, one can integrate over the interior of the resulting unit sphere. The normalization condition Eq. (2.6) then yields a relation between the chemical potential and the number of particles:

$$\mu = \frac{15^{2/5}}{2} \left(\frac{Na_s}{\bar{a}} \right)^{2/5} \hbar\bar{\omega}, \quad (2.15)$$

with the geometric mean $\bar{\omega}$ of the oscillator frequencies defined as

$$\bar{\omega} = (\omega_x\omega_y\omega_z)^{1/3} \quad (2.16)$$

and the characteristic length \bar{a} defined as

$$\bar{a} = \sqrt{\frac{\hbar}{M\bar{\omega}}}. \quad (2.17)$$

2.2.2 Gaussian variational calculation

As a second method we estimate the ground state by a variational method [72]. We seek Gaussian solutions of the form

$$\psi(\mathbf{r}) = \frac{2\sqrt{2}}{\pi^{3/4}\sqrt{w_x w_y w_z}} e^{-2\left(\frac{x^2}{w_x^2} + \frac{y^2}{w_y^2} + \frac{z^2}{w_z^2}\right)}, \quad (2.18)$$

where w_i ($i = x, y, z$) are the variational parameters that denote the spatial Gaussian widths.² This trial Gaussian wave function, which is normalized to unity, is inserted into the energy functional Eq. (2.9) and we obtain

$$E(w_x, w_y, w_z) = N \sum_{i=x,y,z} \hbar\omega_i \left(\frac{a_i^2}{w_i^2} + \frac{w_i^2}{16a_i^2} \right) + \frac{\sqrt{2}N^2U}{w_x w_y w_z \pi^{3/2}}. \quad (2.19)$$

Here, we introduced the harmonic oscillator lengths $a_i = (\hbar/M\omega_i)^{1/2}$ ($i = x, y, z$). Minimizing with respect to the variational parameters w_i , i.e.

$$\frac{\partial E}{\partial w_i} = 0, \quad (2.20)$$

we obtain the following coupled equations

$$\frac{1}{2}\hbar\omega_i \left(\frac{w_i^2}{4a_i^2} - \frac{4a_i^2}{w_i^2} \right) - \frac{\sqrt{2}NU a_x a_y a_z}{w_x w_y w_z \bar{a}^3 \pi^{3/2}} = 0, \quad (2.21)$$

where we defined \bar{a} as in Eq. (2.17). In general, these equations can be solved numerically. However, if the number of particles is large, we can neglect the kinetic energy terms (proportional to $1/w_i^2$) with respect to the interaction energy per particle. Then Eqs. (2.21) decouple and we can solve for the variational parameters w_i . Substituting the expression for U from Eq. (2.8), the solutions are

$$w_i = 2 \left(\frac{2}{\pi} \right)^{1/10} \left(\frac{N a_s}{\bar{a}} \right)^{1/5} \frac{\bar{\omega}}{\omega_i} \bar{a}, \quad (2.22)$$

with $\bar{\omega}$ defined as in Eq. (2.16). To leading order, i.e. neglecting the kinetic energy term as before in Eq. (2.19), the chemical potential can be calculated by the thermodynamical relation $\mu = \partial E / \partial N$, which gives

$$\mu = \frac{7}{4} \left(\frac{2}{\pi} \right)^{1/5} \left(\frac{N a_s}{\bar{a}} \right)^{2/5} \hbar\bar{\omega}, \quad (2.23)$$

showing that the chemical potential scales as $N^{2/5}$.

As in the Thomas-Fermi approximation in Eq. (2.15), we have $\mu \propto N^{2/5}$, however, the explicit expressions for the chemical potentials for the two approximations differ by a numerical factor of ≈ 0.92 . Figure 2.1 compares the ground states for the two approximations and an exact numerical calculation for the case of a spherically symmetric trap. The Thomas-Fermi solution is very close to the numerical solution³ and only fails close to the edge of the condensate cloud. It was shown that the region where the two solutions differ approaches zero with increasing particle number [78]. The variational solution only roughly approximates the numerical solution, but does not suffer from a discontinuity in the first derivative at the edge of the cloud. For numerical simulations we prefer the smooth Gaussian approximation or numerically determined ground states over the Thomas-Fermi solution, which introduces high frequency components due to the sharp edge.

²Throughout the dissertation we use the convention that by the width of a Gaussian we always refer to the full width at $1/e$ of the maximum of the density $|\psi|^2$ of a wave function.

³The numerical method used to calculate nonlinear ground states is presented in Appendix A.2.

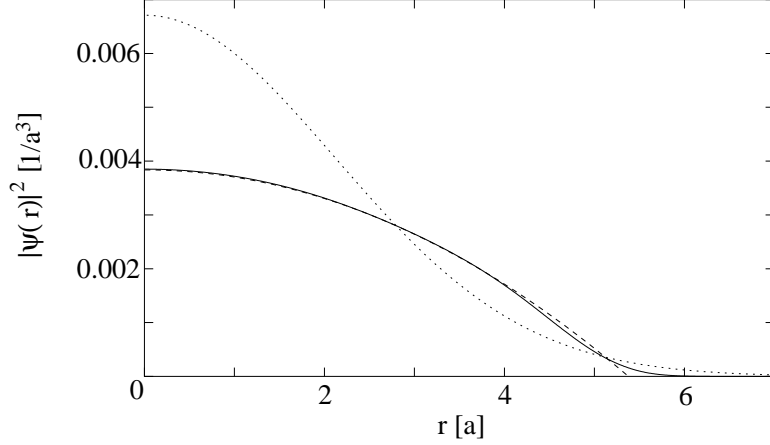


Figure 2.1: Ground state of a condensate in a spherically harmonic trap ($a_x = a_y = a_z \equiv a$) for $N = 10^5$ atoms and a ratio $a_s/a = 0.003$: full numerical solution (solid), Thomas-Fermi approximation (dashed), and Gaussian variational approximation (dotted).

2.3 Time-dependent Gross-Pitaevskii equation

Having derived the stationary GPE in Section 2.1 that provides the ground state wave function and energy, we now seek an equation of motion for the mean field Hartree wave function ψ . This enables us to investigate the dynamics of condensates in various external potentials. Similar to the energy functional in Eq. (2.4), we can write the action functional of the N -particle wave function as

$$S[\Psi] = \int dt \int d\mathbf{r}_1 \dots d\mathbf{r}_N \Psi^* \left(i\hbar \frac{\partial}{\partial t} - H \right) \Psi. \quad (2.24)$$

We recall that the action functional can be written in form of a Lagrangian density \mathcal{L} as

$$S = \int dt \int d\mathbf{r} \mathcal{L}(\theta, \partial_t \theta, \partial_i \theta), \quad (2.25)$$

where we abbreviated $\partial_t = \partial/\partial t$ and $\partial_i = \{\partial/\partial x, \partial/\partial y, \partial/\partial z\}$. The arguments of the Lagrangian density are defined as $\theta = \{\psi, \psi^*\}$, $\partial_t \theta = \{\partial_t \psi, \partial_t \psi^*\}$ and $\partial_i \theta = \{\partial_i \psi, \partial_i \psi^*\}$. Employing the Hartree approximation from Eq. (2.5) and using the pseudopotential from Eq. (2.7), we can identify the Lagrangian density to be

$$\begin{aligned} \mathcal{L}(\theta, \partial_t \theta, \partial_i \theta) &= \frac{i\hbar}{2} N [\psi^*(\mathbf{r}, t) \partial_t \psi(\mathbf{r}, t) - \psi(\mathbf{r}, t) \partial_t \psi^*(\mathbf{r}, t)] \\ &\quad - \frac{\hbar^2}{2M} N |\nabla \psi(\mathbf{r}, t)|^2 - V(\mathbf{r}, t) N |\psi(\mathbf{r}, t)|^2 \\ &\quad - \frac{N(N-1)}{2} U |\psi(\mathbf{r}, t)|^4, \end{aligned} \quad (2.26)$$

where we now choose the one-particle potential to be explicitly time-dependent. The Euler-Lagrange equations of motion for fields [79],

$$\partial_t \frac{\partial \mathcal{L}}{\partial(\partial_t \psi^*)} = \frac{\partial \mathcal{L}}{\partial \psi^*} - \sum_i \partial_i \frac{\partial \mathcal{L}}{\partial(\partial_i \psi^*)}, \quad (2.27)$$

lead directly to an equation of motion for the Hartree function, the so-called time-dependent GPE:

$$i\hbar \frac{\partial}{\partial t} \psi(\mathbf{r}, t) = \left[-\frac{\hbar^2}{2M} \nabla^2 + V(\mathbf{r}, t) \right] \psi(\mathbf{r}, t) + NU |\psi(\mathbf{r}, t)|^2 \psi(\mathbf{r}, t), \quad (2.28)$$

where, again, we assumed large condensates so that $N - 1 \approx N$.

We derived the time-dependent as well as the stationary GPE under the explicit assumption of a system in a number state by starting with an N -particle wave function. When deriving the GPE within the framework of second quantization, one can also arrive at a mean field equation for the expectation value of the field operator with respect to a coherent state. Both approaches, number state and coherent state assumptions, lead to identical GPEs for large number of particles [36].

2.3.1 Reduction to one dimension

For most of the phenomena that we investigate it is not necessary to solve the full three-dimensional time-dependent GPE, since we restrict ourselves to control and manipulation of the atomic condensate in only one dimension. We assume the condensate to be confined by a static potential in the other two dimensions. In this section we show that a tight confinement in these dimensions enables us to reduce the GPE to a one-dimensional equation of motion. This equation then captures the important physics and is more accessible to analytical and numerical treatment.

Consider a potential of the form

$$V(\mathbf{r}, t) = V(z, t) + V_{\perp}(x, y). \quad (2.29)$$

Typically, $V(z, t)$ will be an optical potential used to manipulate the state of the condensate, while $V_{\perp}(x, y)$ is an optical or magnetic trapping potential in the transverse direction. The condensate is assumed to be tightly confined in the (x, y) plane, so that the spacing of the energy levels of the transverse trapping potential exceeds the magnitude of the mean field energy. Transverse excitations are then suppressed in this quasi-one-dimensional geometry, and we can also neglect the mean-field effects in this direction. The transverse mode $\varphi_{\perp}(x, y)$ is then the ground state of the potential $V_{\perp}(x, y)$, obeying the eigenvalue equation

$$E_{\perp} \varphi_{\perp}(x, y) = -\frac{\hbar^2}{2M} \left(\frac{\partial^2}{\partial x^2} + \frac{\partial^2}{\partial y^2} \right) \varphi_{\perp}(x, y) + V_{\perp}(x, y) \varphi_{\perp}(x, y). \quad (2.30)$$

The potential in Eq. (2.29) may be realized, for example, using a red-detuned optical dipole trap around the focus of a Gaussian laser beam centered on the origin [80], thereby giving approximately harmonic transverse confinement. Substituting the factorized Hartree function

$$\psi(\mathbf{r}, t) = \psi(z, t) \varphi_{\perp}(x, y) e^{-iE_g t/\hbar} \quad (2.31)$$

into the time-dependent GPE from Eq. (2.28) and projecting onto the normalized transverse mode φ_{\perp} , the reduced one-dimensional GPE becomes

$$i\hbar \frac{\partial}{\partial t} \psi(z, t) = \left[-\frac{\hbar^2}{2M} \frac{\partial^2}{\partial z^2} + V(z, t) \right] \psi(z, t) + NU_0 |\psi(z, t)|^2 \psi(z, t). \quad (2.32)$$

We define the effective one-dimensional nonlinear coefficient U_0 as

$$U_0 = U \int dx dy |\varphi_{\perp}(x, y)|^4. \quad (2.33)$$

In particular, if the transverse ground state can be approximated as a Gaussian of width w_\perp ,

$$\varphi_\perp(x, y) = \frac{2}{\sqrt{\pi}w_\perp} \exp\left(-2\frac{x^2 + y^2}{w_\perp^2}\right), \quad (2.34)$$

the explicit expression for the effective nonlinear coefficient is $U_0 = 2U/\pi w_\perp^2$ according to Eq. (2.33).

2.4 Optical lattices

After having introduced the basic mean field properties and evolution equations for the Bose-Einstein condensate, we now focus on the derivation of a time-dependent optical lattice potential, our main tool to manipulate the momentum state of matter waves. We present the derivation in detail to clearly state the time scales involved and approximations made, since this is crucial for a possible experimental verification of our predictions.

2.4.1 Laser geometry

We consider a two-level atom in an optical lattice potential along the z -axis created by two counterpropagating laser fields with frequencies ω_L and $\omega'_L(t) = \omega_L - \delta(t)$ and wave vectors k_L and $k'_L(t)$, respectively. The time-dependent frequency detuning $\delta(t)$ between the two fields can be chosen to have positive or negative values. We consider the case where the transverse atomic wave function is much smaller than the beam waist and the longitudinal extent is much less than the Rayleigh range. It is then appropriate to approximate the counterpropagating laser beams as plane waves propagating along the z -axis,

$$\mathbf{E}(z, t) = \frac{\mathcal{E}}{2} \epsilon \left[e^{i(k_L z - \omega_L t)} + e^{i\{k'_L(t)z - [\omega_L - \delta(t)]t + \phi\}} \right] + \text{c.c.}, \quad (2.35)$$

where we choose the electric field amplitude \mathcal{E} and the polarization vector ϵ of both fields to be the same. ϕ is the fixed relative phase between the two laser fields. For simplicity, we consider the case of a two-level atom that is electric dipole-coupled to the light field. Figure 2.2 shows the two-level system consisting of a ground state $|g\rangle$ and an excited state $|e\rangle$, separated by the energy $\hbar\omega_A$. We define the detuning from the atomic resonance as

$$\Delta = \omega_A - \omega_L. \quad (2.36)$$

In order to avoid spontaneous emission from the excited state, we use far-off resonant light, so that $|\Delta| \gg \Gamma$, with Γ the spontaneous decay rate of the excited atomic level. Furthermore, we choose the frequencies so that

$$|\delta(t)| \ll |\Delta| \ll \omega_L. \quad (2.37)$$

This inequality holds in typical experimental setups, where ω_L is in the optical regime, Δ in the GHz-regime and δ in the MHz-regime.

2.4.2 Lattice potential

The coupled Schrödinger equations for the ground and excited state wave functions ψ_g and ψ_e in the electric dipole approximation [81] read

$$i\hbar \frac{\partial}{\partial t} \psi_g = \left[-\frac{\hbar^2}{2M} \nabla^2 + V(\mathbf{r}) \right] \psi_g - \mathbf{d}_{eg}^* \cdot \mathbf{E}(t) \psi_e \quad (2.38)$$

$$i\hbar \frac{\partial}{\partial t} \psi_e = \left[-\frac{\hbar^2}{2M} \nabla^2 + V(\mathbf{r}) + \hbar\omega_A \right] \psi_e - \mathbf{d}_{eg} \cdot \mathbf{E}(t) \psi_g, \quad (2.39)$$

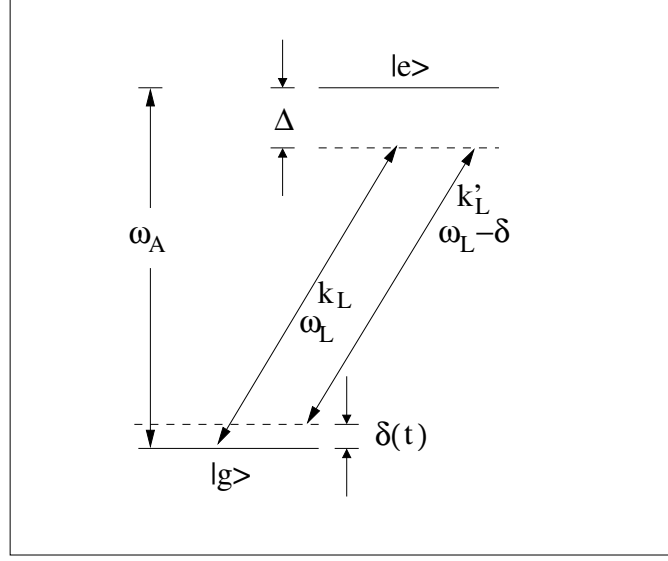


Figure 2.2: Two-level atom coupled by two laser fields, one with frequency ω_L and wave vector k_L , the other with $\omega_L - \delta$ and k'_L , respectively.

where $\mathbf{d}_{eg} = \mathbf{d}_{ge}^*$ is the atomic dipole moment of the transition and $V(\mathbf{r})$ an external potential in addition to the two laser fields. We proceed by adiabatically eliminating the excited state dynamics. Transformation to a rotating frame with $\psi_e(\mathbf{r}, t) \rightarrow \psi_e(\mathbf{r}, t) \exp(-i\omega_L t)$ leads to the coupled equations

$$i\hbar \frac{\partial}{\partial t} \psi_g = \left[-\frac{\hbar^2}{2M} \nabla^2 + V(\mathbf{r}) \right] \psi_g - \mathbf{d}_{eg}^* \cdot \mathbf{E}(t) \psi_e e^{-i\omega_L t} \quad (2.40)$$

$$i\hbar \frac{\partial}{\partial t} \psi_e = \left[-\frac{\hbar^2}{2M} \nabla^2 + \hbar\Delta + V(\mathbf{r}) \right] \psi_e - \mathbf{d}_{eg} \cdot \mathbf{E}(t) \psi_g e^{i\omega_L t}, \quad (2.41)$$

with the detuning Δ defined in Eq. (2.36). If the magnitude of the detuning term greatly exceeds the kinetic and potential energy terms in Eq. (2.41), we can neglect these terms and formally solve for the excited state wave function,

$$\psi_e(t) \approx \frac{i}{\hbar} \psi_g(t) e^{-i\Delta t} \int_0^t dt' e^{i\Delta t'} \mathbf{d}_{eg} \cdot \mathbf{E}(t') e^{i\omega_L t'}. \quad (2.42)$$

Here, we made use of the fact that $\psi_g(t)$ is slowly varying compared to all other terms, which oscillate at least at frequency Δ , and $\psi_g(t)$ was taken outside the integral. We now substitute the explicit form of the electric field from Eq. (2.35) into the excited state solution from Eq. (2.42). According to Eq. (2.37), we can perform the rotating wave approximation (RWA) by neglecting terms that oscillate at $\approx 2\omega_L$, i.e. at twice the optical frequency, and obtain

$$\psi_e(t) = i \frac{\Omega_L}{2} \psi_g(t) e^{-i\Delta t} \int_0^t dt' \left[e^{i(k_L z + \Delta t')} + e^{i(k'_L z + (\Delta + \delta)t' + \phi)} \right]. \quad (2.43)$$

Here, we introduced the Rabi frequency as $\Omega_L = \mathbf{d}_{eg} \cdot \boldsymbol{\epsilon} \mathcal{E} / \hbar$. Carrying out the integration leads to

$$\begin{aligned} \psi_e(t) &= \frac{\Omega_L}{2\Delta} \psi_g(t) e^{i(k_L z - \Delta t)} (e^{i\Delta t} - 1) \\ &+ \frac{\Omega_L}{2\Delta} \psi_g(t) e^{i(k'_L z - \Delta t + \phi)} (e^{i(\Delta + \delta)t} - 1) \\ &- i \frac{\Omega_L}{2} \psi_g(t) e^{i(k'_L z - \Delta t + \phi)} \int_0^t dt' e^{i(\Delta + \delta)t'} \left[\frac{\delta}{\Delta} + \frac{t'}{\Delta} \frac{d\delta}{dt'} \right]. \end{aligned} \quad (2.44)$$

The time scale over which $\psi_g(t)$ changes is given by the inverse Rabi frequency $1/\Omega_L$. If we now demand that

$$\left| \frac{d\delta}{dt} \right| \ll |\Omega_L \Delta|, \quad (2.45)$$

and recall from Eq. (2.37) that $|\delta(t)| \ll |\Delta|$, we can safely neglect the integral in Eq. (2.44). We then substitute the remaining terms into the equation of motion for the ground state, Eq. (2.40). Once again we perform the RWA by only keeping terms oscillating at the frequency $\delta(t)$ and neglecting all others, since they are considerably faster according to Eq. (2.37). We end up with an effective equation for the wave function of the electronic ground state,

$$\begin{aligned} i\hbar \frac{\partial}{\partial t} \psi_g &= \left(-\frac{\hbar^2}{2M} \nabla^2 + V(\mathbf{r}) \right) \psi_g \\ &- \frac{\hbar |\Omega_L|^2}{2\Delta} \{1 + \cos[(k_L - k'_L)z - \delta t + \phi]\} \psi_g, \end{aligned} \quad (2.46)$$

where we replaced N_g by the total number of atoms N since the excited state is negligibly populated. We now define the lattice depth as $V_0 = \hbar |\Omega_L|^2 / 2\Delta$, remove the constant energy term by the transformation $\psi_g \rightarrow \psi_g \exp(iV_0 t / \hbar)$ and choose the fixed relative phase between the two laser fields to be $\phi = \pi$.⁴ This leaves us with

$$\begin{aligned} i\hbar \frac{\partial}{\partial t} \psi_g &= \left(-\frac{\hbar^2}{2M} \nabla^2 + V(\mathbf{r}) \right) \psi_g \\ &+ V_0 \cos[(k_L - k'_L)z - \delta t] \psi_g. \end{aligned} \quad (2.47)$$

The laser beams produce an effective cosine-shaped potential due to the AC-Stark shift. As a last step, we simplify the expression for the wave vector difference in the argument of the cosine. We rewrite the difference of the wave vectors and the change of $k'_L(t)$ with time as

$$\frac{1}{k_L} |k_L| - |k'_L| = \frac{\delta}{\omega_L}, \quad (2.48)$$

$$\frac{1}{k_L \omega_L} \left| \frac{dk'_L}{dt} \right| = \frac{1}{\omega_L^2} \left| \frac{d\delta}{dt} \right|. \quad (2.49)$$

Due to the conditions imposed in Eqs. (2.37) and (2.45), k'_L does not change significantly with time and k_L and k'_L are essentially of equal magnitude, $|k'_L(t)| \approx |k_L|$. Since we consider counterpropagating laser fields, we have $k'_L = -k_L$. The

⁴The relative phase ϕ corresponds to a constant spatial shift of the lattice potential. We choose $\phi = \pi$ for convenience, so that the lattice maximum occurs at $z = 0$.

atom in the electronic ground state then experiences an effective optical lattice potential

$$V_{lat}(z, t) = V_0 \cos [2k_L z - \delta(t)t]. \quad (2.50)$$

The frequency chirp $\delta(t)$ causes the optical lattice fringes to move at the instantaneous velocity

$$v_{lat}(t) = \frac{1}{2k_L} \frac{d}{dt} [\delta(t)t]. \quad (2.51)$$

Note that neglecting the temporal change of the wave vector k'_L implies lattice velocities much less than the speed of light, $v_{lat} \ll c$.

2.4.3 Recoil units

It is useful to introduce recoil units, which we use throughout the dissertation. The recoil energy E_R and the recoil frequency ω_R , respectively, are defined as

$$E_R = \hbar\omega_R = \frac{\hbar^2 k_L^2}{2M} \quad \text{and} \quad \omega_R = \frac{\hbar k_L^2}{2M}. \quad (2.52)$$

They account for the amount of energy transferred when an atom absorbs or emits one photon from the lattice laser field. Accordingly, the atom momentum is changed by an amount $\hbar k_L$ and the recoil velocity v_R is given by

$$v_R = \frac{\hbar k_L}{M}. \quad (2.53)$$

We also introduce the recoil acceleration rate a_R as

$$a_R = v_R \omega_R. \quad (2.54)$$

The velocity of a particle accelerated at this rate increases by one recoil velocity after a time equal to the inverse of the recoil frequency. The lattice potential in Eq. (2.50) has a periodicity of π/k_L , thus we express length scales in units of $1/k_L$. For example, for typical condensates of sodium atoms, ^{23}Na , and a red detuned laser with wavelength $\lambda = 985$ nm we have

$$\begin{aligned} \omega_R &= 2\pi \times 8.9 \text{ kHz}, \\ v_R &= 1.76 \text{ cm/s}, \\ a_R &= 1551.9 \text{ m/s}^2, \\ 1/k_L &= 0.157 \text{ } \mu\text{m}. \end{aligned} \quad (2.55)$$

The mass of sodium is $M = 3.82 \times 10^{-26}$ kg and the s -wave scattering length $a_s = 4.9$ nm.

2.5 Periodic potentials and band structure

Periodic systems, such as the optical lattice potential introduced in Eq. (2.51), exhibit unique features that are conveniently discussed in terms of energy bands. These energy bands emerge in periodic systems due to many identical potential wells in close proximity. Infinitely separated, each potential well is assumed to have a discrete energy spectrum and the system is highly degenerate. As we move potential wells together, this degeneracy is lifted. The more wells we move together the finer the splitting gets. Eventually, these finely split levels blur into energy bands around an originally degenerate eigenvalue. In this section we briefly derive

the band structure of an optical lattice and review its main features and implications. Especially, we motivate the concept of a negative effective mass and discuss the mechanisms of Bloch oscillations and Landau-Zener tunneling between specific bands. These concepts are useful in the discussion of effects that we investigate in following chapters.

2.5.1 Dispersion curve

Consider a scalar particle in a one-dimensional lattice potential. Its Hamiltonian is given by

$$H = -\frac{\hbar^2}{2M} \frac{\partial^2}{\partial z^2} + V_{lat}(z), \quad (2.56)$$

where V_{lat} is given by Eq. (2.50). The period of the lattice is π/k_L , so that $V_{lat}(z + \pi/k_L) = V_{lat}(z)$. Bloch's theorem [75] requires the eigenfunctions of the Hamiltonian to be of the form

$$\varphi_{nk}(z) = e^{ikz} u_{nk}(z), \quad (2.57)$$

where $u_{nk}(z)$ is spatially periodic with the lattice periodicity, i.e. $u_{nk}(z + \pi/k_L) = u_{nk}(z)$. The eigenfunctions in Eq. (2.57) are characterized by a band index n and a quasimomentum k . Accordingly, the eigenvalues are also characterized by n and k ,

$$H\varphi_{nk}(z) = \epsilon_{nk}\varphi_{nk}(z). \quad (2.58)$$

Substituting the Bloch wave functions $\varphi_{nk}(z)$ into the Hamiltonian (2.56), we find that the spatially periodic functions $u_{nk}(z)$ satisfy the equation

$$H_k u_{nk}(z) = \epsilon_{nk} u_{nk}(z), \quad (2.59)$$

where we defined

$$H_k = \frac{(\hat{p} + \hbar k)^2}{2M} + V_{lat}(z). \quad (2.60)$$

Here, $\hat{p} = -i\hbar\partial/\partial z$ is the single-particle momentum operator. In Fig. 2.3 we compare the dispersion curves of atoms in the periodic potential to the free space case. Figure 2.3(a) shows the parabolic dispersion curve for a free particle reduced to the first Brillouin zone. The effect of the periodic potential is to create avoided crossings of width $\Delta\epsilon_n$, or energy gaps, between bands n and $n-1$ as shown in Fig. 2.3(b). Whereas in free space the particle can assume any energy, the lattice leads to the formation of discrete energy bands, shown in Fig. 2.4 for the same potential as in Fig. 2.3. These bands are labeled by the discrete index n . For this particular choice of potential depth, $V_0 = 2E_R$, the lowest band is weakly bound. The higher bands are separated only by small energy gaps and hence are practically free. For small lattice depths ($V_0 \leq 10E_R$), perturbation theory yields a splitting between the first two bands equal to the potential depth, $\Delta\epsilon \approx V_0$ [82]. Deeper lattices cause the energy gaps to broaden and the width of each band to decrease.

2.5.2 Atomic motion in the lattice

In order to illustrate the effects of the band structure on particle dynamics, we consider a constant external force F acting on the atom in addition to the lattice. The Hamiltonian then reads

$$H' = -\frac{\hbar^2}{2M} \frac{\partial^2}{\partial z^2} + V_{lat}(z) + Fz. \quad (2.61)$$

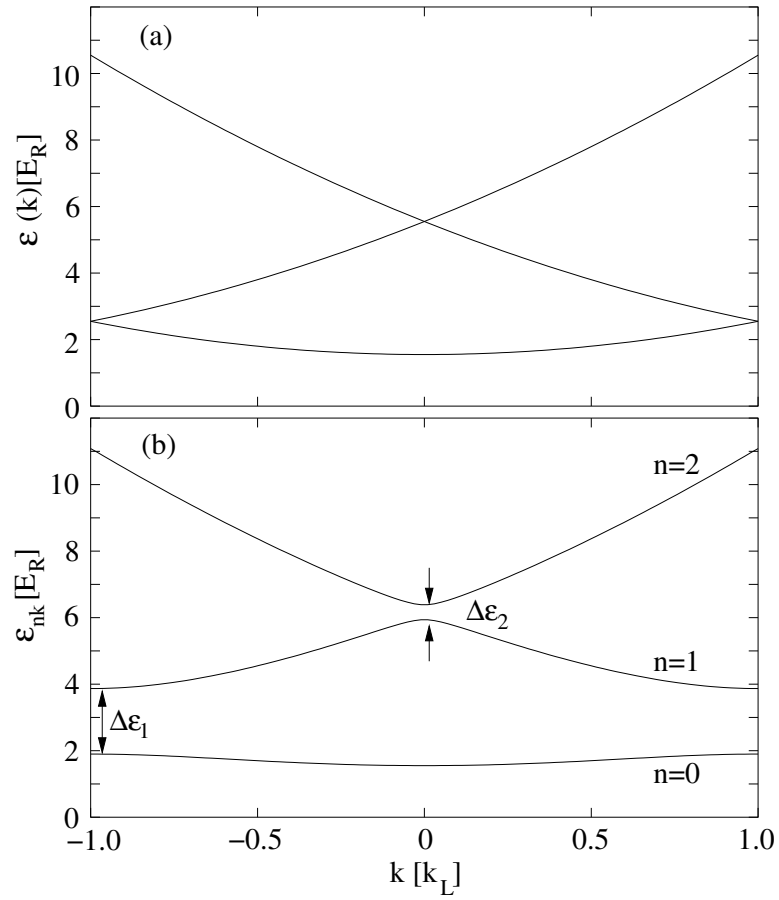


Figure 2.3: Dispersion curves reduced to the first Brillouin zone: (a) a free particle and (b) a particle in the periodic lattice potential $V_{lat} = V_0 \cos(2k_L z)$ with $V_0 = 2E_R$.

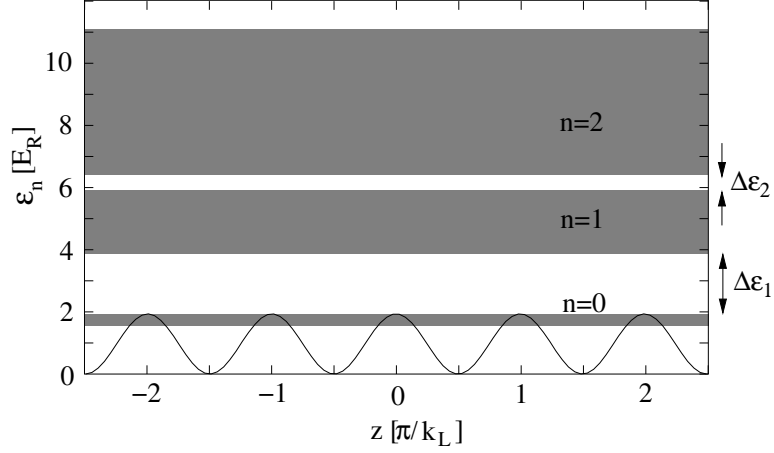


Figure 2.4: Allowed energy bands (grey shaded areas) for the lattice potential in Fig. 2.3 (solid line).

Due to the modified potential, the Bloch functions in Eq. (2.57) are no longer eigenstates of the system. However, the structure of the Bloch functions is preserved when using the time-dependent ansatz

$$\varphi_{nk(t)}(z, t) = e^{ik(t)z} u_{nk}(z, t). \quad (2.62)$$

Using this ansatz in the time-dependent Schrödinger equation

$$i\hbar \frac{\partial}{\partial t} \varphi_{nk(t)}(z, t) = H' \varphi_{nk(t)}(z, t), \quad (2.63)$$

we obtain an equation of motion for the spatially periodic part $u_{nk}(z, t)$,

$$i\hbar \frac{\partial}{\partial t} u_{nk(t)}(z, t) = H_{k(t)} u_{nk(t)}(z, t), \quad (2.64)$$

where we defined

$$H_{k(t)} = \frac{(\hat{p} + \hbar k(t))^2}{2M} + V_{lat}(z), \quad (2.65)$$

as in Eq. (2.60), with the quasimomentum now being time-dependent. Additionally, we obtain an equation for the quasimomentum $k(t)$,

$$\hbar \frac{d}{dt} k(t) = -F. \quad (2.66)$$

This is reminiscent of Newton's law $\dot{p} = F$ for a particle in free space, but with the particle momentum p now replaced by the quasimomentum k . The effect of the external force in both cases is an acceleration of the particle. However, whereas the velocity of a particle in free space subject to a constant force grows linearly, one can show that the mean value of a particle moving in band n of a periodic potential obeys [75]

$$\langle v_n \rangle(k) = \frac{1}{\hbar} \frac{d\epsilon_n(k)}{dk}. \quad (2.67)$$

The mean velocity of a particle in a lattice depends on the shape of the band it is moving in. Figure 2.5(a) illustrates this behavior for the two lowest bands of Fig.

2.3. For example, for the band $n = 0$, the mean velocity is negative for negative k , positive for positive k , and vanishes at the center of the Brillouin zone and at the band edges. Another way to express this behavior is to rewrite the equation of motion for the quasimomentum Eq. (2.66) with the help of Eq. (2.67) to

$$F = M^* \frac{d\langle v_n \rangle}{dt}, \quad (2.68)$$

where we introduced the so-called effective mass M^* as

$$\frac{1}{M^*} = \frac{1}{\hbar^2} \frac{d^2 \epsilon_n(k)}{dk^2}. \quad (2.69)$$

The definition of the effective mass is chosen so that Eq. (2.68) still resembles Newton's equation $m\dot{v} = F$, with the effect of the band structure contained in the effective mass. It is important to point out that the effective mass can assume negative values. Figure 2.5(b) shows this effect for the two lowest bands of Fig. 2.3. For the band $n = 0$, regions of negative curvature and thus negative effective mass occur near the band edges, whereas for band $n = 1$, there is a region of negative effective mass around the center of the Brillouin zone. The existence of a negative effective mass is crucial for the discussion of gap solitons in Chapter 5. Dynamical effects of a negative effective mass on condensates in optical lattices have recently been investigated theoretically [83] and experimentally [84, 85].

2.5.3 Bloch oscillations

Solving Eq. (2.66) yields

$$k(t) = k(0) - \frac{F}{\hbar} t, \quad (2.70)$$

so that the quasimomentum k scans the Brillouin zone linearly with time. The time it takes to traverse the Brillouin zone is the so-called Bloch period T_B and is given by

$$T_B = \frac{2k_L \hbar}{|F|}. \quad (2.71)$$

If the motion of a particle is confined to one band, the particle changes its velocity due to the changing quasimomentum k according to Eq. (2.67) while traversing the Brillouin zone during one Bloch period T_B . Since the Brillouin zone is scanned periodically as long as the external force is applied, the mean velocity exhibits the same periodicity. These oscillations are referred to as Bloch oscillations [73].

2.5.4 Landau-Zener tunneling

Until now we considered atomic motion confined to one energy band. However, there is a finite probability of interband tunneling. This effect was first described by Zener in the context of dielectric breakdown in metals [74]. The probability for a tunneling event to occur between band n and $n - 1$ is given by

$$P_n^{LZ} = \exp\left(-\frac{\pi M \Delta \epsilon_n^2}{4nk_L \hbar^2 |F|}\right), \quad (2.72)$$

where $\Delta \epsilon_n$ is the energy gap between the two bands. The stronger the external force or the smaller the band gap, the more likely are the atoms to tunnel between bands. In the band structure in Fig. 2.3(b), the probability for tunneling out of the lowest band is highest at the band edges. If the system undergoes several Bloch oscillations, Landau-Zener tunneling occurs each time the quasimomentum passes the tunneling region.

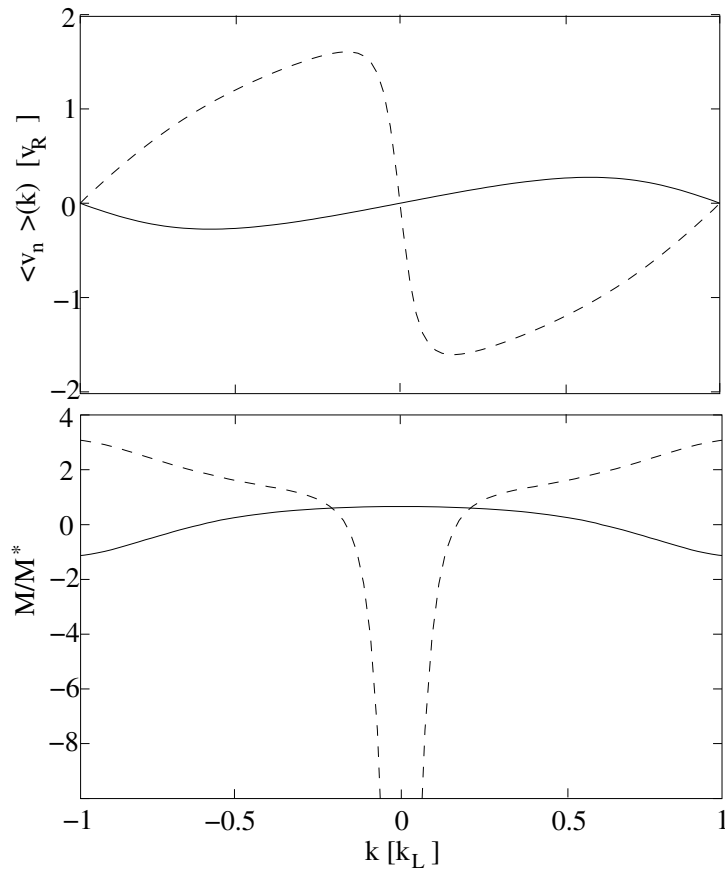


Figure 2.5: (a) Mean velocity and (b) effective mass for the potential in Fig. 2.3 for the lowest band $n = 0$ (solid) and the first excited band $n = 1$ (dashed).

Chapter 3

Acceleration in Optical Lattices

The simplest and most important coherence property of an atomic beam is its monochromaticity. With this in mind, our goal is to determine the extent to which it is possible to significantly accelerate an initially quasi-monochromatic Bose-Einstein condensate without losing this property. We discuss the case of a condensate in an optical lattice accelerated at a constant rate.

After connecting the constantly accelerated lattice potential to the quasimomentum description in an accelerated frame in Section 3.1, we begin by briefly reviewing the case of classical point particles in Section 3.2. Here, starting with an ensemble of spatially distributed atoms at rest, the accelerated optical lattice traps atoms in individual lattice sites and drags them along. The acceleration causes an initially sharp momentum distribution to broaden, the ensemble is considerably heated. Also, increasing the acceleration rate causes fewer atoms to be confined until the confinement vanishes entirely at a critical value.

In contrast to the classical case, the physical origin of acceleration of ultracold and condensed atoms is very different. Here, the atomic wavefunction probes the periodicity of the lattice and the acceleration process can be interpreted as Bragg scattering with continuously varied detuning. For typical experiments, the momentum spread is much smaller than the lattice vector and the atomic momentum can only change by integer multiples of the lattice vector. We refer to these localized peaks as *momentum modes*. In addition, the atoms perform Bloch oscillations, which can easily be explained in the band structure picture. Section 3.3 introduces this type of acceleration by reviewing work done with ultracold atoms, in which the lattice successively couples neighboring momentum modes [60, 61, 62, 63, 64, 65]. If the atoms are initially prepared in the lowest energy band of the periodic potential, the transfer is demonstrated to be perfect if the acceleration rate is small enough. If this is the case, the rate of change of the atomic state due to the accelerating force is small compared to the difference in eigenfrequencies between the bands. The adiabatic theorem [86] then guarantees that the atoms follow the lowest band without being excited to higher bands. Since the acceleration is constant, the quasimomentum of the atoms increases linearly with time while passing through adjacent Brillouin zones. This process is accordingly known as *rapid adiabatic passage*. A side effect of this type of acceleration is the occurrence of Bloch oscillations: while following the lowest band adiabatically, the mean velocity of the atoms in the accelerated frame is determined by the local slope of the band. A full scan of the Brillouin zone is equivalent to one full Bloch oscillation.

However, this type of acceleration relies on small acceleration rates, typically on

the order of $1 - 10 \text{ m/s}^2$, in order to fulfill the adiabatic criterion. This leads to time scales too long for many applications. Also, mean field effects are not taken into account. Therefore, in Section 3.4, we investigate the acceleration efficiency at the limit of adiabaticity. We consider lattice accelerations that are an order of magnitude higher, around 500 m/s^2 , and focus on atomic condensates instead of ultracold atoms. For a fixed lattice depth, we find a regime of efficient coupling, where around 85% of the atoms are transferred to the final mode. Section 3.5 discusses the loss mechanisms that occur during the acceleration process. These losses can be explained either by imperfect Rabi oscillations between momentum modes, or, in the band structure picture, by Landau-Zener tunneling, where atoms are excited to continuum bands. In addition to tunneling losses, sudden switch-on of the lattice potential causes initial loss to free bands. Furthermore, we show in Section 3.6 that large condensates distort the effective band structure and cause considerable nonlinear phase shifts that also degrade the transfer efficiency.

Section 3.7 concludes by briefly connecting our results to recent experiments, in which a Bose-Einstein condensate was accelerated in an optical lattice according to our proposed setup [1, 2].

3.1 Accelerated optical lattice

We investigate the acceleration of condensates by means of a frequency-chirped optical lattice, introduced in Section 2.4. Although we show later on that this is not necessarily an optimum choice, we restrict our analysis in this chapter to linear accelerations produced by a time-dependent detuning between the two lattice laser beams of the form

$$\delta(t) = \eta t, \quad (3.1)$$

so that the lattice potential from Eq. (2.50) reads

$$V_{lat} = V_0 \cos(2k_L z - \eta t^2). \quad (3.2)$$

According to Eq. (2.51), this produces a lattice group velocity v_{lat} linearly changing with time and a constant lattice acceleration a_{lat} ,

$$v_{lat}(t) = \frac{\eta t}{k_L} \quad \text{and} \quad a_{lat} = \frac{\eta}{k_L}. \quad (3.3)$$

This simple case is sufficient to identify and discuss the major physical mechanisms at play in the acceleration of the atoms.

To briefly connect atomic motion in accelerated lattices with the quasimomentum description introduced in Section 2.5.1, we give the explicit unitary transformation between a laboratory frame and an accelerated frame, following Refs. [62, 87]. For single particles, the Hamiltonian in the laboratory frame is given by

$$H_{lab} = \frac{\hat{p}^2}{2M} + V_0 \cos(2k_L z - \eta t^2), \quad (3.4)$$

with \hat{p} the single-particle momentum operator. We now introduce a unitary transformation

$$U(t) = e^{i\alpha(t)\hat{p}/\hbar} e^{-i\beta(t)z/\hbar} e^{i\gamma(t)/\hbar}, \quad (3.5)$$

with the parameters chosen as

$$\alpha(t) = \frac{\eta t^2}{2k_L}, \quad \beta(t) = \frac{M\eta t}{k_L}, \quad \gamma(t) = \frac{M\eta^2 t^3}{3k_L^2}. \quad (3.6)$$

This transformation performs a translation in position space of $\alpha(t) = a_{lat}t^2/2$ and a translation in momentum space $\beta(t) = Ma_{lat}t$. Applying this transformation to H_{lab} then yields the Hamiltonian in the accelerated frame H_{acc} ,

$$H_{acc} = U(t)H_{lab}U^\dagger(t) + i\hbar \left[\frac{\partial}{\partial t}U(t) \right] U^\dagger(t). \quad (3.7)$$

Explicitly, this evaluates to

$$H_{acc} = \frac{\hat{p}^2}{2M} + V_0 \cos(2k_L z) + \frac{M\eta z}{k_L}. \quad (3.8)$$

In the accelerated frame, the atoms experience a constant inertial force $F = M\eta/k_L = Ma_{lat}$ in addition to the effect of the periodic potential. Clearly, H_{acc} is identical to the Hamiltonian in Eq. (2.61). Thus, an accelerated optical lattice is equivalent to the situation considered in Section 2.5.2, where we derived equations of motion for the quasimomentum of a particle in an optical lattice.

3.2 Classical point particles

We first consider the acceleration of an ensemble of N non-interacting, point-like classical particles in the frequency-chirped optical lattice given in Eq. (3.2). We proceed by numerically solving Newton's equations of motion,

$$\frac{d^2 z_i(t)}{dt^2} = \frac{2k_L V_0}{M} \sin(2k_L z - \eta t^2), \quad (3.9)$$

with $i = 1 \dots N$. Initially, the N atoms are at rest and distributed over around 100 lattice sites. The size of this interval and the probability of finding an atom at a given point were chosen to mimic the shape of a Bose-Einstein condensate density profile, to which we turn in Section 3.4. Explicitly, we considered a Gaussian density distribution of the particles.

The solid lines in Fig. 3.1 show the evolution of the mean mean velocity $\langle v(t) \rangle$ of the classical atomic ensemble over the acceleration time for two acceleration rates. We observe that the mean atomic velocity is always somewhat less than the corresponding instantaneous lattice velocity v_{lat} , the dashed lines in Fig. 3.1. The cause of this difference is revealed in Fig. 3.2, which shows the momentum distribution $n(k)$ of the classical ensemble at a fixed time t and for the same two values of a_{lat} . Here, we expressed the momentum p in terms of the wavenumber $k = p/\hbar$. In addition to peaks at positive momenta indicative of accelerated atoms that contribute to an increase in the mean velocity of the sample, a significant group of particles acquire negative momenta, i.e. they are accelerated in the direction opposite to the lattice motion. These are atoms that spill into a well to their left in the moving potential. An explanation for this spilling is easily given in the accelerated frame, where the periodic potential is tilted due to the inertial force F , as shown in Eq. (3.8). Atoms confined to the individual wells are accelerated in the laboratory frame, whereas atoms that are not confined, roll down the potential hill and are not dragged along. Increasing the inertial force, i.e. accelerating the lattice at a higher rate, makes the potential wells shallower, causing fewer atoms to be confined. Once the acceleration reaches a critical value of $a_{crit} = 2k_L V_0/M = 2V_0 a_R/E_R$ there exist no more local minima that can bind the particles and the lattice cannot accelerate any of the atoms. However, it is important to note that, as long as there exist local minima, atoms once trapped will remain trapped.

Another important feature of Fig. 3.2 is that the momentum distributions of both the accelerated and decelerated groups of atoms are rather wide. This shows

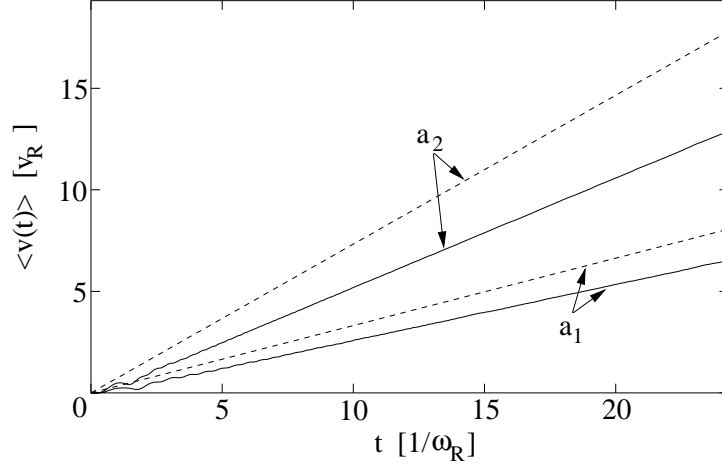


Figure 3.1: Mean velocity of the atomic cloud of classical particles: The simulation uses $N = 10^5$ atoms initially at rest with a Gaussian spatial distribution of longitudinal width $w_z = 318.9/k_L$ and a transverse width $w_\perp = 31.9/k_L$. In lattice recoil units (see Section 2.4.3), the lattice depth is chosen to be $V_0 = 2E_R$ and we consider two acceleration rates, $a_1 = 0.33a_R$ (two lower curves) and $a_2 = 0.73a_R$ (two upper curves). Shown are the results of a numerical simulation (solid) and the instantaneous lattice velocity v_{lat} (dashed).

that (even ignoring the decelerated atoms), the lattice accelerator produces a considerable heating of the atomic sample. This can be a serious problem for applications requiring a high degree of spatial coherence of the atomic beam. We will see that the situation can be significantly improved in the quantum regime for condensates with a mean field energy small compared to the lattice depth, being a result of quantum interferences.

3.3 Bloch oscillations of ultracold atoms

Before focusing on condensate acceleration, we briefly review the situation of ultracold but non-condensed atoms in optical lattices. Ultracold atoms in both static and time-dependent optical lattices have been investigated in several contexts in the recent past. At the single-atom level, they were exploited extensively in theoretical and experimental work aiming at demonstrating effects such as Bloch oscillations [60, 61, 62], Landau-Zener tunneling [63, 88], the appearance of Wannier-Stark ladders [64, 65, 88, 89], quantum chaos [90] and the dynamics of mesoscopic quantum superpositions [91].

Of particular relevance in the present context is Ref. [62], which explicitly considers the acceleration of atoms in a moving periodic potential and interprets it in terms of momentum transfer via multiple rapid adiabatic passage. The experiment proceeds by first laser cooling a sample of cesium atoms so that the velocity distribution corresponds to a Lorentzian shape, with a narrow width of around $0.5v_R$ (full width at half maximum). Then, a statistical mixture of Bloch states is prepared around $k = 0$ in the lowest energy band by adiabatically turning on the lattice potential $V_{lat}(t) = V_0(t) \cos(2k_L z)$. Denoting a Bloch state in band n and quasi-momentum k by $|n, k\rangle$, the atoms stay in the fundamental band if the adiabatic

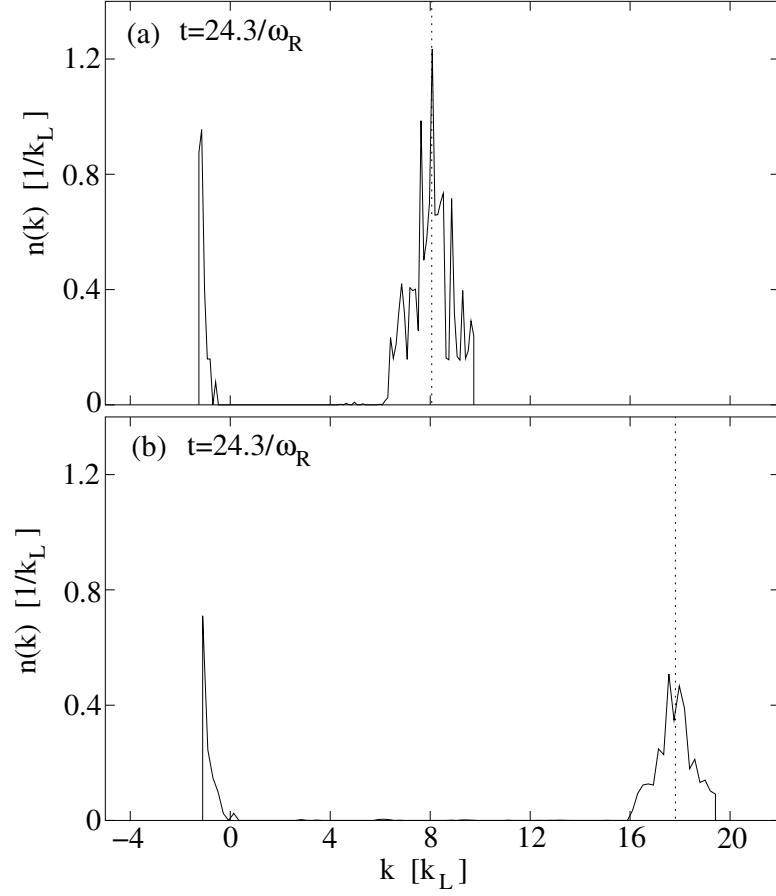


Figure 3.2: Momentum distribution $n(k)$ for the parameters in Fig. 3.1 at time $t = 24.3/\omega_R$, and the acceleration rates $a_1 = 0.33a_R$ (a) and $a_2 = 0.73a_R$ (b). Included is the instantaneous lattice momentum at the time of the plot (vertical dotted line).

criterion [86]

$$\left| \left\langle 1, k \left| \frac{d}{dt} H(t) \right| 0, k \right\rangle \right| \ll (\Delta\epsilon_1)^2 / \hbar \quad (3.10)$$

is fulfilled while ramping up the lattice potential. Here, the time-dependence of the Hamiltonian $H(t)$ derives from the time-dependent lattice depth $V_0(t)$ and $\Delta\epsilon_1$ is the energy splitting at the band gap as defined in Fig. 2.3(b).

The lattice depth is then kept constant and the lattice is accelerated, so that the lattice potential can be written as in Eq. (3.2), $V_{lat}(t) = V_0 \cos(2k_L z - \eta t^2)$. As shown in Section 3.1, this is equivalent to an inertial force $F = Ma_{lat}$ in the accelerated frame, so that we are exactly in the situation described in Section 2.5.2 when discussing atomic motion in a lattice. If the adiabatic criterion of Eq. (3.10) is fulfilled during the acceleration process, the time-dependence of the Hamiltonian now deriving from the motion of the lattice, the atoms will follow the lowest band in which they were prepared. As described in Section 2.5.3, they perform Bloch oscillations.

The explicit expression for the adiabatic criterion, see Ref. [62], is identical to the probability of Landau-Zener tunneling to occur between the two lowest bands, see Eq. (2.72). Thus, tunneling loss is the major restriction on the maximum allowed acceleration rate, in contrast to the case of accelerated classical particles.

3.4 Condensate acceleration

The extension of the work on ultracold atoms to condensates in optical lattices was first investigated theoretically in Refs. [92, 93], both pointing out the possibility of Bloch oscillations, although the nonlinearity is identified to distort the dispersion curve of the system. The first experimental demonstration of a Bose-Einstein condensate in an optical lattice is described in Ref. [13]. There, the condensate is accelerated by gravity in a shallow optical lattice, causing atoms to tunnel out of the different potential wells. These atoms interfere and produce a pulsed output, consisting of a superposition of equidistant modes separated in energy by $Mg\pi/k_L$, the matter-wave equivalent of a mode-locked laser. Other experiments have employed optical lattices to Bragg scatter condensates in order to characterize coherence and phase properties of the condensate [94, 95]. Bragg scattering was exploited to generate multiple momentum sidemodes of the condensate used in matter-wave four-wave mixing experiments [16, 96, 97] and to realize atomic beam splitters used in coherent matter-wave amplifiers [17, 18]. When considering condensates in lattices, the system can undergo a transition from the superfluid phase to a Mott insulator phase, as described in Ref. [98] and recently demonstrated in a groundbreaking experiment [99]. The transition occurs for a critical ratio between the interaction energy of atoms at one lattice site and the tunneling matrix element to neighboring sites. Increasing the lattice depth will in general increase this ratio. However, to reach the critical value for only one atom per site, a lattice depth of $10 - 20E_R$ is needed. Since the critical ratio grows linearly with the number of atoms and we only consider cases with at least 100 atoms per site and moderate lattice depths, Mott insulator effects are not an issue.

We now focus on the acceleration of a condensate at a high rate while at the same time trying to preserve its initial quasi-monochromaticity. Our goal is to gain insight into the physical acceleration mechanism in order to identify degrading processes. For this purpose it is sufficient to describe the atomic system in the Hartree mean-field limit in one dimension, where the evolution of a Bose-Einstein condensate at temperature $T = 0$ in an accelerated optical lattice is described by

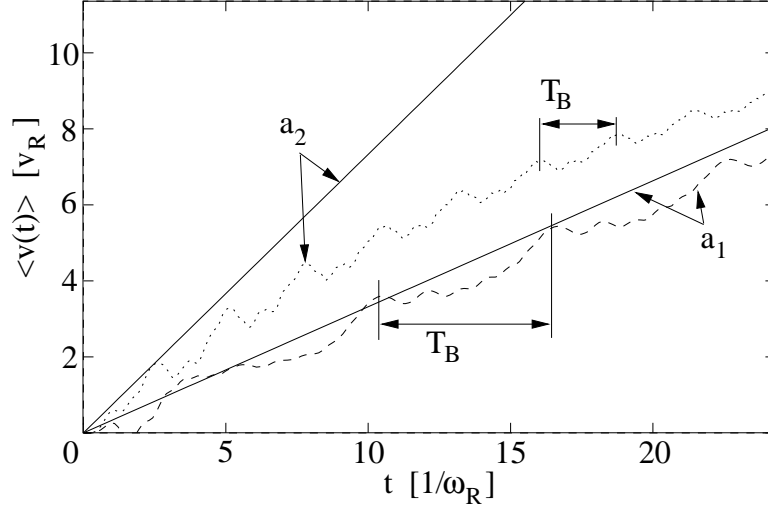


Figure 3.3: Mean velocity of a condensate with $N = 10^5$ atoms, an initial Gaussian spatial distribution of longitudinal width $w_z = 318.9/k_L$ and a transverse width $w_\perp = 31.9/k_L$. The lattice depth is chosen to be $V_0 = 2E_R$. Acceleration rates are as in Figs. 3.1 and 3.2, $a_1 = 0.33a_R$ (dashed) and $a_2 = 0.73a_R$ (dotted), together with the corresponding instantaneous lattice velocity (solid) for the two acceleration rates.

the GPE of Eq. (2.28), with the lattice potential Eq. (3.2) as an external potential,

$$i\hbar \frac{\partial}{\partial t} \psi(z, t) = \left[-\frac{\hbar^2}{2M} \frac{\partial^2}{\partial z^2} + V_0 \cos(2k_L z - \eta t^2) \right] \psi(z, t) + NU_0 |\psi|^2 \psi(z, t). \quad (3.11)$$

We solve Eq. (3.11) numerically using a split-operator technique, see Appendix A.4. We start with a condensate in a trap ground state exhibiting the same density profile as the classical ensemble considered in Section 3.2. We then assume the trapping potential to be switched off and suddenly turn on the accelerated lattice potential. The resulting mean velocity $\langle v(t) \rangle$ of the condensate is shown in Fig. 3.3 for the two acceleration rates used for the classical ensemble in Figs. 3.1 and 3.2.

We observe that the mean velocity of the condensate exhibits two major differences when compared to the case of classical particles. First, the condensate shows pronounced time-dependent oscillations that can be identified as Bloch oscillations, introduced in Section 2.5.3, with the oscillation period being consistent with Eq. (2.71) and $F = Ma_{lat}$. Since the oscillations are not clean, this indicates that the condensate dynamics involves more than just the fundamental band (which is assumed in the derivation of pure Bloch oscillations). Second, the higher of the two lattice accelerations causes $\langle v \rangle$ to converge towards a constant value, an effect due to increased Landau-Zener tunneling, as will be explained later.

The difference between the classical and quantum situations is evidenced even more strikingly in Fig. 3.4. Instead of being composed of two broad continua as in Fig. 3.2, the condensate momentum distribution $\phi(k)$, which is the Fourier transform of the spatial wavefunction $\psi(z)$, consists of a series of very narrow peaks located at integer multiples of $2k_L$. Physically, this is due to the fact that while the classical particles probe the local value of the lattice potential, the ultracold

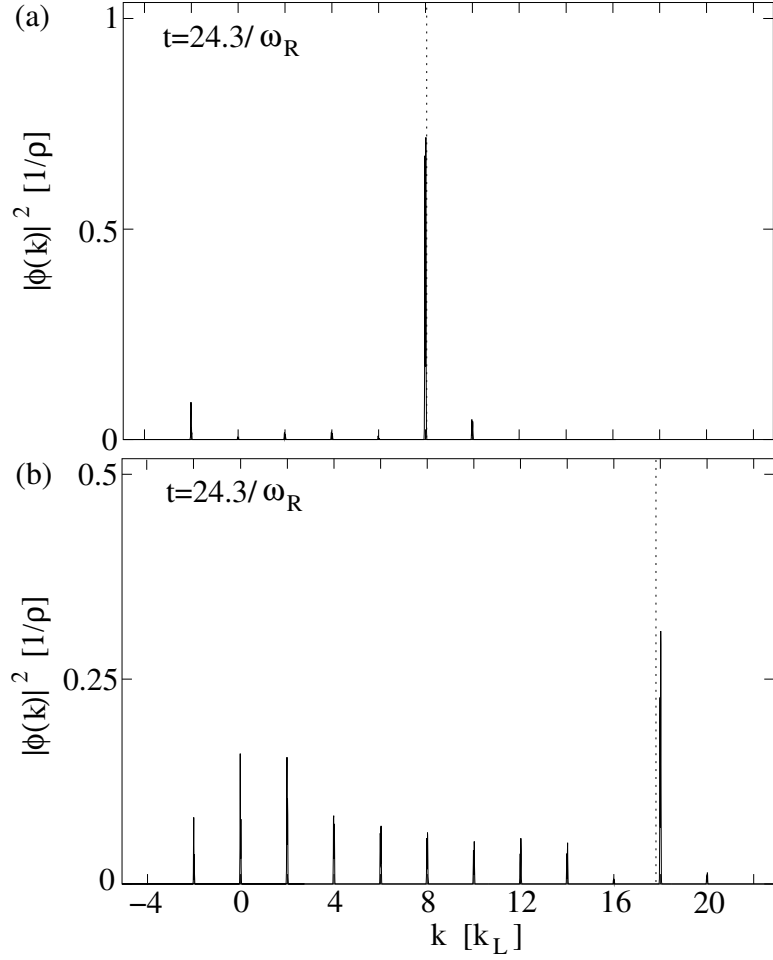


Figure 3.4: Momentum space density of an accelerated condensate at time $t = 24.3/\omega_R$ for two acceleration rates: $a_{lat} = 0.33a_R$ (a) and $a_{lat} = 0.73a_R$ (b). The characteristic density is given by $\rho = 2E_R/NU_0$, the condensate and lattice parameters are chosen as in Fig. 3.3. Included is the instantaneous lattice momentum at the time of the plot (vertical dotted line).

Bose-Einstein condensate probes a region of the lattice comprising a large number of maxima and minima, and hence its full periodicity. As such, the individual classical particles are channeled in one or the other potential well of the time-dependent potential, while the condensed atoms are diffracted by it. Their dynamics is governed by the quantum interferences that give rise to Bragg scattering, with the resulting narrow peaks of Fig. 3.4.

A central result is that after acceleration, the condensed atoms can still be largely monochromatic. The next section takes advantage of the physical difference in physics between the acceleration of quantum and classical samples to investigate ways to improve the monochromaticity of the condensate.

3.4.1 Quasimodes

With respect to atom-interferometric applications, we call an acceleration scheme ideal if it leaves all atomic population in one single momentum mode whose value is determined by the velocity v_{lat} of the optical lattice. We can therefore define a figure of merit of the accelerator as one minus the fraction of atoms in other momentum sidemodes. Fig. 3.4 suggests that we have to restrict ourselves to certain acceleration rates and times in order not to lose too many atoms. The closest we were able to approach “perfect” acceleration with our simple linear acceleration scheme is shown in the example of Fig. 3.4(a).

In the following we consider a simple coupled-mode description of the acceleration process that identifies the important parameters in its optimization. We extend the case of a static lattice as shown in Ref. [100] to accelerated ones. We start from the GPE (3.11) and introduce the momentum space condensate wave function as the Fourier transform of the spatial wave function $\psi(z, t)$,

$$\phi(k, t) = \frac{1}{\sqrt{2\pi}} \int_{-\infty}^{\infty} dz \psi(z, t) e^{-ikz}. \quad (3.12)$$

Substituting this into Eq. (3.11) we obtain the corresponding coupled difference-differential GPEs

$$\begin{aligned} i\hbar \frac{\partial}{\partial t} \phi(k, t) &= \frac{\hbar^2 k^2}{2M} \phi(k, t) \\ &+ \frac{V_0}{2} \left[\phi(k - 2k_L) e^{-i\eta t^2} + \phi(k + 2k_L) e^{i\eta t^2} \right] \\ &+ \frac{NU_0}{2\pi} \int dk_1 dk_2 \phi(k - k_1 + k_2, t) \phi(k_1, t) \phi^*(k_2, t). \end{aligned} \quad (3.13)$$

From Eq. (3.13) we observe that the optical lattice couples states separated in momentum by $k = \pm 2k_L$. Together with the fact that the initial momentum distribution of the condensate is much narrower than k_L , i.e. $\Delta k \ll k_L$, since the spatial extent of the condensate that we have in mind is large compared to the lattice period π/k_L , this leads to a momentum distribution consisting in general of a “comb” of narrow peaks. Ground state collisions lead to a broadening of these peaks, but for small enough particle numbers N , it can be expected that this broadening remains small compared to $2k_L$. This suggests that it is useful to expand the momentum space condensate wave function on a basis of *quasimodes* described by the mode functions

$$u_n(k) = \frac{1}{\sqrt{2k_L}} \{ \Theta[k - (2n - 1)k_L] - \Theta[k - (2n + 1)k_L] \}, \quad (3.14)$$

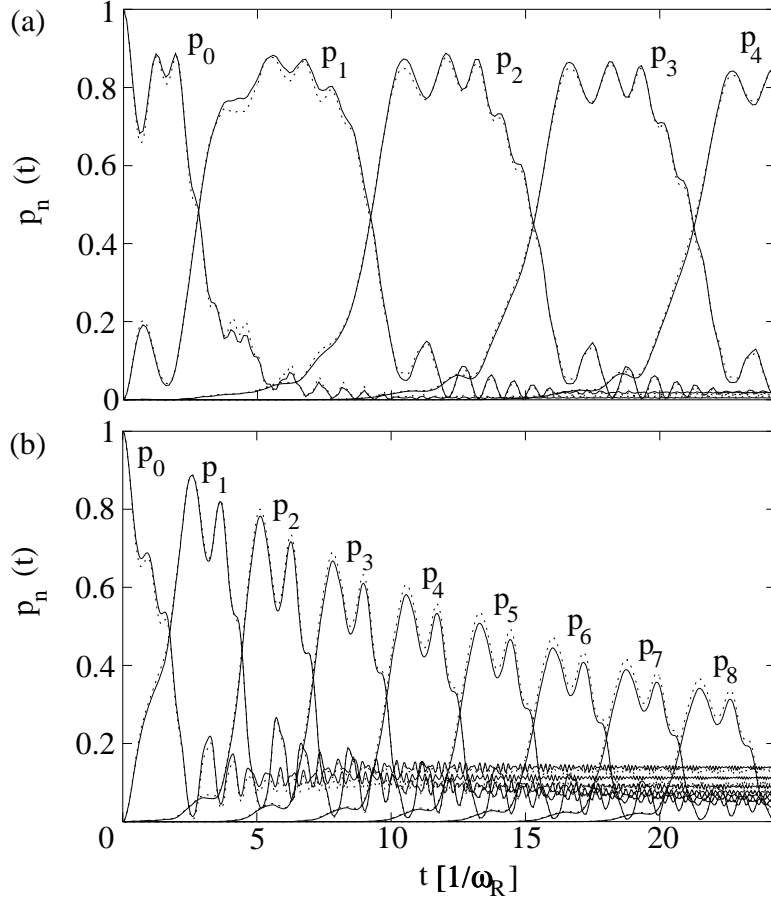


Figure 3.5: Temporal evolution of the quasimode population for a condensate accelerated at rates $a_{lat} = 0.33a_R$ (a) and $a_{lat} = 0.73a_R$ (b). The condensate and lattice parameters are chosen as in Fig. 3.3. Shown is the solution of the truncated coupled-mode equations from Eq. (3.20) (dotted) and the direct solution of the GPE in Eq. (3.11) (solid).

The diagonal elements of $\mathbf{H}(t)$, which are responsible for the explicit time-dependence of the coupling Hamiltonian, are given by

$$\omega_n(t) = 4\omega_R n^2 - 2n\eta t. \quad (3.23)$$

Finally, we can define the detuning Δ_n between adjacent modes as

$$\Delta_n(t) = \omega_{n+1}(t) - \omega_n(t) = 4\omega_R(2n+1) - 2\eta t. \quad (3.24)$$

Equation (3.20) describes Bragg scattering of atoms off the periodic optical lattice. First-order Bragg resonances occur whenever one of the detunings $\Delta_n(t)$ in Eq. (3.24) becomes equal to zero. We observe that these detunings depend explicitly on time, due to the acceleration of the optical potential. As a result of the linear acceleration, neighboring pairs of modes are therefore successively moved in and out of resonance, so that in contrast to the case of classical particles, the physical process underlying the atomic acceleration consists of successively tuned and detuned Bragg resonances.

This sequence of resonances is illustrated in Fig. 3.5, which shows the evolution of the population dynamics of a few momentum sidemodes of the condensate for the two acceleration rates of Figs. 3.1- 3.4. The solid lines give the results of a truncated coupled-modes analysis, while the dotted curves show the results of the direct solution of the GPE Eq. (3.11), in which case the various sidemode populations are calculated from

$$p_n(t) = \int_{(2n-1)k_L}^{(2n+1)k_L} dk |\phi(k, t)|^2. \quad (3.25)$$

The two approaches are in very good agreement, despite the fact that the coupled-mode analysis included only eight modes in the present example and neglected the nonlinearity. Figure 3.5(a) clearly illustrates the successful sequential population transfer towards sidemodes of higher momentum. In contrast, Fig. 3.5(b) shows a sequential loss for each transfer between two neighboring modes, leaving population in lower modes, a result of the fact that after some time these modes are far-off resonance from any other mode.

3.5 Loss mechanisms in condensate acceleration

With the help of the coupled-mode approach we identified sequential Bragg resonances as the physical mechanism that accelerates the condensates. With this understanding, we now explain several processes that cause a loss of monochromaticity. Specifically, we investigate the one-time loss caused by the sudden switch-on of the lattice and discuss the dynamical loss caused by incomplete Bragg scattering and Landau-Zener tunneling, respectively.

3.5.1 Initial loss: Sudden lattice switch-on

If a condensate in the trap ground state is suddenly loaded into a lattice, it will not be located in its lowest band, but rather in a superposition of Bloch states of the general form

$$\psi(z) = \sum_{n,k} a_{nk} \varphi_{nk}(z), \quad (3.26)$$

where $\varphi_{nk}(z)$ are the Bloch functions defined in Eq. 2.57. We obtain the expansion coefficients a_{nk} by projecting the condensate wave function onto the Bloch functions,

$$a_{nk} = \int dz \varphi_{nk}^*(z) \psi(z). \quad (3.27)$$

The probability of finding the condensate in band n with momentum k is then given by $|a_{nk}|^2$. Since we assume the condensate at $t = 0$ to be highly localized in momentum space, we can approximate it by a plane wave with wave vector k_0 ,

$$\psi(z, t = 0) = \frac{1}{\sqrt{L}} e^{ik_0 z}, \quad (3.28)$$

where we consider the plane wave to be defined on a finite one-dimensional domain of length L in order to normalize the wave function. This plane wave approximation enables us to easily calculate the decomposition into Bloch functions of different bands, as shown in Fig. 3.6 for a condensate initially at rest, $k = 0$. Right after the lattice is suddenly switched on, a large fraction of the condensate remains in the fundamental band $n = 0$. However, around 10% of the atoms are excited to the

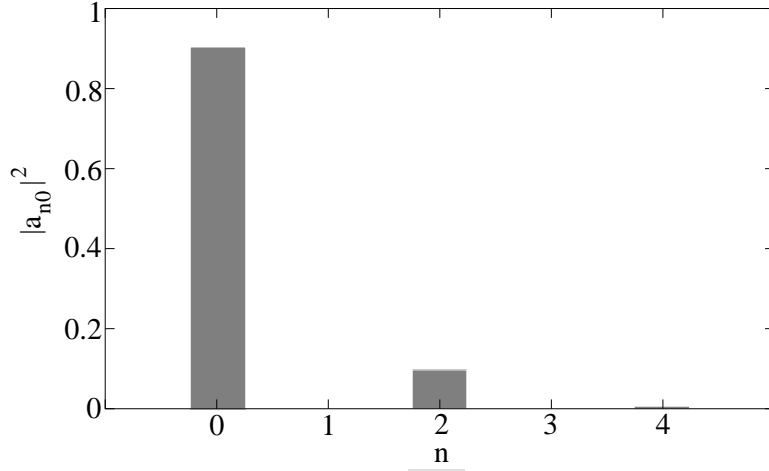


Figure 3.6: Initial state decomposition of u_0 into Bloch functions at $k = 0$ for a lattice of depth $V_0 = 2E_R$.

$n = 2$ band. This excited band is a quasi-free band for the choice of $V_0 = 2E_R$, as illustrated in Fig. 2.4. Atoms in this band do not feel the lattice potential and cannot be accelerated. Thus, the sudden switch-on of the lattice is a considerable source of loss, regardless of the acceleration rate. However, it only occurs once, and can be circumvented by ramping up the lattice adiabatically so that the condensate remains in the fundamental band. The decomposition into Bloch states has recently been measured experimentally for sudden switch-on and adiabatic loading [2].

3.5.2 Dynamical loss

Whereas the sudden switch-on of the lattice causes a one-time loss, there are loss processes that occur over the whole duration of the acceleration. This incomplete transfer for high acceleration rates can be explained in two ways: A crude but qualitative argument emerges from the coupled-mode picture, whereas the analysis of Landau-Zener tunneling provides a good quantitative estimate of the loss rate.

Incomplete Bragg scattering

Ignoring for now all but the two adjacent modes u_n and u_{n-1} , we observe that they couple with a time-dependent Rabi frequency Ω_n given by

$$\Omega_n(t) = \frac{1}{2} \sqrt{\tilde{V}_0^2 + \Delta_n^2(t)}. \quad (3.29)$$

We can gain insight into the time scale of this coupling mechanism by introducing an averaged Rabi frequency $\bar{\Omega}$ over the interval $t_R = 1/\tilde{\eta}$, the time it takes the system to move from one Bragg resonance to the next, see Eq. (3.24),

$$\bar{\Omega} = \frac{1}{t_R} \int_{t_n}^{t_n+t_R} dt \Omega_n(t), \quad (3.30)$$

where $t_n = (n-1)/\tilde{\eta}$. Hence, one can expect that a close to optimal mode-to-mode coupling should correspond to

$$\bar{\Omega} t_R \approx \pi, \quad (3.31)$$

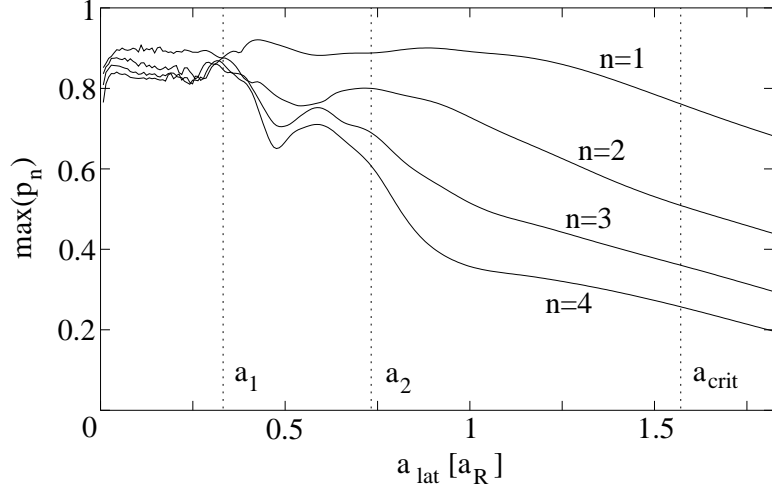


Figure 3.7: Maximum population of the i th mode as a function of acceleration, obtained from the truncated coupled-mode equations, with $a_1 = 0.33a_R$ and $a_2 = 0.73a_R$.

since in this case the system can complete half of an averaged Rabi cycle in the time it takes to move from one Bragg resonance to the next. The complete population of one mode is then approximately transferred to the next mode, thereby increasing the momentum of the condensate by $2\hbar k_L$. If the lattice acceleration is too fast for this Rabi transfer to fully occur, lower momentum modes remain significantly populated. This is the case in the example of Figs. 3.4(b) and 3.5(b). We have mentioned in the context of Fig. 3.5(b) that once a momentum sidemode is shifted out of resonance, its population remains practically constant. This accounts for the saturation in $\langle v \rangle$ shown in Fig. 3.3. In contrast to the classical case where all atoms that are captured in a potential well remain captured, here, in the quantum regime, atoms initially accelerated may gradually be moved out of resonance, after which they retain a constant velocity.

Figure 3.7 summarizes the results of a numerical optimization of the lattice acceleration rate. It confirms that if the acceleration rate is too large one can only transfer a small fraction of the population to the next mode, while if it is too small we couple to modes with negative momentum, as manifested in the small dip in all curves near the origin. The plateau-like feature defines the regime of efficient coupling, where around 85% of the population is transferred.

The derivation of the critical acceleration rate a_{crit} that is indicated in Fig. 3.7 will be given in the following section on Landau-Zener tunneling.

Landau-Zener tunneling

Another explanation for this dynamical loss is given by Landau-Zener tunneling, as described in Section 2.5.4. Since the lattice depth $V_0 = 2E_R \leq 10E_R$ that we use throughout this chapter is within the perturbative regime, the band gap between the two lowest bands is $\Delta\epsilon_1 \approx V_0$, see Section 2.5.1. The tunneling rate P_1^{LZ} from Eq. (2.72) between these two bands is then

$$P_1^{LZ} = \exp\left(-\frac{a_{crit}}{a_{lat}}\right) \quad \text{with} \quad a_{crit} = \frac{\pi V_0^2 a_R}{8E_R^2}, \quad (3.32)$$

the critical acceleration corresponding to a tunneling probability of $P_1^{LZ} = 1/e \approx 37\%$. With our particular choice of $V_0 = 2E_R$ we have $a_{crit} = \pi a_R/2$, which is also indicated in Fig. 3.7. For the small acceleration rate $a_{lat} = 0.33a_R$ that we used throughout the chapter we obtain a tunneling loss $P_1^{LZ} \approx 0.9\%$. This explains the efficient transfer as seen e.g. in Fig. 3.5(a). We conclude that our calculated overall efficiency of around 85% is mainly due to the initial loss caused by the sudden switch-on of the lattice. For the higher acceleration rate $a_{lat} = 0.73a_R$ we have a loss rate of $P_1^{LZ} \approx 12\%$, in good agreement with Fig. 3.5(b). The constant loss occurs for each mode-to-mode transfer, every time the band gap is passed. Atoms tunneling to the higher band are quasi-free and are no longer accelerated.

3.6 Nonlinear effects

Until now we assumed the nonlinearity to be small, so that the linear coupled-mode approach is valid. The situation changes drastically once the nonlinearity is increased, and new loss effects occur. The main reason for this is that a freely evolving condensate that is released from a trap converts its mean field energy into kinetic energy. The time scale over which this conversion takes place is determined by the chemical potential μ of the condensate,

$$t_\mu \approx \frac{\hbar}{\mu}. \quad (3.33)$$

Although in our case the condensate evolves in an optical lattice potential in contrast to free space, it was shown in Ref. [100] that t_μ is still a good estimate under these conditions.

The first implication of the energy conversion is that the initially narrow modes broaden, as can be observed in Fig. 3.8(a) which shows a broad continuum in momentum space rather than localized modes. In this case we have $t_\mu = 0.23/\omega_R$. This time is smaller by an order of magnitude than the time $t_\mu = 4.65/\omega_R$ for the condensate used in Fig. 3.4(a), in which case the modes experience almost no broadening. A fast broadening of the modes also leads to increased losses, since the tails of the modes move themselves out of the Bragg resonance.

In addition to this broadening, the mean field energy decreases the actual energy gap by an amount μ , so that higher tunneling rates occur. As long as $\mu \ll V_0$, the nonlinearity has almost no effect on the tunneling rate, as illustrated in Fig. 3.4(a), where $\mu = 0.215E_R \ll V_0 = 2E_R$. In Fig. 3.8(a) in contrast, $\mu = 4.3E_R$ is on the order of the gap and we have extremely high loss rates of around 25% for the first few transfers. This is despite the fact that the acceleration rate $a_{lat} = 0.33a_R$ alone only predicts a loss of 0.9%, as discussed in Section 3.5.2. After $t \approx 15/\omega_R$ the loss rate decreases. This is due to the fact that the mean field energy is almost fully converted and the gap is no longer reduced. The remaining losses are then mainly due to the broad modes as mentioned above.

It is obvious that the linear coupled-mode approach does not capture these phenomena. Hence it should only be applied for acceleration times $t \ll t_\mu$ and chemical potentials $\mu \ll V_0$.

3.7 Recent experiments

Shortly after publication of our work on condensate acceleration [101], experiments of Bose-Einstein condensates in moving optical lattices were reported. In one experiment, Morsch *et al.* [1, 66] load a condensate into an accelerated optical lattice and observe Bloch oscillations as well as Landau-Zener tunneling. They also verify

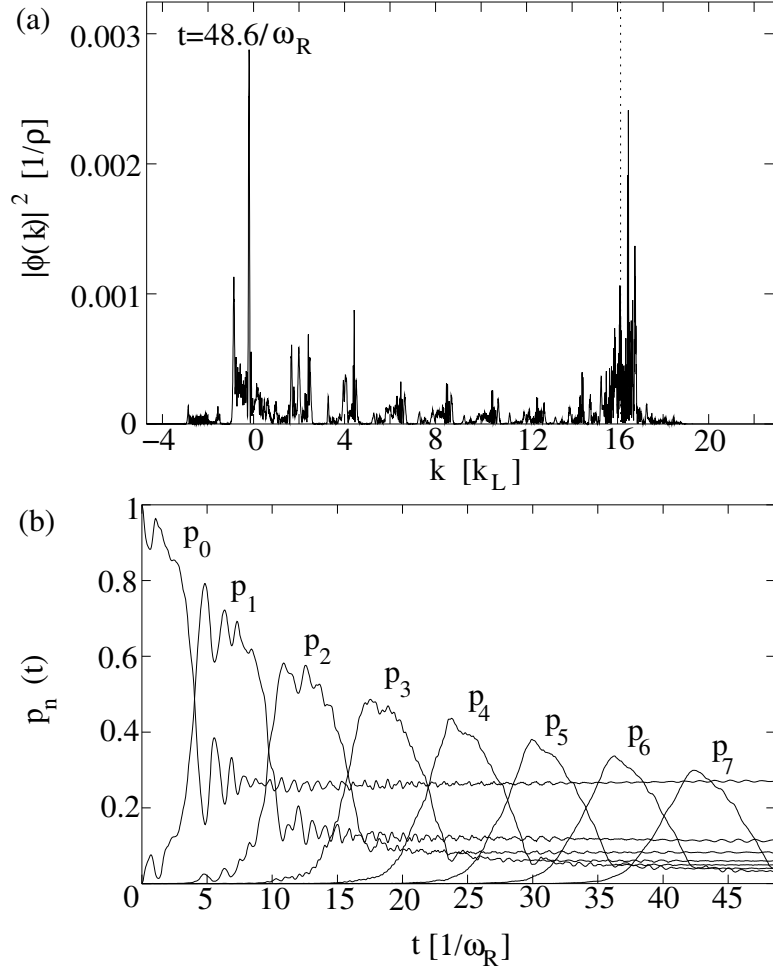


Figure 3.8: Acceleration of a condensate with $N = 2 \times 10^6$ atoms at rate $a_{lat} = 0.33a_R$. The spatial extent and lattice depth are chosen as in Fig. 3.3 and the characteristic density is given by $\rho = 2E_R/NU_0$. In (a) the instantaneous lattice momentum at the time of the plot is included (vertical dotted line).

nonlinear effects in the tunneling process predicted earlier in Ref. [93]. Their data for different lattice acceleration rates agree qualitatively with our calculations. In a second experiment, Hecker-Denschlag *et al.* [2] focus on the preparation of a condensate in prescribed lattice states. They are able to transfer population between lattice states and observe their evolution. They also use these techniques to demonstrate a condensate accelerator with a maximum transfer efficiency of around 70%, very similar to the behavior we predicted. In contrast to Refs. [1, 66] however, these experiments are performed in a regime where $t \ll \hbar/\mu$, so that nonlinear effects do not play a role.

Chapter 4

Optimized Acceleration

In the previous chapter we found that the use of a constantly accelerated lattice suffers from non-perfect transfer efficiency. We concluded that high acceleration rates as well as an effectively decreased band gap due to a large mean field energy increases the tunneling probability to free bands. Also, the sudden switch-on of the optical lattice causes initial loss to free bands. In this chapter, we discuss how these limitations can be overcome by dropping the constraint of a constant acceleration. We parametrize the time dependence of the frequency chirp between the two lattice beams, which introduces more flexibility to the system. Since the system is no longer amenable to analytic treatment, we use genetic algorithms to solve this high-dimensional optimization problem. The genetic algorithm technique has proved to be very successful in various "real world" engineering problems [102, 103], but also in the field of atomic, molecular and optical physics, where such algorithms are e.g. employed to shape laser pulses for laser chemistry [104, 105, 106, 107] and to generate and analyze ultrashort pulses [108].

After a general introduction in Section 4.1, we illustrate the usefulness of genetic algorithms with two examples: In Section 4.2, we show that a nearly perfect and fast momentum transfer is possible even for very large condensates. Then, in Section 4.3, we demonstrate that, in principle, arbitrary momentum state superpositions can be generated. Here, a prescribed relative phase between momentum states can be created by accumulating a dynamical phase, while at the same time optimizing for the prescribed mode population.

4.1 Genetic algorithms

Genetic algorithms (GA) are global optimization algorithms inspired by both, natural selection and natural genetics, and can be applied to a broad variety of problems [102, 103]. The terminology used to describe the functioning of GAs is based on several metaphors from the originating field of biological evolution. The key element of the technique is to mimic the biological principle of *survival of the fittest*. In order to achieve this goal, GA proceed by parametrizing the control function to be optimized in terms of a finite set of coefficients, or *genes*. A set of genes corresponding to a particular instance of the control function is called a *chromosome*. The GA operates on a set of chromosomes, the *population*. A *fitness function* determines how well the control function encoded in a particular chromosome fulfills the desired optimization goal. This quantitative measure of the performance of a chromosome is then used to establish a ranking among all chromosomes of a population. The algorithm then proceeds by replacing an ill-fitted fraction of the population by new chromosomes, the *offsprings*, that result from the combination

of two parent chromosomes according to some set of rules. This process is referred to as *mating*. The selection of the parent chromosomes and the mating rules have to be designed so that it is likely that both parents pass on genes that perform well, and that the offspring has a higher fitness value than the parents. In addition to this controlled combination of chromosomes, random mutations of single genes have to be implemented to prevent the algorithm from becoming trapped in local extrema. The process of evaluating the fitness, establishing a ranking and mating is iterated until a chromosome reaches a prescribed fitness value.

Genetic algorithms were first proposed in the context of atomic, molecular and optical physics in a groundbreaking article by Judson and Rabitz [104]. The authors argued that the design of laser pulses to control the motion of molecules in an experimental setup suffers from the lack of exact knowledge of the molecular Hamiltonian. They suggested the use of GA to leapfrog these difficulties: The applied laser pulses were encoded into a sequence of genes and the evaluation of the fitness of the chromosomes was determined by using the experimental apparatus as an analog computer that solves Schrödinger's equation exactly and in real time with the true laboratory parameters. The feasibility of this approach was demonstrated by numerical simulations. Later, this scheme was successfully implemented in actual experiments, see e.g. Refs. [106, 107].

Our goal is to extend the methods from the previous chapter, that use a constantly accelerated lattice to accelerate condensates, by allowing a more complex motion of the lattice. We demonstrate the usefulness of GA in this particular setup with the help of numerical simulations. The time-dependent motion of the lattice can be viewed as an extended Bragg scattering mechanism. In principle, this approach should be experimentally feasible, since Bragg scattering is already a well-established tool of atom optics: It has been used in many applications such as the determination of the coherence properties of condensates [94, 95], the implementation of Mach–Zehnder interferometers to image the condensate phase [109], the splitting of condensates [110], and the creation of initial states appropriate for nonlinear mixing processes [16].

4.1.1 The control parameter

As in Chapter 3, we base our investigations on the one-dimensional GPE with an optical lattice potential, see Eq. (3.11), but with the linear frequency chirp between the lattice laser beams replaced by its general form $\delta(t)$,

$$\begin{aligned} i\hbar \frac{\partial}{\partial t} \psi(z, t) &= \left[-\frac{\hbar^2}{2M} \frac{\partial^2}{\partial z^2} + V_0 \cos(2k_L z - \delta(t)t) \right] \psi(z, t) \\ &+ NU_0 |\psi|^2 \psi(z, t). \end{aligned} \quad (4.1)$$

In the situation at hand, the control is achieved by the time-dependent detuning $\delta(t)$. It is convenient to express the detuning by a truncated Fourier series:

$$\delta_i(t) = \sum_{\nu=1}^m a_{i\nu} \cos(2\nu\omega_R t) + b_{i\nu} \sin(2\nu\omega_R t), \quad i = 1, \dots, \mathcal{N}, \quad (4.2)$$

where ω_R is the recoil frequency defined in Eq. (2.52). Each detuning δ_i is now encoded in a chromosome c_i consisting of $n = 2m$ genes g_{ij} , each gene corresponding to one particular Fourier coefficient,

$$c_i(g_{i1}, \dots, g_{in}) = c_i(a_{i1}, \dots, a_{im}, b_{i1}, \dots, b_{im}). \quad (4.3)$$

The index i labels a specific chromosome, and the size of the chromosome population is \mathcal{N} .

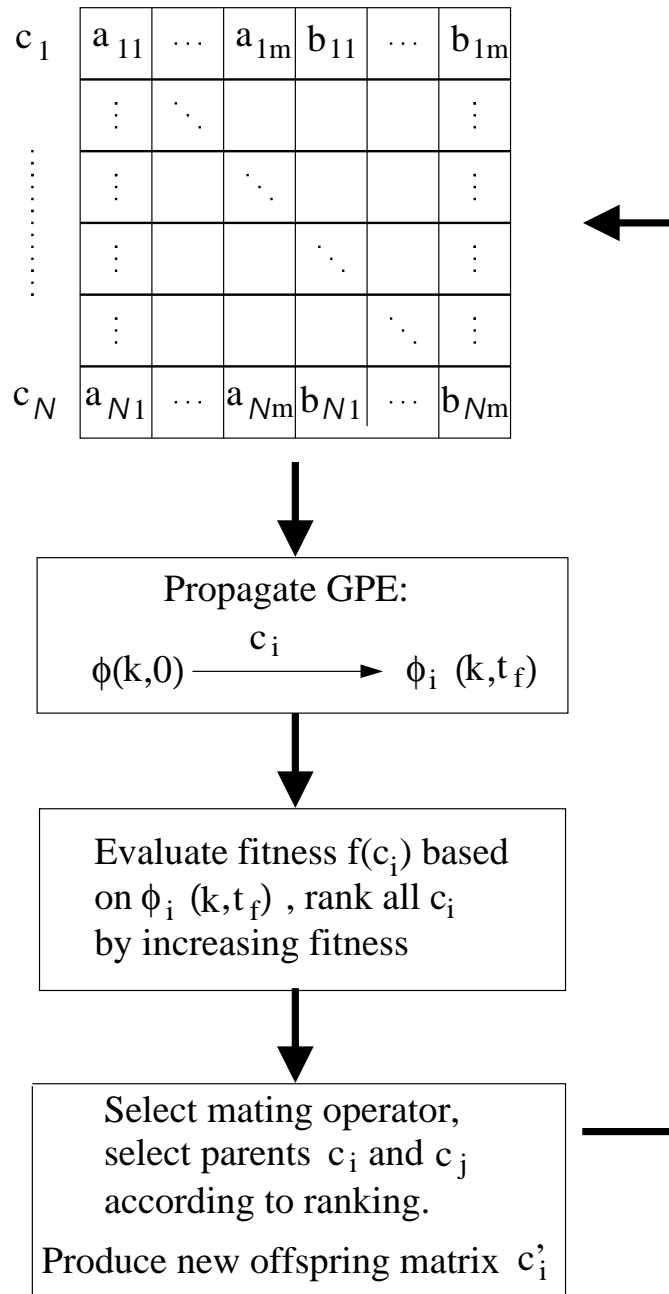


Figure 4.1: Schematics of the genetic algorithm.

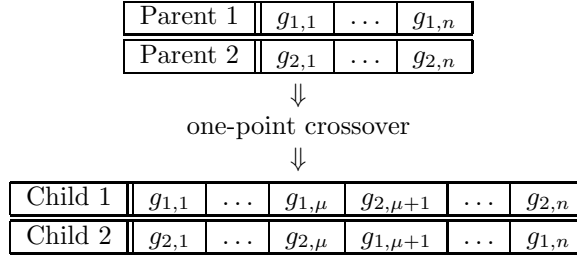
Starting from a randomly initialized population, the genetic algorithm uses a set of mating rules, mutations, and a problem-specific fitness function $f(c_i)$ to create new generations of chromosomes, as illustrated in Fig.4.1. In our problem, the fitness is evaluated by evolving an initial momentum space wavefunction $\phi(k, 0)$ according to the Fourier transformed GPE from Eq. (4.1) for a time t_f , the dynamics of the optical lattice being determined by the detuning $\delta_i(t)$. The fitness for each chromosome is then evaluated, based on the final wavefunction in momentum space $\phi(k, t_f)$, and compared to the optimization goal. If the optimum was not reached, the process is iterated. When it comes to the production of the new offspring matrix c'_i , two steps are necessary: First, parent chromosomes that are to be combined by mating operators have to be selected. This is achieved by ranking the initial \mathcal{N} chromosomes according to their fitness and using the so-called roulette wheel method [102] that assures that parent chromosomes with a high fitness are preferentially selected. Second, a group of offspring chromosomes c'_i are generated from the parent population c_i according to specified mating rules.

4.1.2 The mating operators

Mating operators perform the actual combination of parent genes into a group of offspring chromosomes, and as such, they are at the heart of the GA. Several mating operators may be considered.

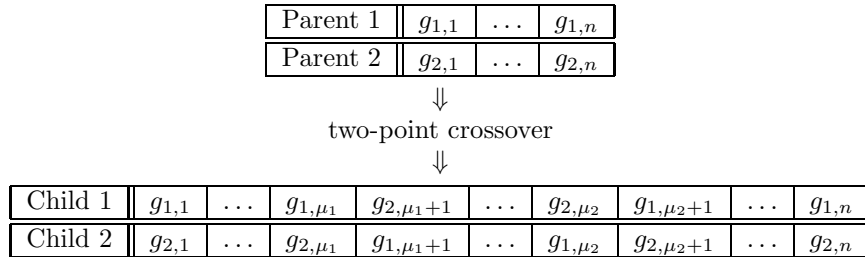
One-point crossover

The one-point crossover operator cuts the two parent chromosomes at a randomly chosen position μ ($1 \leq \mu < n$) and swaps them according to



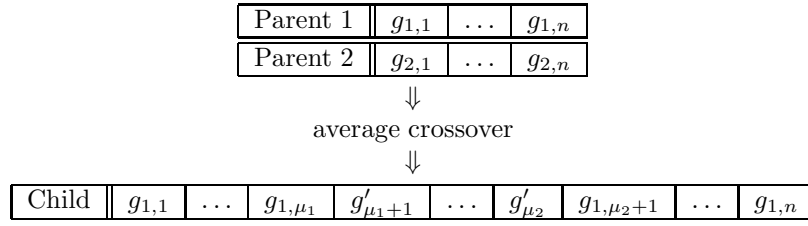
Two-point crossover

A slightly modified version of the one-point crossover is the two-point crossover that cuts the two parent chromosomes at two random positions μ_1 and μ_2 ($1 \leq \mu_1 < \mu_2 < n$), and then exchanges the genes between these two positions:



Average crossover

This mating operator produces just one offspring from the two parent chromosomes by averaging the genes between two randomly chosen positions μ_1 and μ_2 ($0 \leq \mu_1 < \mu_2 \leq n$) according to $g'_\kappa = (g_{1,\kappa} + g_{2,\kappa})/2$:

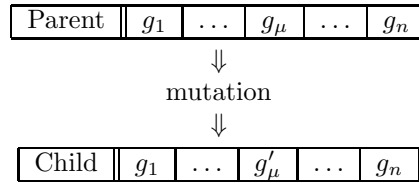


4.1.3 Randomness in offspring production

Except for the random location at which the splicing of the chromosome occurs, the mating operators discussed so far are deterministic. Since a deterministic offspring production can lead the GA to converge in a local rather than a global optimum, we require in addition truly random operators. These operators randomly change single genes with the intention to push chromosomes that are close to a local optimum into a different region of the search space. Although this might decrease the current fitness of the chromosome, it enables the GA to explore the whole search space for global optima. In the problem at hand, we introduce two operators, the “classical” operator *mutation* and a modified mutation operator *creep*.

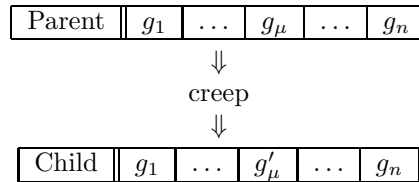
The mutation operator

The mutation operator produces one offspring from one parent by replacing a gene by a random number g'_μ within predetermined bounds $g'_{min} \leq g'_\mu \leq g'_{max}$. The probability of this process to take place is given by the *mutation rate*.



The creep operator

The creep operator also produces one offspring from one parent by changing its genes with a certain rate, the *creep rate*. In contrast to the mutation operator, the creep operator does not replace the gene by a totally random value but rather shifts the old value g_μ by a random amount, $g'_\mu = g_\mu + (0.5 - r)p_{creep}$. Here p_{creep} is a parameter that controls the range of the shift and $0 \leq r \leq 1$ is a random number.



The operators discussed in this section are the most common ones in GA optimization and the only ones used in our analysis. Note that this set of operators can in principle be applied to a broad range of optimization problems, but custom-tailored mating operators can be designed that are better suited for a particular task [111].

4.1.4 Operator selection

When it comes to selecting a specific mating operator or mutation operator, there are basically two possibilities: The first one consists of assigning fixed weights to the

available operators and then choosing randomly among them. This is a straightforward approach, but it suffers from the problem of not discriminating against mating operators that do not perform well for the optimization problem at hand. Thus, a second possibility is to dynamically adjust the operator weights over the course of the optimization [102, 111]. This guarantees that the best suited operators are applied and allows one to test the performance of new mating operators. This is done by assigning an adjustable *operator fitness* to each mating operator under consideration. As such, the mating operators are selected according to their fitness the same way as the parent chromosomes are picked. We make use of this adaptive approach. The details of the procedure used in our simulations are discussed in Appendix B.

4.2 Optimized coherent acceleration

We now apply GA optimization to the manipulation of the state of a Bose-Einstein condensate in a chirped optical lattice. As a first example, we consider the coherent transfer of a condensate population between the adjacent quasimodes u_0 and u_1 . Our motivation here is to overcome difficulties experienced with a constantly accelerated lattice as discussed in Chapter 3.

For the sake of illustration, we assume that the condensate is initially in the zero-momentum quasimode, $p_0(t=0) = 1$ according to the definition in Eq. (3.18), and seek a time-dependent detuning such that $p_1(t_f) = 1$ after some predetermined time t_f . In that case, the algorithm fitness has the simple form

$$f(c_i) = p_1(t_f), \quad (4.4)$$

with an optimal value of unity.

Figure 4.2 summarizes the results of the optimization procedure. It compares the optimized population transfer of a large condensate consisting of 2×10^6 atoms (spatial extent and atom number are chosen as in Fig. 3.8) to the case of the same condensate subject to on-resonance Bragg scattering. In this example, the genetic algorithm involved a one-point-crossover, a two-point-crossover and an average cross-over mating operator. In addition, it included two mutation operators with mutation rates of 0.8 and 0.4, and two creep operators, both at a rate of 0.9, but different creep parameters: a “coarse” creep with $p_{\text{creep}} = 0.01$ and a “finer” creep operator with $p_{\text{creep}} = 0.001$. More details of the simulations are given in Appendix B. While it can be expected that resonant Bragg scattering at the appropriate frequency transfers almost perfectly the population of a small condensate from mode u_0 to mode u_1 , such is not the case for the large condensate we investigated (dashed line in Fig.4.2(b)). In this case, the mean-field nonlinearity of the condensate is no longer negligible. It dynamically shifts the Bragg resonance, see Chapter 3 and Ref. [100], so that the transfer efficiency drops to barely over 90% and the maximum transfer occurs later in time. It is in such nontrivial situations that genetic algorithms are expected to be useful. Indeed, the optimal time-dependent detuning $\delta(t)$ found by the genetic algorithm is highly non-trivial. The temporal dependence of the detuning $\delta(t)$, which transfers more than 99% of the population to the quasimode u_1 , reveals that while it is initially advantageous to remain close to the Bragg resonance frequency, as indicated by the rather flat portion of the detuning, it eventually becomes necessary to drastically couple the condensate atoms to higher momentum modes so as to drag the remaining population to the final state u_1 . The relatively fast initial increase of the detuning above the level of the first Bragg resonance makes up for the fact that at $t = 0$ we start with zero detuning and couple partially to the mode of negative momentum u_{-1} . Note that the optimized detuning successfully counteracts the sudden switch-on of the lattice at

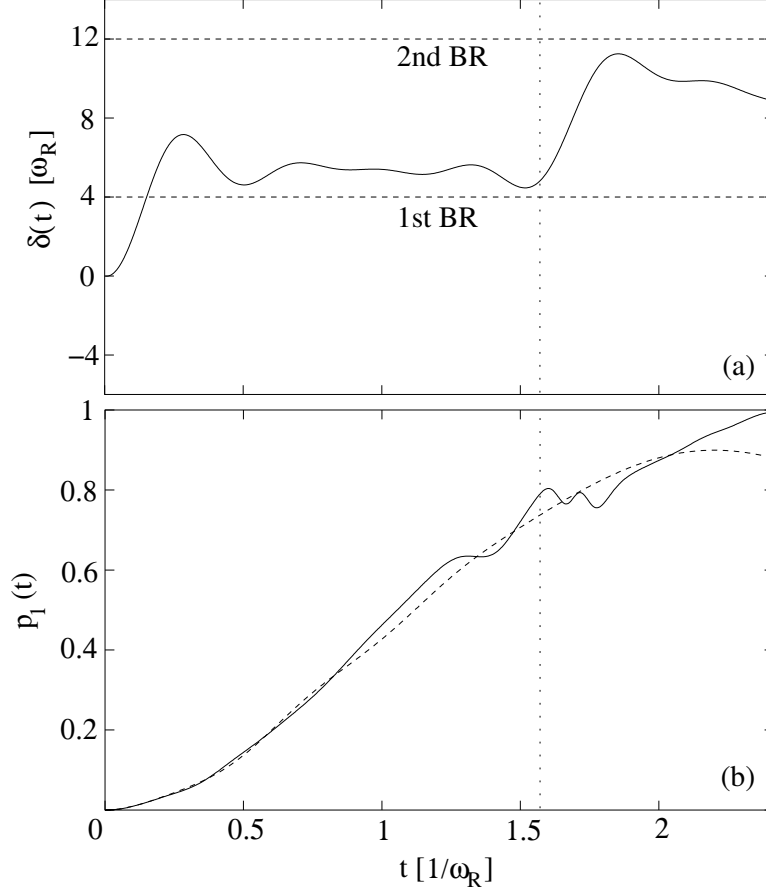


Figure 4.2: Momentum transfer of a condensate with $N = 2 \times 10^6$ atoms, and a Gaussian spatial distribution of longitudinal width $w_z = 318.9/k_L$ and transverse width $w_\perp = 31.9/k_L$; $V_0 = 2E_R$ (same parameters as in Fig. 3.8) over a duration of $t_f = 2.41/\omega_R$. (a) The optimized time-dependent detuning (solid) and the first and second Bragg resonance (BR) for reference (dashed). (b) Temporal evolution of the mode population p_1 for: On resonance (dashed) and optimized (solid). Indicated in (a) and (b) is the time it takes to resonantly transfer all population from the quasimode u_0 to u_1 if the two modes were a linear two-mode system (vertical dotted line).

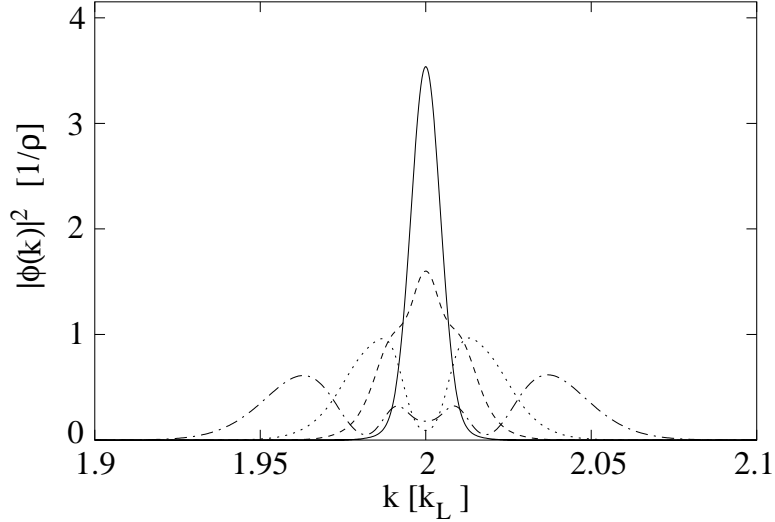


Figure 4.3: Effect of the nonlinearity on the momentum space wave function: Momentum space densities within quasimode u_1 after optimizing the transfer, so that $p_1 > 0.99$ after time $t_f = 2.41/\omega_R$; $N = 10^5$ (solid), $N = 5 \times 10^5$ (dashed), $N = 10^6$ (dotted), and $N = 2 \times 10^6$ (dashed-dotted). The condensate density is given in units of $\rho = 2E_R/NU_0$ for $N = 10^5$.

$t = 0$ and prevents initial loss to free bands, in contrast to the situation described in Section 3.5.1. All condensate atoms are accelerated to a final velocity of $2v_R$ during a time $t_f = 2.41/\omega_R$, corresponding to an averaged acceleration of $0.83a_R$. This acceleration rate is larger than the already lossy acceleration of $0.73a_R$ for fewer atoms (and thus a smaller nonlinearity) from Figs. 3.4(b) and 3.5(b). According to Eq. (3.32), we would have expected a tunneling loss of around 15% if a constant acceleration of this strength had been used. The use of an optimized detuning not only overcomes the obstacles encountered in Chapter 3, caused by a sudden lattice switch-on and large mean field energies, but even beats the Landau-Zener tunneling rate and provides a faster transfer.

The effect of the mean-field energy is further illustrated in Fig. 4.3, which shows the final momentum distribution $\phi(k)$ within the quasimode u_1 for various numbers of atoms in the condensate for optimal transfer. While this distribution remains extremely narrow compared to the quasimode width $2k_L$, collisions lead to a substantial reshaping and broadening within that mode.

4.3 Coherent superposition engineering

In a second application, we set out to design an equal-weight superposition of the two quasimode states u_0 and u_1

$$\phi(k, t_f) = \frac{1}{\sqrt{2}} (u_0 e^{i\varphi_0} + u_1 e^{i\varphi_1}), \quad (4.5)$$

with a prescribed relative phase $\Delta\varphi = \varphi_1 - \varphi_0$. In contrast to the previous example, we now want to control two properties of the quantum state, the relative phase as well as the population in each state. Whereas the principles of population transfer

have been demonstrated in the previous section, a relative phase can be created by controlling the dynamic phase that each mode accumulates over the course of the evolution of the system. The fitness function to be optimized has to monitor both population and phase properties, and is therefore more complicated.

We choose to employ a penalty function $\mathcal{P}(c_i)$ for the optimization of the quasi-mode populations [103]. The goal of $\mathcal{P}(c_i)$ is to decrease the fitness of chromosomes that do not fulfill the desired requirements, thereby steering the population towards the target values. A prototype penalty function is

$$\mathcal{P}(c_i) = \begin{cases} 1.5 & : p_0(c_i), p_1(c_i) > 0.465 \\ 1.0 & : p_0(c_i), p_1(c_i) > 0.47 \\ 0 & : p_0(c_i), p_1(c_i) > 0.475 \\ 100 & : \text{else.} \end{cases} \quad (4.6)$$

The fitness function for this optimization problem is then given by

$$f(c_i) = 1 - |\alpha(c_i) - \Delta\varphi| - \mathcal{P}(c_i), \quad (4.7)$$

where, as we recall, c_i corresponds to a specific realization of the time-dependent detuning $\delta(t)$ and $\alpha(c_i)$ is the relative phase corresponding to this realization. This fitness function reaches its maximum, unity in this case, when the populations are within the specified range and the phase difference is exactly as prescribed. The results for the optimization for the two cases $\Delta\varphi = -\pi/2$ and $\Delta\varphi = -\pi/4$ are shown in Fig. 4.4. For the genetic algorithm we used the same operators and parameters as in Section 4.2. More details of the simulations are given in Appendix B.

Fig. 4.5 shows the momentum distribution $\phi(k)$ within each of the two quasi-modes u_0 and u_1 of the condensate, as well as the corresponding phases for the case $\Delta\varphi = -\pi/2$. Clearly, the genetic algorithm converges to the stated goal, and produces a condensate in the desired coherent superposition.

In particular, we observe that the relative phase of the two components is approximately constant in the region where the condensate wave function is different from zero. The optimization goal of $\Delta\varphi = -\pi/2$ is achieved with an accuracy of over 99% at the center of the mode. The curvature of the phase at the wings of the wave function is due to nonlinear phase shifts accumulated during the Hamiltonian evolution. It could be reduced by further decreasing the density of the condensate.

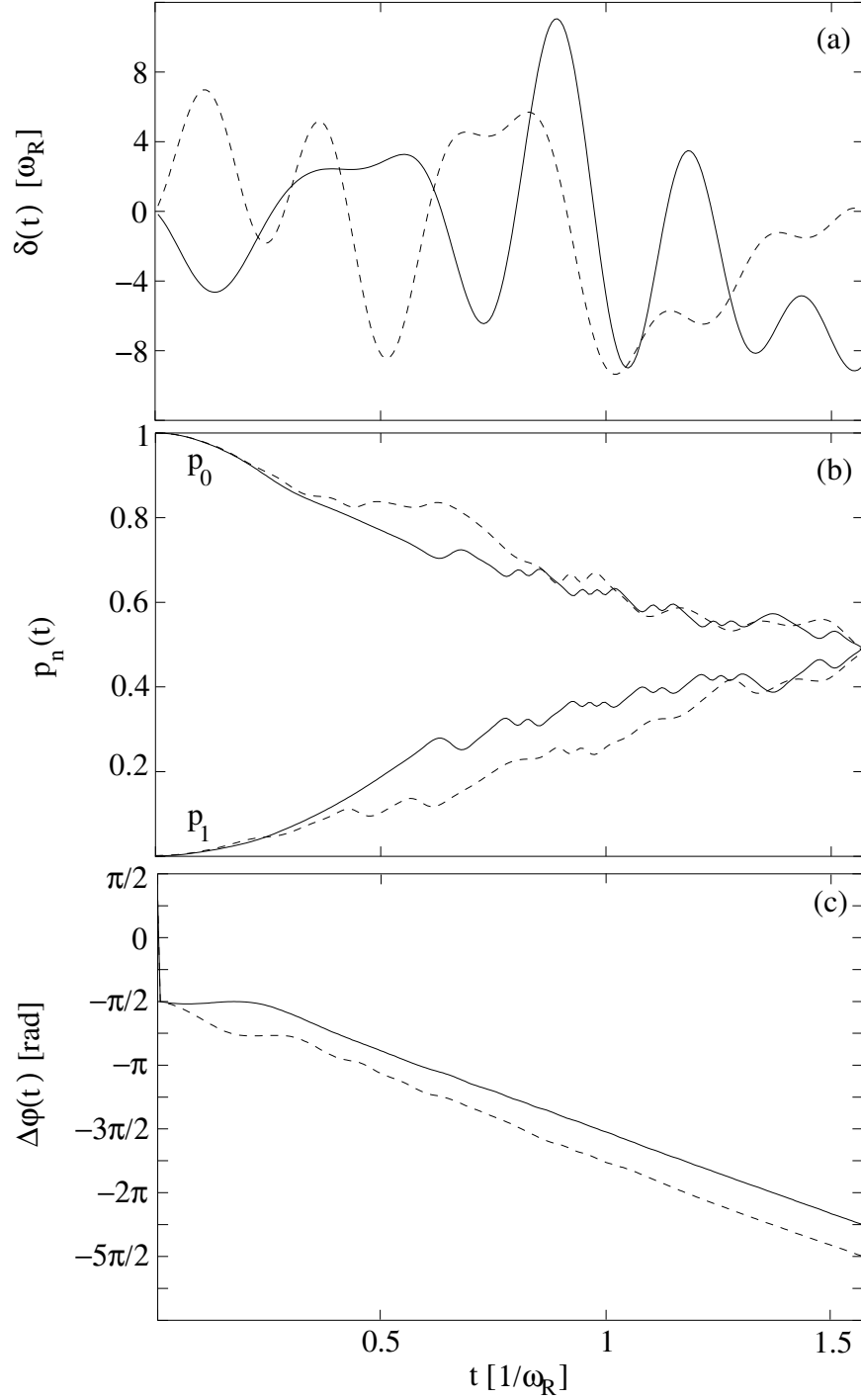


Figure 4.4: Excitation of an equal-weight coherent superposition of momentum states with relative phases, $\Delta\varphi = -\pi/4$ (solid) and $\Delta\varphi = -\pi/2$ (dashed). The condensate consists of $N = 5 \times 10^4$ atoms with an initial Gaussian distribution of longitudinal width $w_z = 637.9/k_L$ and transverse width $w_\perp = 31.9/k_L$; $V_0 = 2E_R$. (a) Optimized time-dependent detuning used to create the superposition. (b) Temporal evolution of the mode population of the two involved modes. (c) Temporal evolution of relative phase of the two quasimodes at the center of their momentum distribution, see also Fig. 4.5.

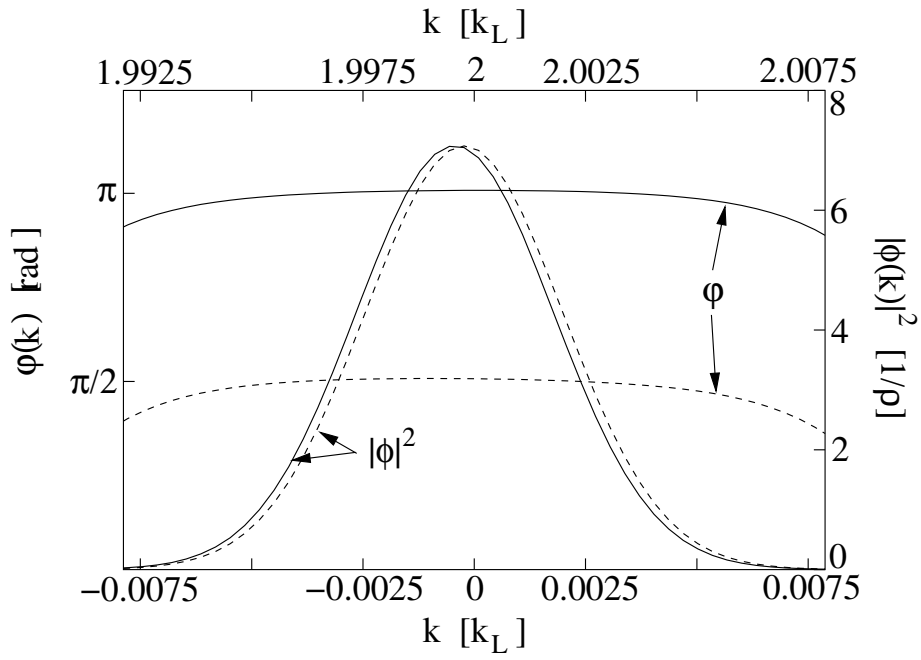


Figure 4.5: Density profiles and phases of the two momentum modes after the optimization at $t = t_f$ for the parameters used in Fig. 4.4. The lower abscissa corresponds to the momentum wave function $\phi(k)$ with phase φ_0 within quasimode u_0 (centered around $k = 0$), the upper to $\phi(k)$ with phase φ_1 within u_1 (centered around $k = 2k_L$). Note that $p_0(t_f), p_1(t_f) \geq 0.475$.

Chapter 5

Dispersion-free Transport: Gap Solitons

Having discussed the acceleration of condensates and the engineering of specific momentum states in the previous chapters, we now focus on the transport of wave packets. In free-space atom-optical applications as well as in atomic waveguides it is desirable to minimize the dispersion of a traveling wave packet. This can be achieved by non-spreading solutions of the nonlinear equation of motion, which are as we recall solitons [112]. These are well-known from nonlinear optics and have been demonstrated in various fiber optics experiments [113]. In solitons, the dispersive effects are balanced by the nonlinearity, and the spreading of the wave packet is canceled. In Section 5.1 we review this situation for atomic solitons: In the case of a repulsive nonlinearity the balancing gives rise to a non-spreading dip in an otherwise constant background density. These *dark solitons* were experimentally excited in Bose-Einstein condensates by optical phase imprinting [19, 20, 69]. On the other hand, *bright solitons*, non-spreading localized wave packets, exist in the presence of an attractive nonlinearity. Such solitons were created very recently in Bose-Einstein condensates by using Feshbach resonances to achieve a negative scattering length [70, 71]. However, this method is restricted to relatively small solitons, since attractive interactions cause condensates to collapse above a critical number of atoms [11, 114]. Ideally, though, it would be desirable to generate solitons carrying larger numbers of atoms. In order to circumvent this problem, we show that bright solitons exist even in the presence of repulsive interactions. This is done by loading the condensate into an optical lattice, where it can be assigned an effective mass that is inversely proportional to the local curvature of the dispersion curve [75]. If we place the Bose-Einstein condensate at a point of negative curvature, which usually occurs at a band gap, the effective mass will also be negative and can counteract the repulsive interaction. This type of soliton is called *gap soliton* [115, 116, 117, 118]. In contrast to earlier work, where we demonstrated gap solitons being composed of two Zeeman levels of a condensate that are coupled by an optical lattice [119, 120], we now focus on gap solitons consisting of superpositions of two momentum states with a fixed relative phase. In Section 5.2 we present an exact and an approximate form of stationary and moving gap solitons. The stability of the solitons is demonstrated by numerical propagation in one and three dimensions in Section 5.3. Finally, Section 5.4 discusses possible excitation schemes based on our findings and the results from Chapter 4.

5.1 Introduction to atomic solitons

We briefly review one-dimensional dark and bright soliton solutions, where we assume tight transverse confinement. Since the nonlinearity alone can balance the dispersion of the wave packet, we consider the GPE from Eq. 2.32 without an external potential,

$$i\hbar \frac{\partial}{\partial t} \psi(z, t) = \left[-\frac{\hbar^2}{2M} \frac{\partial^2}{\partial z^2} + NU_0 |\psi(\mathbf{r}, t)|^2 \right] \psi(z, t). \quad (5.1)$$

5.1.1 Dark atomic solitons

For the case of repulsive interactions ($a_{sc} > 0$, i.e. $U_0 > 0$), both the kinetic energy and nonlinear term in Eq. (5.1) tend to broaden localized wave packets, so we do not expect localized, or bright soliton, solutions for that case. However, dark solitons describing localized density dips in an otherwise constant background can arise and are given by [19, 20, 121] (with analogous solutions being well known in nonlinear fiber optics, see e.g. [113])

$$\psi(z, t) = n_0^{1/2} \sqrt{1 - (1 - v_s^2) \operatorname{sech}^2 \left(\frac{(z - v_s v_0 t)}{w_s} (1 - v_s^2)^{1/2} \right)} e^{i(\phi - \mu t/\hbar)}, \quad (5.2)$$

where n_0 is the background density away from the dark soliton core, $\mu = n_0 |U_0|$, $w_s = \sqrt{\hbar^2/M\mu}$ is the correlation length determining the width¹ of the soliton core, and $v_0 = \sqrt{\mu/M}$ is the Bogoliubov speed of sound. The group velocity v_s of the dark soliton is given in units of v_0 and bounded by $-1 < v_s < 1$. The spatial phase ϕ of the soliton is given by

$$\phi(z, t) = -\arctan \left[\left(\frac{1}{v_s^2} - 1 \right)^{1/2} \tanh \left(\frac{(z - v_s v_0 t)}{w_s} (1 - v_s^2)^{1/2} \right) \right]. \quad (5.3)$$

Figure 5.1 (a) illustrates the density distribution $|\psi(z)|^2$ of a dark soliton for various velocities, and Fig. 5.1 (b) shows the corresponding spatial phases $\phi(z)$. These solutions show that the dark solitons are characterized by the presence of a phase-step δ across the localized density dip. It can be related to the velocity v_s and the density n_{bot} at the bottom of the atomic density dip [19, 20]. In particular, one finds the relation

$$\cos \left(\frac{\delta}{2} \right) = v_s = \frac{n_{bot}}{n_0}, \quad (5.4)$$

so that for a stationary soliton with $v_s = 0$ and a vanishing density at the bottom, $n_{bot} = 0$, there is a steep $\delta = \pi$ phase-step (solid curves in Fig. 5.1). Only stationary solitons have a vanishing density at their center, so they are also referred to as *black* solitons, whereas for moving solitons with $n_{bot} > 0$ the expression *grey* soliton is used. Also, only stationary solitons have a sharp phase step across the center, whereas moving solitons exhibit a smoother phase step.

Dark matter-wave solitons have been observed experimentally in a sodium condensate by Denschlag *et al.* [20], and in a cigar-shaped rubidium condensate by Burger *et al.* [19]. In both experiments dark solitons of variable velocity were launched via the phase imprinting of a condensate by a light-shift potential. By

¹In this chapter we use the convention that w_s refers to the width of a hyperbolic secant. The full width at 1/e of the maximum of a squared hyperbolic secant is then given by $2.17w_s$, 2.17 being a numerical conversion factor. This conversion relates the width of hyperbolic secant-shaped density distributions to the width of a Gaussian density distribution as defined in Chapter 2.

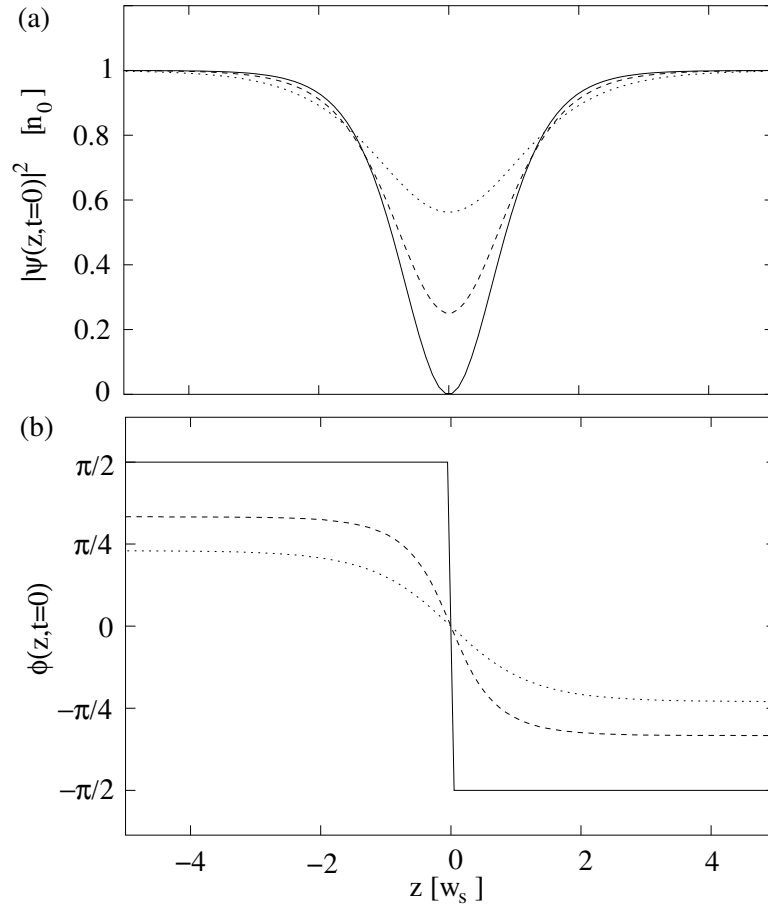


Figure 5.1: (a) Density and (b) phase of dark soliton according to Eqs. (5.2) and (5.3) at $t = 0$ for different soliton velocities: $v_s = 0$ (solid), $v_s = 0.5$ (dashed), and $v_s = 0.75$ (dotted).

applying a pulsed laser to only half of the Bose-Einstein condensate and choosing the laser intensity and duration to imprint a desired phase-step δ , the soliton velocity could be selected according to Eq. (5.4). Ideally, imprinting a phase step of π should lead to a stationary dark soliton, but the experiments were carried out in a harmonic trap [122] where dissipative effects were shown to accelerate the solitons [123, 124]. The solitons then decayed before reaching the edge of the condensate. Note that the subtle interplay between density distribution and the spatial phase is crucial for the successful excitation of the solitons, a fact that becomes very important when discussing means to excite atomic gap solitons in Chapter 5.4.

5.1.2 Bright atomic solitons

For the case of attractive interactions ($a_{sc} < 0$, i.e. $U_0 < 0$), the kinetic energy of the condensate can be balanced by the nonlinearity, yielding spatially localized bright solitons [113, 121], i.e. non-spreading wave packets in contrast to non-spreading density dips as in the case of dark solitons. The one-parameter solution to Eq. (5.1) then reads

$$\psi(z, t) = \sqrt{\frac{1}{2w_s}} e^{i\phi(z,t)} \operatorname{sech}\left(\frac{z - v_s v_R t}{w_s}\right), \quad (5.5)$$

with $w_s = 2\hbar^2/N|U_0|M$ is the soliton width and v_s is the dimensionless velocity parameter. The phase of the bright soliton is given by

$$\phi(z, t) = \left(z - \frac{v_s v_R}{2} t\right) \frac{v_s v_R M}{\hbar} + \frac{N^2 U_0^2 M}{8\hbar^3} t, \quad (5.6)$$

exhibiting only a linear spatial dependence in contrast to the spatial phase step of dark solitons.

Recently, such bright solitons have been experimentally demonstrated in condensates of ^7Li atoms [70, 71], where the scattering length was tuned to negative values by using Feshbach resonances [125, 126, 127]. In both experiments the magnitude of the attractive interaction was chosen to excite solitons consisting of around 5000-6000 atoms. Whereas in Ref. [70] a soliton train was created and predicted interactions between the single solitons were observed, Ref. [71] excited a single soliton. Both experiments demonstrated a dispersion-free propagation over macroscopic distances. Since in two or more dimensions negative scattering lengths can lead to catastrophic collapse in homogeneous systems for large enough particle numbers, the experiments had to be performed in quasi-one-dimensional systems with strong transverse confinement, where solitons are rendered stable [128].

5.2 Momentum state gap solitons

So far in our discussion dark solitons aroused for positive and bright solitons for negative scattering lengths. However, it is possible to extend the range of options by considering a Bose-Einstein condensate in a one-dimensional optical lattice where bright soliton solutions exist even for positive scattering lengths. In general, these so-called gap solitons consist of two components that are coupled by the periodic potential. They exhibit a more complex structure than the single component solitons described in Sections 5.1.1 and 5.1.2 and their excitation process is more complicated. However, due to their complex structure, soliton properties such as width and number of atoms per soliton are less restricted and they offer more possibilities for coherent manipulation.

Historically, gap solitons were first considered in nonlinear optics where they result from the combination of an optical nonlinearity and a periodic spatial refractive-index distribution [115, 116, 117, 118]. They were then first mentioned in the

context of nonlinear atom optics by Lenz *et al.*, considering a nonlinearity caused by dipole-dipole interactions between cold atoms [129, 130]. Steel *et al.* pointed out the possibility of gap solitons in condensed atomic systems [131], where two counterpropagating components of a scalar condensate are coupled by an optical lattice. In earlier work, we discussed the existence of gap solitons in a condensed system with two magnetic Zeeman levels coupled by an optical lattice. Excitation schemes using magnetic phase imprinting were demonstrated [120, 132]. However, since coupling between the two considered Zeeman levels is hard to achieve in alkali metals [133], we return here to gap solitons consisting of a scalar condensate in two counterpropagating momentum modes. We derive detailed soliton solutions and investigate their properties. After demonstrating the soliton stability by numerical propagations studies, we develop feasible excitation schemes.

Just recently, several groups showed renewed interest in bright gap solitons in condensed systems with repulsive interactions. In particular, the existence of solitons in deep lattices [134] and methods to excite very narrow solitons, usually trains of solitons, by means of Bragg reflections were demonstrated [135, 136].

5.2.1 Coupled-mode equations

In contrast to the nonlinear optics case, where the periodicity is due to a periodically modulated index of refraction, e.g. a fiber Bragg grating, we use the optical lattice introduced in Chapter 2 as the only external potential. The one-dimensional GPE then reads

$$i\hbar \frac{\partial}{\partial t} \psi(z, t) = \left[-\frac{\hbar^2}{2M} \frac{\partial^2}{\partial z^2} + V_0 \cos(2k_L z) \right] \psi(z, t) + NU_0 |\psi(\mathbf{r}, t)|^2 \psi(z, t), \quad (5.7)$$

where we require $U_0 > 0$. We consider a weak optical lattice, $V_0 \ll E_R$, and require the atomic wavefunction to be spread over several lattice sites, thus enabling momentum modes to be coupled via Bragg scattering. Following the nonlinear optics approach [117], we look for soliton solutions ψ_s consisting of a superposition of two counterpropagating modes with momenta $\pm \hbar k_L$ of the form

$$\psi_s(z, t) = [\psi_+(z, t)e^{ik_L z} + \psi_-(z, t)e^{-ik_L z}] e^{-i\omega_R t}. \quad (5.8)$$

Substituting this ansatz for ψ_s into Eq. (5.7) and assuming that the envelope functions ψ_{\pm} for the two momentum modes vary slowly with respect to $1/k_L$,

$$\left| \frac{\partial^2}{\partial z^2} \psi_{\pm}(z) \right| \ll \left| \frac{1}{k_L} \frac{\partial}{\partial z} \psi_{\pm}(z) \right|, \quad (5.9)$$

we can neglect second-order spatial derivatives compared to first-order derivatives. Applying this slowly varying envelope approximation, we obtain the coupled-mode equations for the envelope functions

$$\begin{aligned} i \frac{\partial}{\partial t} \psi(z, t) &= \left(-iv_R \sigma_3 \frac{\partial}{\partial z} + \sigma_1 \frac{V_0}{2\hbar} \right) \psi(z, t) \\ &+ \frac{NU_0}{\hbar} \begin{pmatrix} |\psi_+|^2 \psi_+ + 2|\psi_-|^2 \psi_+ \\ |\psi_-|^2 \psi_- + 2|\psi_+|^2 \psi_- \end{pmatrix}. \end{aligned} \quad (5.10)$$

Here, v_R is the recoil velocity defined in Eq. (2.53), and we combined the envelope functions ψ_{\pm} into the vector

$$\boldsymbol{\psi}(z, t) = \begin{pmatrix} \psi_+(z, t) \\ \psi_-(z, t) \end{pmatrix}. \quad (5.11)$$

For compact notation, we also introduced the Pauli matrices² σ_1, σ_3 . The coupling between the two mode functions ψ_{\pm} is mediated by the optical lattice as well as by the nonlinearity, as can be seen in Eq. (5.10). In the derivation of Eq. (5.10) we neglected couplings to modes carrying a momentum other than $\pm\hbar k_L$, since the linear coupling mechanism is off-resonant and the nonlinear mixing is not phase-matched for these momenta.

In the following we present two different solutions of Eq. (5.10) that coincide in an experimentally relevant limit. Whereas the first approach, given in Section 5.2.2, reveals the general structure and the properties of the gap solitons, the method used in Section 5.2.4 gives insight into the physical origin of gap solitons.

5.2.2 Solitary wave solutions

The coupled-mode equations Eq. (5.10) contain the effects of the optical lattice as well as terms describing nonlinear self-phase and cross-phase modulation. In nonlinear optics, Aceves and Wabnitz [137] derived solutions of this set of equations by extending the results of the massive Thirring model of field theory [138], where the self-phase modulation terms are absent. From a strict mathematical point of view, these extended solutions yield solitary waves, since the system is not exactly integrable [139]. Since these solitary waves exhibit most features of a true soliton, including stability in wave packet collisions, we nevertheless refer to them as solitons. Adjusting the solutions from Ref. [137] to our problem, we obtain explicit two-parameter soliton solutions that are characterized by a bounded soliton group velocity $-1 < v_s < 1$, given in units of the recoil velocity v_R , and a shape and phase parameter $0 < \alpha < \pi$:

$$\psi(z, t) = A_0 \left(-\frac{e^{2\theta} + e^{-i\alpha}}{e^{2\theta} + e^{i\alpha}} \right)^{2\gamma_2^2 v_s} e^{i\sigma} \begin{pmatrix} \frac{1}{\beta} \operatorname{sech}(\theta - i\alpha/2) \\ -\beta \operatorname{sech}(\theta + i\alpha/2) \end{pmatrix}. \quad (5.13)$$

Here, we abbreviated

$$\beta = \left(\frac{1 - v_s}{1 + v_s} \right)^{\frac{1}{4}}, \quad (5.14)$$

$$\gamma_1 = \frac{1}{\sqrt{1 - v_s^2}}, \quad \gamma_2 = \frac{1}{\sqrt{3 - v_s^2}}, \quad (5.15)$$

$$\theta = -\frac{V_0 \sin \alpha}{2\hbar v_R \sqrt{1 - v_s^2}} (z - v_s v_R t), \quad (5.16)$$

$$\sigma = -\frac{V_0 \cos \alpha}{2\hbar v_R \sqrt{1 - v_s^2}} (v_s z - v_R t), \quad (5.17)$$

$$A_0 = \frac{\gamma_2}{\gamma_1} \sqrt{\frac{V_0}{2NU_0}} \sin \alpha. \quad (5.18)$$

These solutions account for the full temporal evolution of the system. Since we will be looking for schemes to excite the gap solitons, we focus on the initial conditions by setting $t = 0$. Figure 5.2 illustrates the impact of the parameter α on the shape and phase of the soliton. Higher values of α cause the peak density of the soliton to increase and the width to decrease, as shown in Fig. 5.2(a). Defining the spatial

²The Pauli matrices we use are defined as

$$\sigma_1 = \begin{pmatrix} 0 & 1 \\ 1 & 0 \end{pmatrix}, \quad \sigma_3 = \begin{pmatrix} 1 & 0 \\ 0 & -1 \end{pmatrix}. \quad (5.12)$$

phase difference between the two soliton components as $\Delta\varphi(z) = \arg[\psi_+(z)] - \arg[\psi_-(z)]$, higher values of α lead to a larger spatial phase-step across the soliton, as exhibited in Fig. 5.2(b). For $\alpha \ll 1$ the spatial phase difference is approximately constant with $\Delta\varphi(z) \approx \pi$. In view of a feasible excitation, we restrict our analysis to this case of a constant phase difference. For this regime with $\alpha \ll 1$, the soliton solutions of Eq. (5.13) then simplify to

$$\psi(z, t = 0) \approx \alpha \sqrt{\frac{V_0}{2NU_0}} \frac{\gamma_2}{\gamma_1} \operatorname{sech}\left(\frac{z}{w_s}\right) e^{-ik_s z} \begin{pmatrix} \frac{1}{\beta} \\ -\beta \end{pmatrix}, \quad (5.19)$$

where w_s is the width of the hyperbolic secant-shaped soliton and k_s the soliton wave vector, with

$$w_s = \frac{2\hbar v_R \sqrt{1 - v_s^2}}{\alpha V_0} \quad \text{and} \quad k_s = \frac{v_s V_0}{2\hbar v_R \sqrt{1 - v_s^2}}. \quad (5.20)$$

We obtain an expression for the full wave function ψ_s by substituting Eq. (5.19) into Eq. (5.8),

$$\psi_s(z, t = 0) = \alpha \sqrt{\frac{V_0}{2NU_0}} \frac{\gamma_2}{\gamma_1} \operatorname{sech}\left(\frac{z}{w_s}\right) \left[\frac{1}{\beta} e^{i(k_L - k_s)z} - \beta e^{-i(k_L + k_s)z} \right]. \quad (5.21)$$

Recalling that ψ_s has to be normalized to unity, we determine the number of atoms in the soliton to be

$$\begin{aligned} N &= \frac{2\hbar v_R \alpha \gamma_2^2 \sqrt{1 - v_s^2}}{U_0 \gamma_1^2} \left(\frac{1}{\beta^2} + \beta^2 - \frac{2\pi w_s k_L}{\sinh(\pi w_s k_L)} \right) \\ &\approx \frac{2\hbar v_R \alpha \gamma_2^2 \sqrt{1 - v_s^2}}{U_0 \gamma_1^2} \left(\frac{1}{\beta^2} + \beta^2 \right), \end{aligned} \quad (5.22)$$

where the approximation holds since we require $w_s k_L \gg 1$.

For a stationary soliton with $v_s = 0$ the wave function in Eq. (5.21) simplifies to

$$\psi_s(z, t = 0) = \alpha \sqrt{\frac{2V_0}{3NU_0}} \operatorname{sech}\left(\frac{z}{w_s}\right) \sin(k_L z), \quad (5.23)$$

with width $w_s = 2\hbar v_R / \alpha V_0$ and wave vector $k_s = 0$. We chose the global phase so that $\psi_s(z, t = 0)$ is real. The soliton consists of a hyperbolic secant-shaped envelope that is modulated due to the interference of the two counterpropagating plane wave components. The fringe pattern in the soliton density $|\psi_s|^2$ has the periodicity of the optical lattice with density maxima in the potential minima.

5.2.3 Gap soliton properties

Equation (5.21) shows that gap solitons consist of two counterpropagating components. Whereas in linear systems without an optical lattice these wave packets would travel in opposite directions, the nonlinearity “glues” these packets together to form a non-dispersive unit. However, these soliton solutions impose severe restrictions on the shape, width, number of atoms and spatial phases of the two counterpropagating components. Therefore, we now investigate the most important properties of the soliton solutions, enabling us to connect these to experimentally accessible parameters and to develop excitation schemes.

Note that the solutions in Eq. (5.21) are derived under the assumption $\alpha \ll 1$. It turns out that this approximation is still valid in practice for values $\alpha \leq 0.25$.

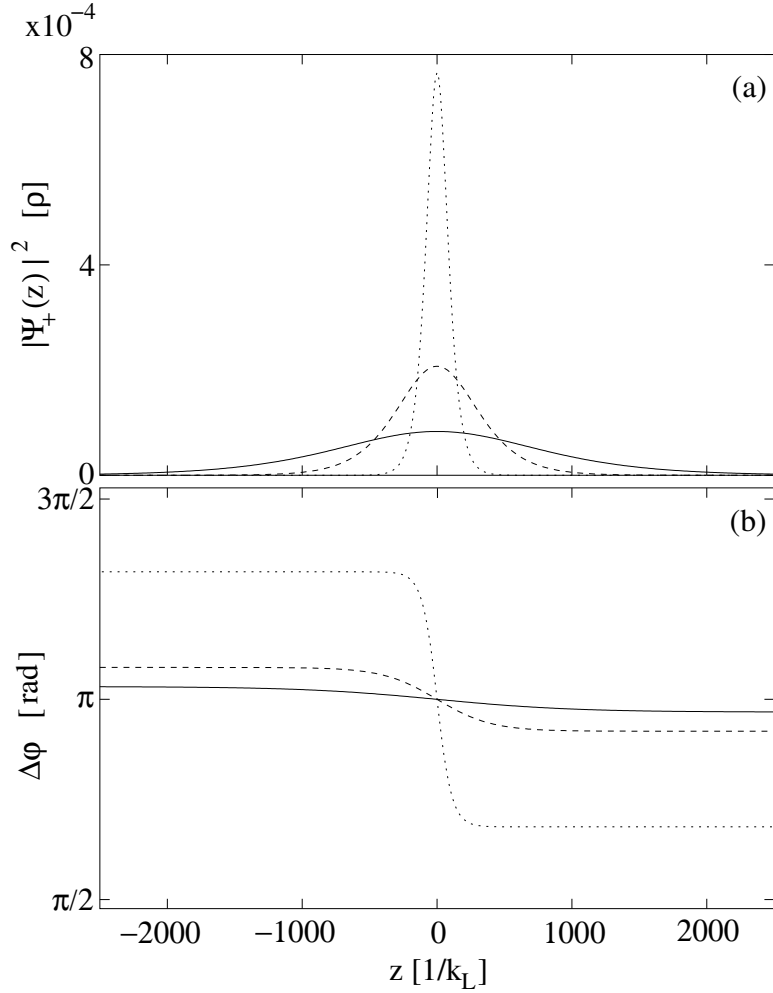


Figure 5.2: One-dimensional soliton solutions at $t = 0$ according to Eqs. (5.13)-(5.18) for $\alpha = 0.1$ (solid), $\alpha = 0.25$ (dashed), and $\alpha = 1.0$ (dotted): (a) soliton density $|\psi_+(z)|^2$ in units of the characteristic density $\rho = 2E_R/NU_0$; (b) phase difference $\Delta\varphi(z) = \arg[\psi_+(z)] - \arg[\psi_-(z)]$. For all plots we chose a stationary soliton consisting of $N = 12204$ atoms with velocity parameter $v_s = 0$, a transverse Gaussian width $w_\perp = 95.7/k_L$ and a lattice depth $V_0 = 0.04E_R$. Note that for $v_s = 0$ we have $|\psi_+(z)|^2 = |\psi_-(z)|^2$.

Momentum modes

Transforming the solution in Eq. (5.21) into momentum space by using the Fourier transform as defined in Eq. (3.12), we obtain

$$\phi_s(k) = \phi_+(k) + \phi_-(k), \quad (5.24)$$

where the mode functions ϕ_{\pm} are centered around $\pm k_L + k_s$ and given by

$$\phi_+(k) = \alpha w_s \frac{1}{\beta} \sqrt{\frac{\pi V_0}{4NU_0}} \frac{\gamma_2}{\gamma_1} \operatorname{sech} \left[\frac{\pi w_s}{2} (k - k_L + k_s) \right], \quad (5.25)$$

$$\phi_-(k) = -\alpha w_s \beta \sqrt{\frac{\pi V_0}{4NU_0}} \frac{\gamma_2}{\gamma_1} \operatorname{sech} \left[\frac{\pi w_s}{2} (k + k_L + k_s) \right]. \quad (5.26)$$

These modes contain important information on the phase and amplitude relations that are needed to create stable solitons. In particular, Eqs. (5.25) and (5.26) show that there is always a spatially homogeneous phase difference of π between the two modes, as described in Section 5.2.2 for the chosen regime $\alpha \ll 1$. For the stationary soliton in Eq. (5.23) it is this phase difference that leads to the sine-shaped modulation of the hyperbolic secant-shaped envelope.

Another important property is the relative mode population. Since in momentum space the distance between the centers of the two modes is $2k_L$ and we require $w_s k_L \gg 1$, the overlap of the two modes is negligible and their relative population is

$$\frac{\int dk |\phi_-(k)|^2}{\int dk |\phi_+(k)|^2} = \beta^4 = \frac{1 - v_s}{1 + v_s}. \quad (5.27)$$

This shows that the relative occupation depends on the soliton velocity v_s . The faster the solitons move to the right (left), the more population is in mode ϕ_+ (ϕ_-), as would be intuitively expected. For $v_s = 0$, the two modes are equally populated.

Width

Equation (5.20) reveals that the soliton width w_s is inversely proportional to the depth of the optical lattice V_0 and the shape parameter α for a chosen velocity parameter v_s ,

$$w_s \propto \frac{1}{V_0 \alpha} v_R v(v_s), \quad (5.28)$$

with $v(v_s) = (1 - v_s^2)^{1/2}$. That means that for fixed parameters α and v_s we can in principle launch solitons with any width by adjusting the lattice depth V_0 to that particular choice. Fig. 5.3(a) illustrates the width as a function of V_0 for two velocities v_s and two values of the parameter α .

Number of atoms

In contrast to the width w_s , the number of atoms in the soliton does not depend on the strength of the optical lattice, as can be seen from Eq. (5.22), but is inversely proportional to the effective nonlinear coefficient U_0 . Using the expression for U_0 for the harmonic transverse potential considered in Section 2.3.1 and the definition of the recoil velocity in Eq. (2.53), we find for a chosen velocity parameter v_s

$$N \propto \frac{\alpha w_s^2 k_L}{a_s} v(v_s), \quad (5.29)$$

with

$$v(v_s) = \sqrt{1 - v_s^2} \left(\frac{1}{\beta^2} + \beta^2 \right) \frac{\gamma_2^2}{\gamma_1^2}. \quad (5.30)$$

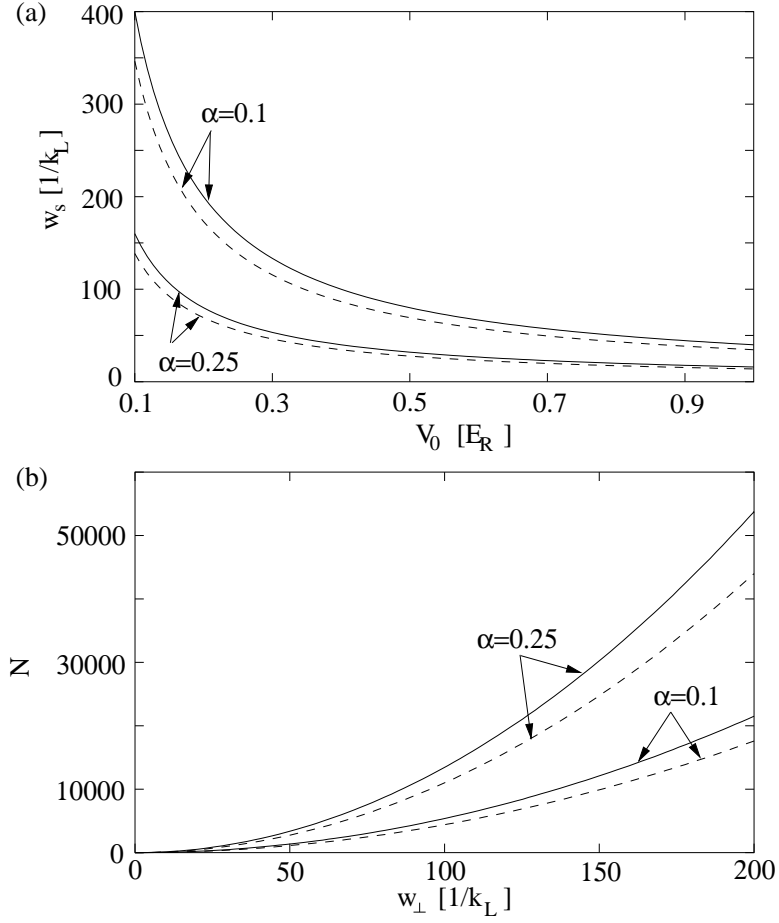


Figure 5.3: Soliton properties for velocities $v_s = 0$ (solid) and $v_s = 0.5$ (dashed) and two choices of parameter α : (a) width w_s as a function of lattice depth V_0 ; (b) number of atoms N as a function of the transverse width w_\perp for typical sodium parameters with $k_L/a_s = 1.3 \times 10^{15}$ (see Section 2.4.3).

For fixed parameters α and v_s and wave vector k_L , the only ways to increase N are by increasing the transverse width w_\perp of the condensate or decreasing the scattering length a_s , e.g. by using Feshbach resonances. Both possibilities lower the effective nonlinear coefficient U_0 . We restrict ourselves here to modifications of the transverse width. In this case the number of atoms depends on the particular species of atoms being considered via the scattering length a_s .

Including the velocity dependence according to Eq. (5.22), Fig. 5.3(b) shows the number of atoms for typical sodium parameters as a function of the transverse width for two velocities v_s and two values of the parameter α . We have to keep in mind that increasing the transverse width will eventually violate the reduction to one dimension. As described in Section 2.3.1, the condensate is assumed to be tightly confined in the transverse direction. In that sense we find ourselves in a situation opposite to the nonlinear optics case: Whereas the difficulty in optics is to achieve high laser intensities to create the required nonlinearity, in the atomic case we actually have to reduce the effective nonlinearity to obtain solitons with a reasonable number of atoms.

In Section 5.3.2 we will show with the help of three-dimensional simulations that there exist parameter regimes that are experimentally accessible.

5.2.4 Multiple scales solutions

In Section 5.2.2 we solved the coupled-mode system from Eq. (5.10) directly by considering the effects of the lattice and the nonlinearity together. We now seek solutions where we neglect the nonlinearity at first and solve the remaining linear system. These linear solutions are then modified by reintroducing the nonlinearity as a small perturbation. This approach is more instructive in the sense that it reveals the physical origin of the gap solitons. We show that in the proper limit the two approaches coincide.

We start by neglecting the nonlinear terms in Eq. (5.10), so we have to solve the linear coupled equations

$$i\frac{\partial}{\partial t}\psi(z, t) = \left(-iv_R\sigma_3\frac{\partial}{\partial z} + \sigma_1\frac{V_0}{2\hbar}\right)\psi(z, t). \quad (5.31)$$

Substituting the plane wave ansatz

$$\psi(z, t) = \begin{pmatrix} A_+ \\ A_- \end{pmatrix} e^{-i(\omega t - kz)} \quad (5.32)$$

into Eq. (5.31) and solving the eigenvalue problem, we find for the energy dispersion

$$\omega^\pm(k) = \pm\sqrt{v_R^2 k^2 + V_0^2/4\hbar^2}, \quad (5.33)$$

with the upper index $+$ ($-$) corresponding to upper (lower) branch. The orthonormal eigenvectors corresponding to ω^\pm are given by

$$\mathbf{A}^\pm(k) = \begin{pmatrix} A_+^\pm(k) \\ A_-^\pm(k) \end{pmatrix} = \frac{1}{\sqrt{2}\sqrt{|\omega^\pm|^2 + v_R\omega^\pm k}} \begin{pmatrix} v_R k + \omega^\pm \\ V_0/2\hbar \end{pmatrix}. \quad (5.34)$$

The solid curves in Fig. 5.4 show the two branches of the dispersion curve (5.33). The lower branch exhibits a negative curvature everywhere and thus a negative effective mass, see Eq. (2.69). Later, we will see that it is this negative effective mass that makes bright soliton solutions possible, despite the repulsive interatomic interaction. Reintroducing the second-order derivatives that were dropped in the slowly varying envelope approximation of Eq. (5.9), we find that the region of

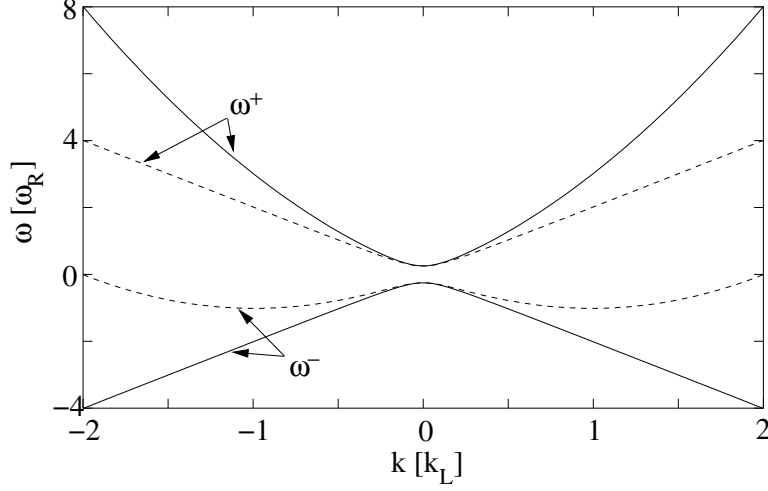


Figure 5.4: Linear energy dispersion for an optical lattice of depth $V_0 = 0.5E_R$, with (solid) and without (dashed) applying the slowly varying envelope approximation.

negative curvature is actually only finite. It can be seen from the dashed curves in Fig. 5.4, that this region is around the center of the Brillouin zone in the lower branch.

Based on these findings, we now reintroduce the nonlinearity as a small perturbation. We consider a wave packet that is placed in the lower branch with a narrow spread of wave vectors around a central value \tilde{k} . We can then write the atomic wavefunction as a product of a slowly varying envelope $\chi(z, t)$ modulated by the solution of the linear system,

$$\psi(z, t) = \chi(z, t) \mathbf{A}^-(\tilde{k}) e^{-i[\omega^-(\tilde{k})t - \tilde{k}z]}. \quad (5.35)$$

Using the *method of multiple scales*, the details of which are shown in Appendix C, leads to a nonlinear equation of motion for the envelope function $\chi(z, t)$,

$$\left[i\hbar \frac{\partial}{\partial t} + i\hbar v \frac{\partial}{\partial z} + \frac{\hbar^2}{2M^*} \frac{\partial^2}{\partial z^2} - g |\chi(z, t)|^2 \right] \chi(z, t) = 0. \quad (5.36)$$

Here, g is the nonlinear coefficient, given by Eq. (C.19) in Appendix C. The group velocity v and the effective mass M^* are derived from the dispersion curve. According to the definitions in Section 2.5.2, they read

$$v = \left. \frac{d\omega^-}{dk} \right|_{\tilde{k}} \quad \text{and} \quad \frac{1}{M^*} = \left. \frac{1}{\hbar} \frac{d^2\omega^-}{dk^2} \right|_{\tilde{k}}. \quad (5.37)$$

As shown in Appendix C, bright soliton solutions of Eq. (5.36) for $g > 0$ only exist if $M^* < 0$. The physical mechanism of the gap solitons can now easily be explained: The repulsive nonlinearity produces a spreading of the wave packet, whereas a negative effective mass in the kinetic energy term causes a contraction of the wave packet. Balancing the spreading and the contraction leads to a soliton solution. In Fig. 5.4 we showed that a region of negative effective mass only exists around the center of the Brillouin zone in the lower branch. Thus, \tilde{k} must be within this region, and it is justified in Eq. (5.35) to modulate the envelope $\chi(z)$ by the

linear solution \mathbf{A}^- corresponding to this lower branch. Also, the envelope solution raises the energy of the linear solution so that the soliton energy lies within the band gap, hence the name *gap soliton*. Note that the effective equation of motion (5.36) yields soliton solutions as in the case of standard atomic solitons described in Section 5.1. However, only the envelope functions are genuine solitons. Modulating the soliton envelopes by the linear eigenfunctions then satisfies the full equation of motion (5.7), but these modulated solutions are no longer true solitons but rather solitary waves.³

In order to connect this approach to the previously derived solutions of Section 5.2.2, we now calculate the envelope $\chi(z)$, taking the case $\tilde{k} = 0$, so that $v = 0$ and $M^* = -V_0/2v_R^2 < 0$. As shown in Appendix C, and by using $\chi(z)$ in Eq. (5.36) we obtain

$$\psi(z, t = 0) = \alpha \sqrt{\frac{V_0}{6NU_0}} \operatorname{sech}\left(\frac{\alpha V_0}{2\hbar v_R} z\right) \begin{pmatrix} 1 \\ -1 \end{pmatrix}, \quad (5.38)$$

with the dimensionless parameter $\alpha \ll 1$. This solution is identical to the one in Eq. (5.19) for $v_s = 0$.

5.3 Numerical propagation studies

After having derived the gap soliton solutions and investigated their properties in the previous sections, we now demonstrate their stability by numerical simulations. The characteristic time scale of solitons is the soliton period t_s , defined as the time it takes for the dynamical soliton phase σ , see Eqs. (5.13) and (5.17), to go through a cycle of 2π . Requiring $\sigma t_s = 2\pi$ leads to an expression for the soliton period,

$$t_s = \frac{4\pi\hbar\sqrt{1-v_s^2}}{V_0}. \quad (5.39)$$

A soliton is considered stable if the initial wave packet does not disperse over the course of several soliton periods. In the following we show the evolution of stationary and moving solitons in one and three dimensions.

5.3.1 Propagation in one dimension

Figure 5.5 shows the evolution of solitons that were initially prepared according to Eq. (5.21). In Fig. 5.5(a), the stable propagation of a stationary soliton over ten soliton periods is demonstrated, whereas Fig. 5.5(b) illustrates a stable moving soliton with a velocity of $v_s = 0.5$ over eight soliton periods. In both cases, the initial wave packet does not exhibit spatial dispersion.

Both solitons exhibit fringes in the density due to the interference of the two counterpropagating components. Note, however, that the actual spatial period is on the order of $1/k_L$ and cannot be resolved in the graphs. The fringes seen in both graphs are due to aliasing effects and are not physical.

5.3.2 Propagation in three dimensions

Cylindrical coordinates

Until now we restricted ourselves to situations where a description by the one-dimensional GPE from Eq. (2.32) is sufficient. However, we need to investigate the stability of the gap solitons in three-dimensional geometries. This is necessary since in any experimental setting, the wave function will have a finite transversal width.

³As mentioned earlier, since these solitary waves exhibit almost all features of true solitons, we nevertheless refer to them as solitons.

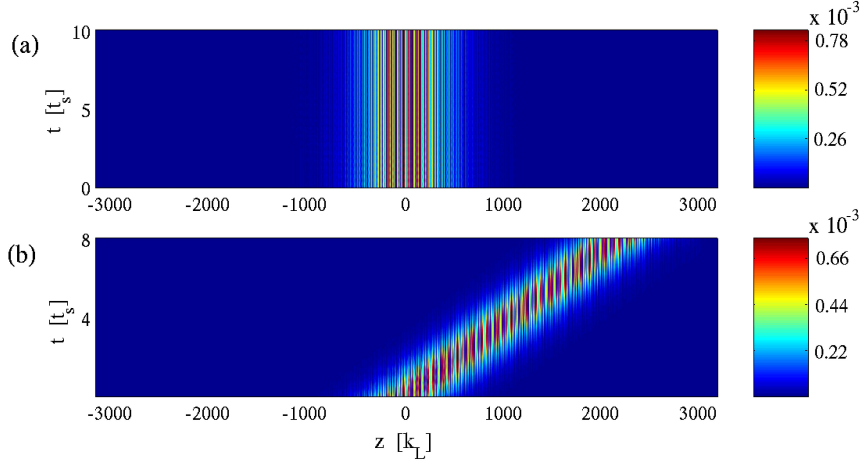


Figure 5.5: Temporal evolution of one-dimensional solitons, the color coding shows the density $|\psi_s(z, t)|^2$ in units of the characteristic density $\rho = 2E_R/NU_0$: (a) stationary soliton with velocity $v_s = 0$, width $w_s = 400/k_L$ and $N = 12204$ atoms; (b) moving soliton with $v_s = 0.5$, $w_s = 346.4/k_L$ and $N = 9985$. For both plots we chose $\alpha = 0.25$ and used a transverse Gaussian width $w_\perp = 95.7/k_L$ and a lattice depth $V_0 = 0.04E_R$.

We need to choose this width carefully in order not to cause transverse excitations. Additionally, we know from Section 5.2.3 that this width also determines the number of atoms in the soliton.

In order to model realistic geometries, we assume the condensate to be confined in the transverse direction by a radially symmetric trapping potential. It is then advantageous to transform the GPE to cylindrical coordinates

$$\begin{aligned} i\hbar \frac{\partial}{\partial t} \psi(r, z, \varphi, t) &= -\frac{\hbar^2}{2M} \left(\frac{\partial^2}{\partial r^2} + \frac{1}{r} \frac{\partial}{\partial r} + \frac{1}{r^2} \frac{\partial^2}{\partial \varphi^2} + \frac{\partial^2}{\partial z^2} \right) \psi(r, z, \varphi, t) \\ &+ \left[V(r, z, t) + NU |\psi(r, z, \varphi, t)|^2 \right] \psi(r, z, \varphi, t). \end{aligned} \quad (5.40)$$

We do not consider situations where the condensate carries angular momentum, as would be the case for vortices. It is thus justified to drop the dependence on φ . The GPE for the cylindrically symmetric wave function then reduces to

$$\begin{aligned} i\hbar \frac{\partial}{\partial t} \psi(r, z, t) &= -\frac{\hbar^2}{2M} \left(\frac{\partial^2}{\partial r^2} + \frac{1}{r} \frac{\partial}{\partial r} + \frac{\partial^2}{\partial z^2} \right) \psi(r, z, t) \\ &+ \left[V(r, z, t) + NU |\psi(r, z, t)|^2 \right] \psi(r, z, t). \end{aligned} \quad (5.41)$$

We assume the potential $V(r, z, t)$ to be time-independent, consisting of a stationary harmonic trapping potential in the radial direction and an optical lattice potential along the z -axis:

$$V(r, z) = \frac{1}{2} M \omega_\perp^2 r^2 + V_0 \cos(2k_L z), \quad (5.42)$$

where ω_\perp is the transverse trapping frequency.

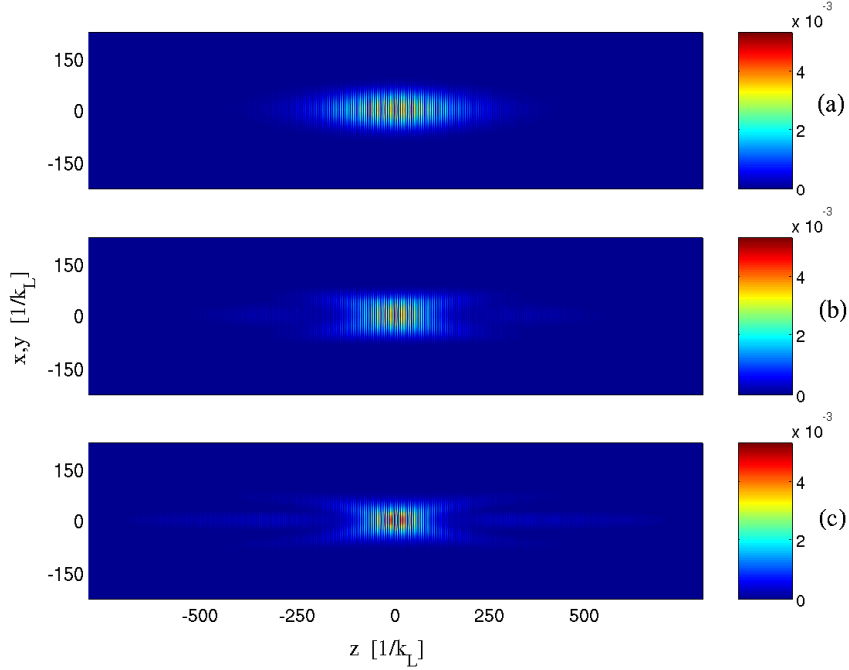


Figure 5.6: Three-dimensional stationary soliton $|\psi(r, z)|^2$ according to Eq. (5.43) at different times: (a) $t = 0$; (b) $t = 10t_s$; (c) $t = 20t_s$. The color coding shows the density in units of $\rho = 2E_R/NU$. The soliton with velocity $v_s = 0$, longitudinal width $w_s = 160.0/k_L$ and transverse width $w_\perp = 95.7/k_L$ contains $N = 12204$ atoms. The lattice depth is $V_0 = 0.1E_R$, the transverse trapping frequency $\omega_\perp = 0.00158\omega_R$ and $\alpha = 0.25$.

Results

We use a finite difference method as described in Appendix A to solve Eq. (5.41) with the potential (5.42). As an initial wave packet we use the one-dimensional soliton solution $\psi_s(z)$ in Eq. (5.21) along the z -axis and a Gaussian density distribution in the radial direction,

$$\psi(r, z) = \psi_s(z) \frac{2}{\sqrt{\pi}w_\perp} e^{-2r^2/w_\perp^2}, \quad (5.43)$$

where w_\perp is the transverse Gaussian width. Figure 5.6 shows⁴ the stable evolution of a stationary soliton over 20 soliton periods. Obviously, the wave packet does not disperse over the course of the simulation. In Fig. 5.7 we illustrate details of the soliton dynamics by slicing the wave packet along the z -axis at $r = 0$. Since the soliton solution $\psi_s(z)$ in Eq. (5.21) is strictly valid only in a true one-dimensional geometry, the wave packet undergoes some reshaping due to transverse effects. By contracting and shedding off atoms, as indicated by the lobes to both sides of the peak density in Figs. 5.7(a) and (b), the wave packet rearranges itself so that the remaining atoms form a stable soliton. In Fig. 5.8 we demonstrate the stable

⁴As in the one-dimensional case, the visible fringes are not physical since the actual fringe spacing cannot be resolved.

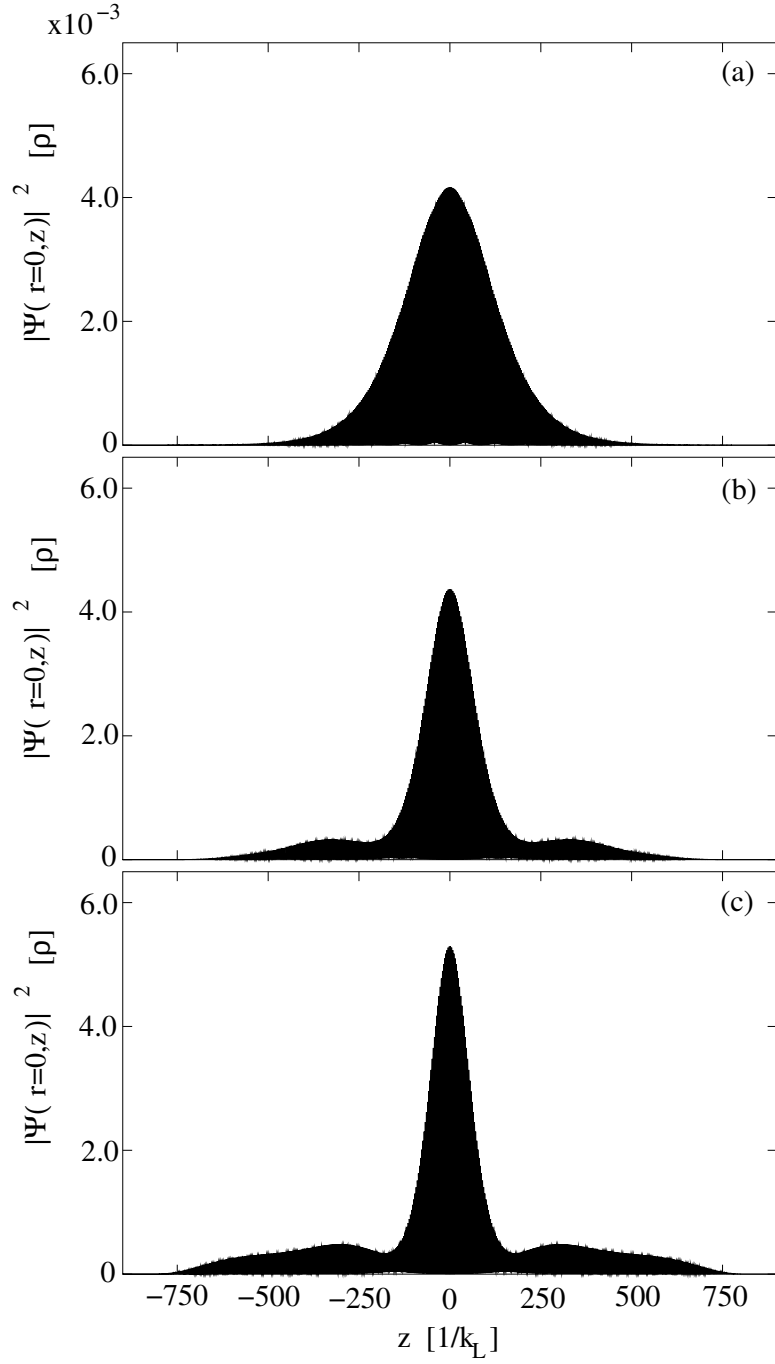


Figure 5.7: Stationary soliton from Fig. 5.6, slices at $r = 0$ at different times: (a) $t = 0$; (b) $t = 10t_s$; (c) $t = 20t_s$. The soliton density $|\psi(r = 0, z)|^2$ is given in units of $\rho = 2E_R/NU$.

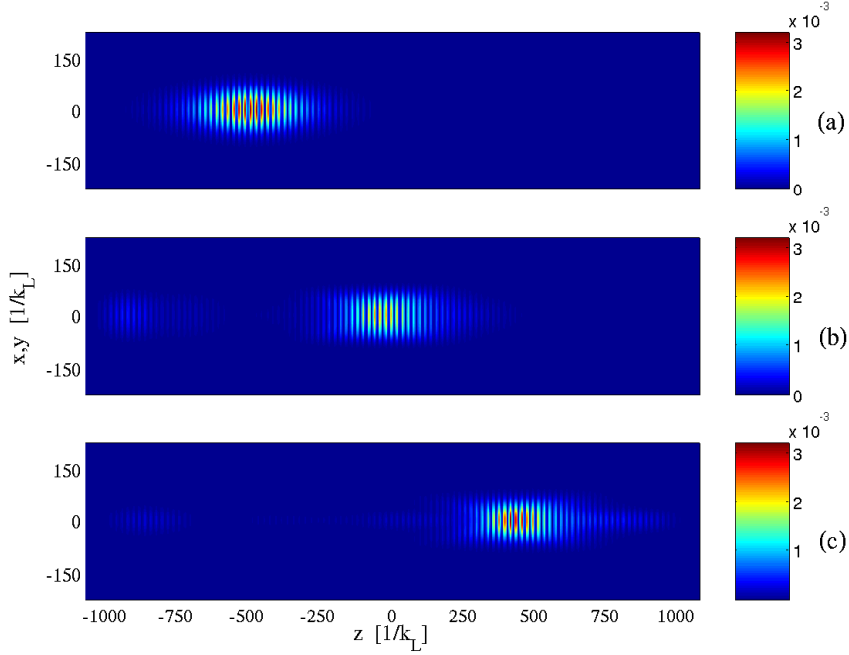


Figure 5.8: Three-dimensional moving soliton $|\psi(r, z)|^2$ according to Eq. (5.43) at different times: (a) $t = 0$; (b) $t = 8.17t_s$; (c) $t = 16.33t_s$. The color coding shows the density in units of $\rho = 2E_R/NU$. The soliton with velocity $v_s = 0.5$, longitudinal width $w_s = 160.0/k_L$ and transverse width $w_\perp = 105.8/k_L$ contains $N = 12204$ atoms. The lattice depth is $V_0 = 0.087E_R$, the transverse trapping frequency $\omega_\perp = 0.00129\omega_R$ and $\alpha = 0.25$.

evolution of a moving soliton over 16.33 soliton periods.⁵ Again, we do not observe any significant dispersion along the z -axis. In a recent publication, Hilligsøe *et al.* [140] showed numerically that gap solitons are stable only in a truly one-dimensional situation, whereas in two and three dimensions, resonant transverse excitations lead to dynamical instabilities. They calculated the time for the decay in three dimensions to be $1/(0.133\omega_\perp)$, corresponding to $38.0t_s$ for the parameters of Fig. 5.6 and $46.6t_s$ for Fig. 5.8. Since the characteristic time scale of the solitons t_s is much smaller than the decay time, stable propagation over reasonably long times is possible for realistic physical parameters, as numerically verified in Figs. 5.6 and 5.8.

For completeness, we demonstrate numerically the importance of the correct relative phase between the two counterpropagating components of the gap soliton. To do so, we artificially create a phase difference of 2π between the two momentum modes of a stationary soliton. This corresponds to a $\cos(k_L z)$ modulation of the hyperbolic secant-shaped envelope in Eq. (5.23). The density maxima of the wave function and the lattice potential now coincide and this situation does not correspond to a stable soliton. Figure 5.9 shows the propagation of this wave packet, displaying strong dispersion along the z -axis. All other parameters are chosen to be the same as in Fig. 5.6.

⁵We propagate the soliton over only 16.33 soliton periods due to computational restrictions, since the wave packet eventually reaches the numerical domain boundary.

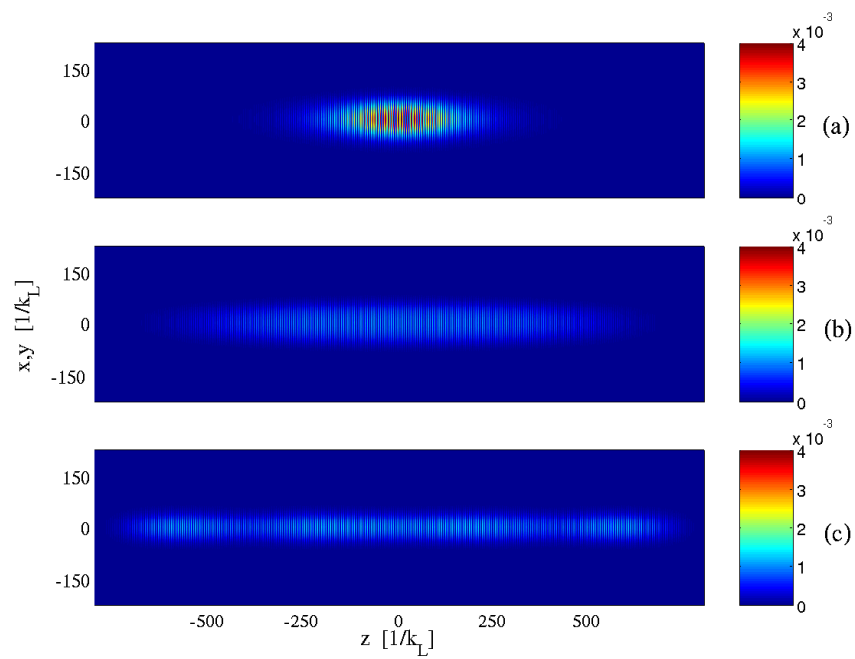


Figure 5.9: Atomic wave packet with the same parameters as in Fig. 5.6 but incorrect relative phase between the counterpropagating components. The wave packet is shown at different times: (a) $t = 0$; (b) $t = 10t_s$; (c) $t = 20t_s$. The color coding shows the density in units of $\rho = 2E_R/NU$.

5.4 Excitation of gap solitons

Although optical and atomic solitons are governed by similar equations of motion and therefore have equivalent mathematical structures, their excitation schemes differ fundamentally. For the generation of optical solitons it is often sufficient to solely couple light with a frequency and power fulfilling the soliton conditions into optical fibers [113]. However, although atomic solitons, such as the dark and bright solitons of Section 5.1, were already derived shortly after the first demonstration of Bose-Einstein condensates [121], their experimental demonstration was delayed, because elaborate excitation schemes were required. The successful use of optical phase imprinting [19, 20] and Feshbach resonances [70, 71] shows that these schemes are completely different from the excitation of optical solitons. Also in the case of atomic gap solitons, the optical counterpart cannot guide us and we have to find new ways of excitation. In the following we discuss two experimentally feasible schemes to generate atomic gap solitons. In particular, we demonstrate the excitation of the stationary soliton shown in Fig. 5.5(a). For simplicity, we restrict the numerical simulations to this one-dimensional case.

In Section 5.2.3 we showed that once the velocity of the soliton is chosen, we have to populate two momentum modes according to that specific choice and create a phase difference of π between the two modes. For the stationary soliton that we wish to excite we need equal populations of the two modes centered around $\pm k_L$.

In both excitation schemes we start with a condensate initially at rest and the trapping potential switched off. We assume the initial condensate wave function to be

$$\psi_0(z) = \sqrt{2}\alpha \sqrt{\frac{V_0}{6NU_0}} \operatorname{sech}\left(\frac{z}{w_s}\right). \quad (5.44)$$

Although we assume a hyperbolic secant-shaped wave function this is not a strong restriction for experimental setups. Gap solitons are known to be fairly insensitive to the exact shape as long as the width of the wave packet matches the initial conditions [119].

5.4.1 Bragg pulse excitation

The first excitation scheme uses resonant Bragg pulses to transfer the correct population to the momentum modes. Since we have to couple from a condensate initially at rest to modes carrying momenta $\pm \hbar k_L$, we need a moving lattice of the form

$$V(z, t) = V_0 \cos(2\bar{k}z + \delta t) \quad \text{with} \quad \bar{k} = k_L/2. \quad (5.45)$$

For resonant Bragg scattering from the initial mode with zero momentum to modes with momenta $\pm \hbar k_L$ we need $\delta = \mp \omega_R$ [100]. With a first pulse of duration t_1 we transfer half of the population from the initial mode to the mode carrying momentum $\hbar k_L$. A second pulse of duration t_2 is then applied to transfer the remaining population from the initial mode to the mode with momentum $-\hbar k_L$. By adjusting the pulse durations we are able to establish a homogeneous phase of π between the modes with $\pm \hbar k_L$. Starting with ψ_0 given by Eq. (5.44), the excitation scheme reads

$$\begin{aligned} \psi_0 & \xrightarrow{\text{1st Bragg pulse}} \frac{1}{\sqrt{2}} \psi_0 (1 - i e^{i k_L z}) \\ & \xrightarrow{\text{2nd Bragg pulse}} \frac{i}{\sqrt{2}} \psi_0 (e^{-i k_L z} - e^{i k_L z}). \end{aligned}$$

The final state is identical to the soliton solution $\psi_s(z)$ in Eq. (5.23). We then replace the moving lattice in Eq. (5.45) by a stationary lattice

$$V(z) = V_0 \cos(2k_L z). \quad (5.46)$$

This is the lattice that is needed for a stable propagation of the excited soliton.

Figure 5.10 shows the numerical simulation of the excitation process. In Fig. 5.10(a) the wave packet after the first Bragg pulse is illustrated. The right inset shows that the initial mode and the mode with momentum $\hbar k_L$ are equally populated. This leads to an interference pattern in the density. After the second Bragg pulse, we see in Fig. 5.10(b) that now both modes with momentum $\pm \hbar k_L$ are equally populated. The vanishing density at the origin $z = 0$ indicates a sine-shaped modulation, corresponding to the desired relative phase of π . Figure 5.10(c) then shows the generated wave packet after a propagation over ten soliton periods. Although there is an onset of a shoulder visible in Fig. 5.10(c), suggesting that a wave packet is separating from the soliton, further numerical investigations show that this is not the case.⁶ The population difference between the two momentum modes causes the soliton to move very slowly. However, this effect is negligible over the chosen timescale of several soliton periods. Apparently, our proposed scheme results in the excitation of a stable and (almost) stationary soliton that does not disperse.

5.4.2 Genetic algorithm excitation

The excitation scheme of the previous section has the disadvantage that two optical lattices are needed, one for resonant Bragg scattering and one for the excited soliton to “live in”. We circumvent this in a second scheme by using a magnetic field in combination with an optimized lattice motion as described in Chapter 4.

In a first step we accelerate the condensate initially at rest to a state with momentum $-\hbar k_L$. This can be achieved by applying a magnetic field with a spatial gradient B' . The potential for this interaction can be written as

$$V(z) = m_F g_F \mu_B B' z, \quad (5.47)$$

with $\mu_B = 9.274 \times 10^{-28}$ J/G the Bohr magneton and g_F the g -factor. In general, a condensate consisting of sodium atoms is trapped in a hyperfine state with quantum numbers $F = 1$ and $m_F = -1$. For this configuration we have $g_F \approx -0.5$. For a given magnetic field gradient B' the field has to be switched on for a time t_1 determined by

$$-m_F g_F \mu_B B' t_1 = -\hbar k_L, \quad (5.48)$$

in order to place the condensate in a mode with momentum $-\hbar k_L$.

We now recall the results from Chapter 4, where we demonstrated the creation of a prescribed population and phase difference in momentum modes by optimizing the lattice motion with help of genetic algorithms. In this excitation scheme we have to transfer half of the population from the mode with momentum $-\hbar k_L$ to the mode with $\hbar k_L$. At the same time we need to create a phase difference of π between these two modes. Using a lattice of the form

$$V(z, t) = V_0 \cos [2k_L z - \delta(t)t], \quad (5.49)$$

we have to find the time-dependent detuning $\delta(t)$ that creates the prescribed momentum state during a time t_2 . Schematically, this scheme reads

$$\begin{aligned} \psi_0 &\xrightarrow{B'} \psi_0 e^{-ik_L z} \\ &\xrightarrow{\delta(t)} \frac{1}{\sqrt{2}} \psi_0 (e^{ik_L z} - e^{-ik_L z}). \end{aligned}$$

⁶We also propagated the excited gap soliton over 30 soliton periods and observed a negligible loss of only 3% of the initial number of atoms (not shown in a figure).

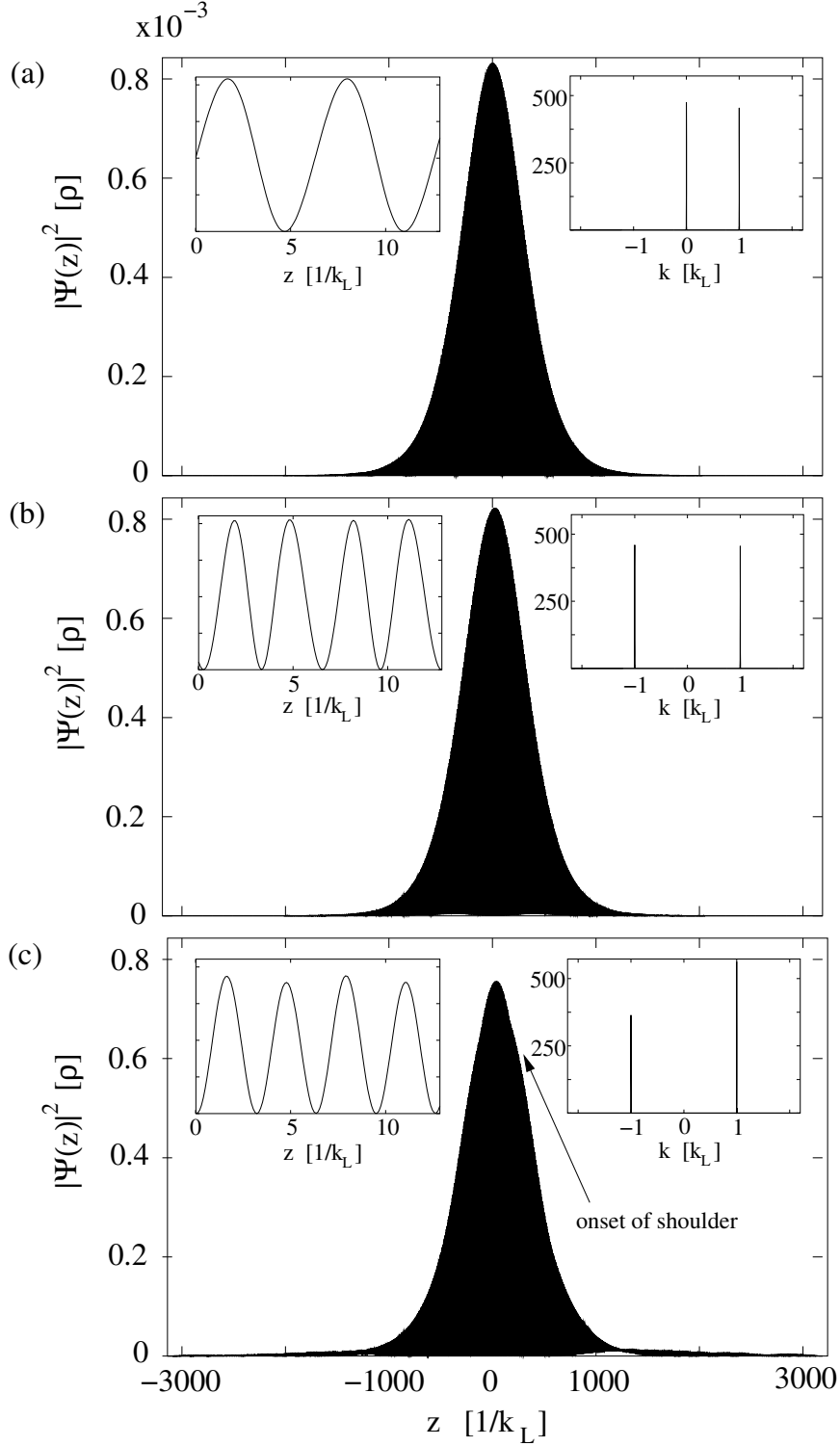


Figure 5.10: Excitation and propagation of a stationary soliton with $w_s = 400/k_L$, $w_\perp = 95.7/k_L$, $N = 12204$, $\alpha = 0.25$ and $\rho = 2E_R/NU_0$. The left insets show a magnification of $|\psi(z)|^2$ in the same units as the large graphs, the right insets illustrate the momentum distribution $|\phi(k)|^2$ in units of $1/\rho$. (a) After the Bragg pulse at $t_1 = 2\pi/\omega_R$ with lattice $V_0 \cos(k_L z - \omega_R t)$ and $V_0 = E_R$. (b) After the Bragg pulse at $t_2 = t_1 + 12\pi/\omega_R$ with lattice $V_0 \cos(k_L z + \omega_R t)$ and $V_0 = E_R$. (c) After propagation at $t_3 = t_2 + 10t_s$, with lattice $V_0 \cos(2k_L z)$ and $V_0 = 0.04E_R$.

After the optimized lattice motion, the final state of the condensate meets the initial conditions for a stationary soliton. By setting $\delta(t) = 0$ for $t > t_1 + t_2$ we already have the stationary lattice needed for a stable propagation of the excited soliton.

Figure 5.11 shows the numerical results of the excitation process. After applying the magnetic field gradient the condensate is completely in the state of momentum $-\hbar k_L$, as illustrated in Fig. 5.11(a). There are clearly no interference fringes in that case. Figure 5.11(b) shows the wave function after the lattice evolution according to an optimized $\delta(t)$. The condensate is almost in an equal superposition of modes with momentum $\pm\hbar k_L$. It is not exactly an equal superposition since the optimization procedure was stopped when there was more than 47% population in each of these modes. The sine-like oscillations in the density verify that there is a relative phase difference of π between the modes. Figure 5.11(c) then shows the wave packet after a propagation over ten soliton periods. Due to the imperfect excitation, i.e. slightly unequal mode populations, the wave packet rearranged its shape over the course of the propagation. Nevertheless, the population difference is much smaller than in the case of Bragg pulse excitation shown in Fig. 5.10(c). The wave packet behaves like a soliton since the dispersive effects are very small and thus the genetic algorithm optimization enables a stable gap soliton excitation.

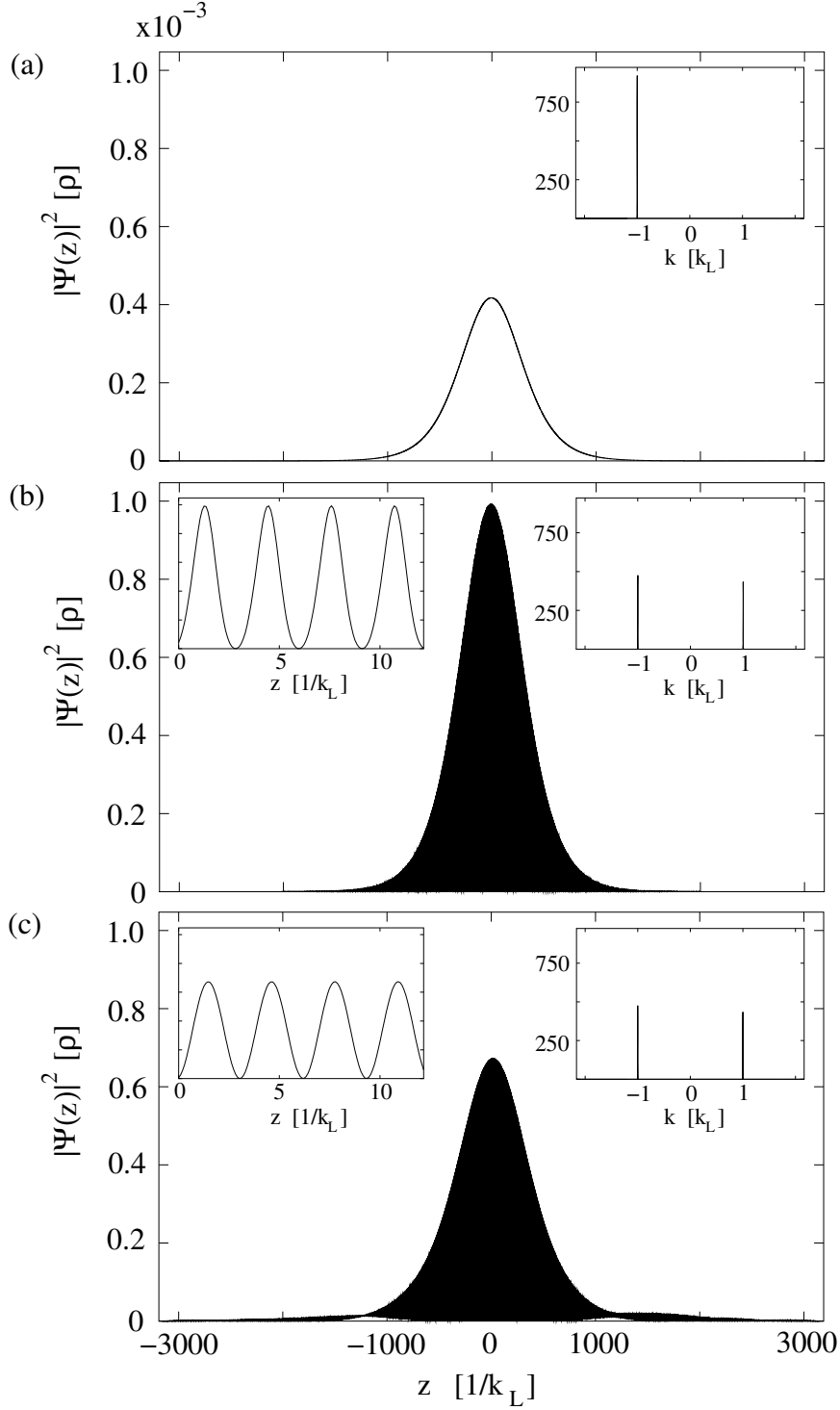


Figure 5.11: Excitation and propagation of a stationary soliton with $w_s = 400/k_L$, $w_\perp = 95.7/k_L$, $N = 12204$, $\alpha = 0.25$ and $\rho = 2E_R/NU_0$. The left insets show a magnification of $|\psi(z)|^2$ in the same units as the large graphs, the right insets illustrate the momentum distribution $|\phi(k)|^2$ in units of $1/\rho$. (a) After magnetic field pulse at $t_1 = 5.6/\omega_R$. (b) After optimized lattice motion at $t_2 = t_1 + \pi/2\omega_R$ with lattice $V_0 \cos[2k_L z - \delta(t)t]$ and $V_0 = 2E_R$. (c) After propagation at $t_3 = t_2 + 10t_s$ with lattice $V_0 \cos(2k_L z)$ and $V_0 = 0.04E_R$.

Chapter 6

Outlook: Fermions

This chapter serves as an outlook on one of the latest developments in the field of atom optics: degenerate systems of dilute Fermi gases. These systems have recently been experimentally demonstrated [141, 142, 143, 144]. Unlike Bose-Einstein condensates, these systems are not amenable to a mean-field description, a consequence of the intrinsically multimode character of the system due to Pauli exclusion principle. Fermi systems promise the extension of nonlinear atom optics to a regime without counterpart in traditional nonlinear optics.

After a brief review of recent achievements in theoretical and experimental aspects of degenerate Fermi gases in Section 6.1, we present a simple model of a fermionic atomic coupler in Section 6.2. This model helps to gain an understanding how fermionic matter waves can be manipulated by interaction with light, which is a cornerstone in the quantum control of bosonic atoms as well. In contrast to the well-known two-mode couplers that accurately describe many physical situations, such as optical waveguide switches or population transfer in two-level atoms, the fermionic coupler will be an example of a nonlinear multimode coupler. We discuss the specific situation where transitions between two internal states of a quantum-degenerate Fermi system at zero temperature are induced by Raman coupling. We assume both states to be harmonically trapped with slightly different trap frequencies. Investigating the dynamics of the system serves the two-fold goal to illustrate some of the differences to the bosonic case, as well as the role of collisions in the fermionic case. Neglecting collisions in Section 6.3, we find that the optical coupling results in a collapse and revival behavior of the population difference between the two traps, caused by the difference in trap frequencies. However, as then shown in Section 6.4, two-body collisions lead to an additional nonlinear phase shift that inhibits the collapse of the population difference.

6.1 Degenerate Fermi gases

6.1.1 Cooling of fermions

As in the case for bosons, dilute fermionic gases approach quantum degeneracy when the phase space density reaches unity. Whereas bosons condense in the lowest single-particle state, fermions tend to a state with a filled Fermi sea. In order to achieve the ultracold temperatures needed for quantum degenerate Fermi gases, one first applies common laser cooling techniques that work irrespectively of the atom statistics. However, laser cooling alone is not sufficient, and fermions cannot be evaporatively cooled the way bosons are because of their fermionic statistics: Due to the requirement of antisymmetry, identical fermions, i.e. fermions of the same species and in the same internal state, are not subject to s -wave scattering, and the

effects of p -wave scattering are negligibly small. These scattering events, however, are necessary to rethermalize the remaining atoms after high energy fermions have been removed from the trap. This difficulty can be overcome by using a mixture of two different types of atoms. Successful experiments with ^{40}K used two different internal states and both states were evaporatively cooled. The interspecies s -wave scattering then enabled the rethermalization [141, 142]. In another experiment, ^6Li fermions were cooled together with their bosonic isotope ^7Li [143, 144, 145]. The fermions were cooled by collisions with the bosons that were evaporated, a process referred to as *sympathetic cooling*. Besides this influence of the atom statistics on the cooling process, an additional problem is the increasing degree of degeneracy during the cooling. Pauli blocking reduces the number of available final states and as a result, even two-component mixtures cannot easily be cooled efficiently since fewer collisions scatter into the few empty states [142, 146]. However, sophisticated improvements of the cooling techniques overcame these problems so that several groups have now achieved quantum degenerate Fermi gases with temperatures as low as one tenth of the Fermi temperature T_F [147, 148] with up to 7×10^7 atoms [149, 150]. These samples of degenerate fermions are comparable in size to the largest alkali Bose-Einstein condensates.

6.1.2 The BCS-BEC crossover

Currently, research is being conducted on the control of interatomic interactions by the use of Feshbach resonances. These resonances occur when the relative energy of a colliding pair of atoms is nearly degenerate with a quasi-bound molecular state. First observations in samples of fermions have been made in Ref. [151], where p -wave scattering between fermions in the same hyperfine state were enhanced. In another experiment, measurements of positive and negative s -wave scattering lengths in a Fermi gas have been reported [152]. Controlling the scattering length opens up the possibility of experimentally tuning the fermionic system between a Bardeen-Cooper-Schrieffer (BCS)-type superfluid¹ and a Bose-Einstein condensate. In the BCS limit, the superfluidity is due to a condensation of delocalized *Cooper pairs*, where two fermions are correlated in momentum space in the presence of attractive interatomic interactions. In the case of repulsive interactions, pairs of fermions form weakly bound bosonic molecules that can then condense into a Bose-Einstein condensate (BEC). Whereas in the BCS-type superfluid the Fermi statistics plays an essential role, no fermionic degrees of freedom remain in the case of a molecular BEC since the fermions are bound as bosonic molecules. Tuning the interatomic interaction from attractive to repulsive one can continuously probe the BCS-BEC crossover. Close to the Feshbach resonance, where the scattering length changes its sign, one expects to see resonance superfluidity [152, 159, 160]. Although a pure BCS-type superfluid has not been reported yet, experimental formation of remarkably stable bosonic molecules² from a Fermi gas [150, 162] led to the successful demonstration of molecular Bose-Einstein condensates [163, 164, 165]. Just recently, even the resonance condensation of fermionic atom pairs close to the Feshbach resonance has been reported [147, 166]. The possibility of exploring the BCS-BEC crossover regime in dilute Fermi gases follows many years of theoretical studies and might lead to new insights into the world of interacting fermions, that has not been possible with conventional Fermi systems such as e.g. electrons in

¹The theory of BCS-type superfluidity respectively superconductivity has originally been developed for electrons in metals by Bardeen, Cooper and Schrieffer [153]. Theoretical investigations on the formation of this state in dilute atomic vapors can be found in Refs. [154, 155, 156, 157, 158, 159, 160].

²Dimers of fermions exhibit much longer lifetimes than dimers of bosons due to the fermionic suppression of vibrational quenching in molecule collisions [161].

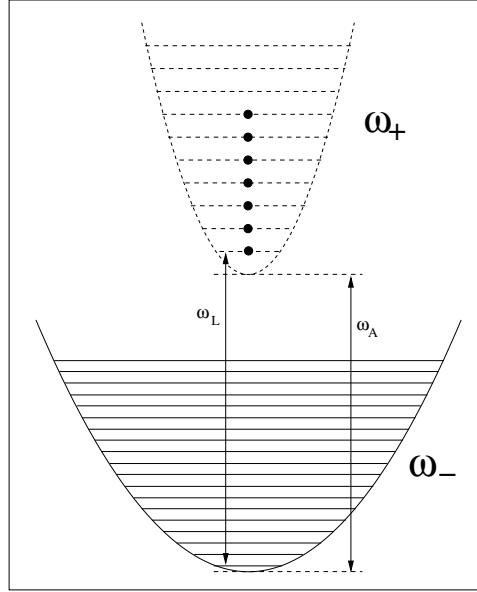


Figure 6.1: Two-component Fermi gas in a harmonic trap. The trapping frequencies ω_+ and ω_- correspond to the two internal states, which are coupled via a spin-flip transition at frequency ω_L resonant with the frequency difference of the trap ground states.

metals.

6.2 The fermionic Raman coupler

6.2.1 The model system

We consider a two-component quantum-degenerate atomic system trapped in a one-dimensional, harmonic potential with each component corresponding, e.g., to one internal hyperfine spin state. In general, the coupling of the atoms to the trapping field is different for the two (spin) components $|+\rangle$ and $|-\rangle$, so that they see trapping potentials of different frequencies ω_+ and ω_- . The two internal states are coupled by a Raman-type interaction of frequency ω_L equal to the spin-flip transition frequency of the atoms in the ground state of the two trapping potentials. This model, which is summarized on the diagram of Fig. 6.1, is described by the second-quantized Hamiltonian

$$\begin{aligned} \hat{\mathcal{H}} &= \int dx \hat{\Psi}_+^\dagger(x) H_+ \hat{\Psi}_+(x) + \int dx \hat{\Psi}_-^\dagger(x) H_- \hat{\Psi}_-(x) \\ &+ \hbar g \int dx \left[e^{-i\omega_L t} \hat{\Psi}_+^\dagger(x) \hat{\Psi}_-(x) + \text{h.c.} \right], \end{aligned} \quad (6.1)$$

where $\hbar g$ is the Raman coupling strength. The first-quantized Hamiltonian describing the trapping potentials associated with the internal states $|+\rangle$ and $|-\rangle$ is

$$H_\pm = -\frac{\hbar^2}{2m} \frac{\partial^2}{\partial x^2} + \frac{1}{2} m \omega_\pm^2 x^2 + E_\pm, \quad (6.2)$$

with E_{\pm} being the energy of the internal state $|\pm\rangle$. The Raman resonance condition is therefore, with $\omega_A = E_+ - E_-$,

$$\omega_L = \omega_A + (\omega_+ - \omega_-)/2. \quad (6.3)$$

We remark that this resonance condition effects only the coupling between the two trap ground states: the coupling between all other levels is off-resonant for $\omega_+ \neq \omega_-$. Hence, introducing a small detuning even for the ground states does not significantly alter the dynamics of the system.

6.2.2 Equations of motion

The atomic field operators corresponding to the two traps obey the fermionic, respectively bosonic (anti)commutation relations

$$\begin{aligned} [\hat{\Psi}_i(x), \hat{\Psi}_j^\dagger(x')]_{\pm} &= \delta_{ij}\delta(x-x'), \\ [\hat{\Psi}_i(x), \hat{\Psi}_j(x')]_{\pm} &= 0, \\ [\hat{\Psi}_i^\dagger(x), \hat{\Psi}_j^\dagger(x')]_{\pm} &= 0, \end{aligned} \quad (6.4)$$

where $i, j = \{+, -\}$.

For the harmonic potentials at hand, the Heisenberg equations of motion for the atomic field operators take the same form, independently of whether the atoms are bosonic or fermionic. It is convenient to expand them in terms of eigenstates $\{u_n(x)\}$ of one of the trap Hamiltonians H_{\pm} , say, H_+ for concreteness, as

$$\begin{aligned} \hat{\Psi}_+(x, t) &= \sum_n u_n(x) \hat{a}_n(t), \\ \hat{\Psi}_-(x, t) &= \sum_n u_n(x) \hat{b}_n(t), \end{aligned} \quad (6.5)$$

where the \hat{a}_n and \hat{b}_n satisfy either fermionic or bosonic commutation relations. In both cases, this expansion readily yields the Heisenberg equations of motion

$$\begin{aligned} i \frac{d\hat{a}_n}{d\tau} &= A_n \hat{a}_n + \tilde{g} \hat{b}_n, \\ i \frac{d\hat{b}_n}{d\tau} &= B_n \hat{b}_n + C_n \hat{b}_{n+2} + D_n \hat{b}_{n-2} + \tilde{g} \hat{a}_n, \end{aligned} \quad (6.6)$$

where we have introduced the coefficients

$$\begin{aligned} A_n &= \frac{1}{2}(\beta - 1) + n, \\ B_n &= \frac{1}{4}(\beta^2 - 1)(2n + 1) + n, \\ C_n &= \frac{1}{4}(\beta^2 - 1)\sqrt{(n+2)(n+1)}, \\ D_n &= \frac{1}{4}(\beta^2 - 1)\sqrt{n(n-1)}, \end{aligned} \quad (6.7)$$

and the ratio

$$\beta = \omega_+/\omega_- \quad (6.8)$$

of the trap frequencies. The dimensionless time τ is scaled to ω_+ , $\tau = \omega_+ t$, and so is the dimensionless coupling strength $\tilde{g} = g/\omega_+$.

We emphasize that while the operator \hat{a}_n describes the annihilation of atoms in level n of the upper trap, a similar interpretation of the \hat{b}_n 's is not possible, since they result from the expansion of the field operator of atoms in the internal state $|-\rangle$ on the basis of the “+”-trap. Denoting the eigenstates of the single-atom Hamiltonian of the lower trap as $\{v_n(x)\}$, the “true” annihilation operators \hat{c}_n associated with the trapped atoms in the $|-\rangle$ internal state are related to the \hat{b}_n 's by the mapping

$$\hat{c}_n(t) = \sum_n T_{nm} \hat{b}_m(t), \quad (6.9)$$

where the mapping matrix element T_{nm} is the overlap integral

$$T_{nm} = \int dx v_n(x) u_m(x). \quad (6.10)$$

6.3 Linear dynamics

In this section, we compare the dynamics of ideal noninteracting bosonic and fermionic systems evolving under the influence of the Raman coupling. We proceed by numerically solving the Heisenberg equations of motion (6.6) for a sample of N atoms initially in the internal state $|+\rangle$ and at temperature $T = 0$. For bosonic atoms, all atoms are therefore initially in the “+”-trap ground state, while for fermions they fill the lowest N trap levels. The corresponding initial states are correspondingly

$$|\psi_F(0)\rangle = \prod_{i=0}^{N-1} \hat{a}_i^\dagger |0\rangle_+ \otimes |0\rangle_-, \quad (6.11)$$

in the case of fermions, and

$$|\psi_B(0)\rangle = \frac{1}{\sqrt{N!}} \hat{a}_0^{\dagger N} |0\rangle_+ \otimes |0\rangle_-, \quad (6.12)$$

for bosonic atoms.

We consider, first, the case of noninteracting fermionic atoms. For trap frequencies approximately equal, $\beta \simeq 1$, Eq. (6.6) suggests the existence of two limiting situations, at least in the case of fermions. (We will revisit this point when discussing low-temperature bosonic systems.) In the first one, which we call the “strong-coupling regime” in the following, $\tilde{g} \approx N$, so that the inter-trap coupling dominates the dynamics and the intra-trap coupling terms $\hat{b}_{n\pm 2}$ can largely be ignored. In contrast, the “weak-coupling regime” $\tilde{g} \ll N$ is dominated by intra-trap coupling.

As a first measure of the system dynamics, Fig. 6.2 shows³ the difference

$$\begin{aligned} \Delta N(\tau) &= \frac{1}{N} \int dx \left[\langle \hat{\Psi}_+^\dagger(x) \hat{\Psi}_+(x) \rangle - \langle \hat{\Psi}_-^\dagger(x) \hat{\Psi}_-(x) \rangle \right] \\ &= \frac{1}{N} \sum_n (\langle \hat{a}_n^\dagger(\tau) \hat{a}_n(\tau) \rangle - \langle \hat{c}_n^\dagger(\tau) \hat{c}_n(\tau) \rangle). \end{aligned} \quad (6.13)$$

between the populations of the “+” and “-” traps. Figure 6.2(a) is for the strong-coupling regime, and Fig. 6.2(b) for the weak-coupling regime.

One can gain some intuitive understanding of the strong-coupling regime by remarking that in that regime, intra-trap transitions remain small, so that the Raman coupling is predominantly between levels of the two traps with equal quantum

³All plots of the population difference ΔN exhibit fast oscillations that cannot be resolved on the shown time scale.

number n . To lowest order, these transitions are all at the Rabi frequency \tilde{g} . However, this simplest description cannot explain the result of Fig. 6.2(a). Rather, it is necessary to include at least their lowest-order corrections, i.e.,

$$\Omega_n = \sqrt{\tilde{g}^2 + \frac{1}{4}(A_n - B_n)^2} \simeq \tilde{g} + \left(\frac{(\beta - 1)^2}{8\tilde{g}} \right) n^2. \quad (6.14)$$

Such an n -dependence of Rabi frequencies is known to lead to collapse and revival phenomena, as was first discussed in the context of the Jaynes-Cummings model [167], where $\Omega_n \propto \sqrt{n}$. This is precisely the type of behavior exhibited by ΔN in the strong-coupling regime. Because of the n^2 -dependence of Ω_n , it is expected that the lowest trap levels, i.e. the atoms in the deep Fermi sea, play a dominant role in the appearance of the revivals. We verified that the populations of the lowest trap levels indeed oscillate more or less in phase, while those of higher n levels dephase rapidly.

We remark that both collapses and revivals of ΔN disappear when the two trap frequencies are identical, since for $\beta = 1$, we have $A_n = B_n = n$ and hence $\Omega_n = \tilde{g}$. In addition, intra-trap transitions vanish in that case, due to $C_n = D_n = 0$. Fig. 6.2(b) shows the inversion ΔN between the total trap populations in the weak-coupling regime, $\tilde{g} \ll N$. In this limit, inter-trap and intra-trap coupling occur on similar time scales. Immediately following a Raman transition from the $|+\rangle$ to the $|-\rangle$ internal state, the population of the “-”-trap starts to undergo a redistribution between its levels. The combined effects of the intra- and inter-trap transitions result in that case in a random-looking evolution of $\Delta N(t)$ of Fig. 6.2(b).

We now briefly turn to the case of a Bose gas. For a sample at zero-temperature, $T = 0$, and initially in the internal state $|+\rangle$, all atoms are in the ground state of the “+”-trap at $\tau = 0$. As a result, the strong-coupling regime is characterized by almost perfect Rabi oscillations of the atomic population between the two trap ground states, with a very small fraction of the atoms coupling to higher modes due to intra-trap transitions. This behavior is also largely preserved for $\beta^2 - 1 \ll \tilde{g} \ll N$. (We recall that for fermions the right-hand side of this inequality corresponds to the weak-coupling regime, dominated by intra-trap transitions.) This difference between bosons and fermions can readily be understood from Eqs. (6.6), which show that in the $T = 0$ bosonic case, intra-trap coupling first occurs between the levels $n = 0$ and $n = 2$ of the “-”-trap, with coupling coefficient $D_2 = (\beta^2 - 1)/4$. As long as this coupling remains small compared to the inter-trap coupling \tilde{g} , the system acts effectively as a two-mode system. In other words, for low temperature bosonic systems, the weak-coupling regime is not characterized by $\tilde{g} \approx N$ as is the case for fermions, but rather by $\tilde{g} \ll \beta^2 - 1$.

As is to be expected, the difference between fermionic and bosonic systems is reduced as T is increased. At first, the sharp edge of the Fermi-Dirac distribution softens, resulting in slightly reduced (strong-coupling) collapses and revivals of the fermionic system. On the other hand, for $T \neq 0$, bosons occupy higher trap states, resulting in a spread in Rabi frequencies participating in the population difference signal. This in turn leads to collapses and revivals rather than the perfect $T = 0$ Rabi oscillations. Increasing the temperature further leads of course to undistinguishable behaviors of the bosonic and fermionic systems.

6.4 Collisions

In this section, we discuss the effect of collisions on the preceding results. Collisions are of course central to the dynamics of quantum-degenerate atomic systems. They are essential in the evaporative cooling of the sample, and also provide a nonlinearity that can lead to the nonlinear mixing of matter waves. In bosonic systems, much

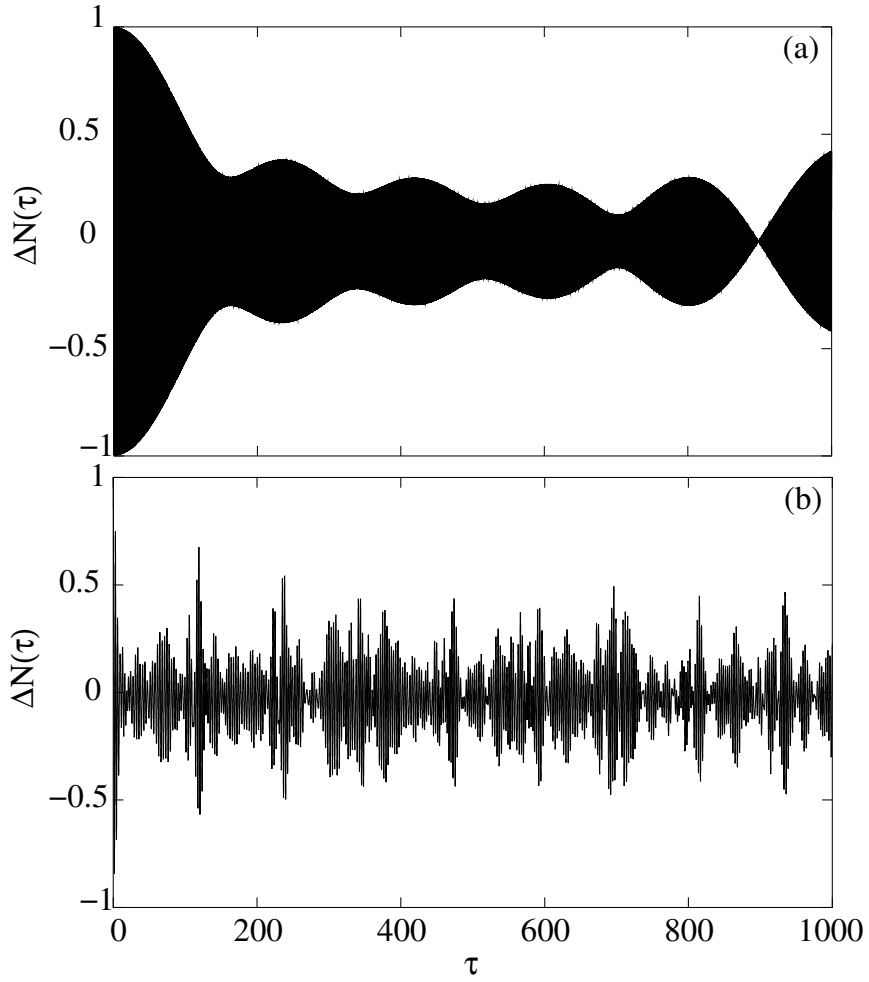


Figure 6.2: $\Delta N(\tau)$ for $N = 10$ fermions and trap ratio $\beta = 0.9$, as obtained from a numerical integration of Eqs. (6.6): (a) strong coupling regime with $\tilde{g} = 10.0$; (b) weak coupling regime with $\tilde{g} = 1.0$. Time τ is given in units of $1/\omega_+$.

new physics can be studied, e.g. by changing the sign of the scattering length of s -wave collisions. In the following sections, we first discuss the way collisions impact the operation of the Raman coupler in the case of fermions, and later compare these results with those for a bosonic sample.

6.4.1 Fermions

It is well known that in fermionic atoms, the Pauli exclusion principle forbids the existence of s -wave scattering between atoms in the same internal state. In addition, p -wave scattering is generally negligible. Hence two-body collisions are described by the Hamiltonian

$$\hat{\mathcal{H}}_{\text{col}} = U_0 \int dx \hat{\Psi}_+^\dagger(x) \hat{\Psi}_-^\dagger(x) \hat{\Psi}_-(x) \hat{\Psi}_+(x), \quad (6.15)$$

where $U_0 = 4\pi\hbar^2 a\rho/m$ is the interaction strength with a being the s -wave scattering length and ρ the characteristic density of the system. Again, we expand the field operators according to Eq. (6.5) in terms of the basis $\{u_n\}$ and obtain

$$\hat{H}_{\text{col}} = U_0 \sum_{i,j,k,l} U_{ijkl} \hat{a}_i^\dagger \hat{b}_j^\dagger \hat{b}_k \hat{a}_l, \quad (6.16)$$

where the matrix element

$$U_{ijkl} = \int dx u_i(x) u_j(x) u_k(x) u_l(x) \quad (6.17)$$

characterizes the scattering between different levels. We note that U_{ijkl} is symmetric under permutations.

In the presence of this quartic Hamiltonian, the Heisenberg equations of motion for the operators a_n and b_n involve cubic combinations of operators. To close this system of equations, we invoke a time-dependent Hartree-Fock ansatz, which has proved to be very successful in the treatment of many-particle quantum systems [168], to factorize products of operators, of the generic form $\hat{b}_i^\dagger(\tau) \hat{b}_j(\tau) \hat{a}_k(\tau)$, by

$$\hat{b}_i^\dagger(\tau) \hat{b}_j(\tau) \hat{a}_k(\tau) \approx \langle \hat{b}_i^\dagger(\tau) \hat{b}_j(\tau) \rangle \hat{a}_k(\tau) - \langle \hat{b}_i^\dagger(\tau) \hat{a}_k(\tau) \rangle \hat{b}_j(\tau), \quad (6.18)$$

where the expectation value is over the state $|\psi_F(0)\rangle$ since we work in the Heisenberg picture. At this level of approximation, we neglect all contributions from pairing. This factorization scheme readily yields the time-dependent Hartree-Fock equations of motion (in dimensionless variables)

$$\begin{aligned} i \frac{\partial \hat{a}_n}{\partial \tau} &= \sum_k \left[(A_n \delta_{nk} + Q_{nk}^{bb}) \hat{a}_k - (Q_{nk}^{ab*} - \tilde{g} \delta_{nk}) \hat{b}_k \right], \\ i \frac{\partial \hat{b}_n}{\partial \tau} &= \sum_k \left[(B_n \delta_{nk} + Q_{nk}^{aa}) \hat{b}_k - (Q_{nk}^{ab} - \tilde{g} \delta_{nk}) \hat{a}_k \right] \\ &+ C_n \hat{b}_{n+2} + D_n \hat{b}_{n-2}, \end{aligned} \quad (6.19)$$

where we have introduced the time-dependent coefficients

$$\begin{aligned} Q_{nk}^{aa}(\tau) &= \tilde{U}_0 \sum_{i,j} U_{nij} \langle \hat{a}_i^\dagger(\tau) \hat{a}_j(\tau) \rangle, \\ Q_{nk}^{bb}(\tau) &= \tilde{U}_0 \sum_{i,j} U_{nij} \langle \hat{b}_i^\dagger(\tau) \hat{b}_j(\tau) \rangle, \\ Q_{nk}^{ab}(\tau) &= \tilde{U}_0 \sum_{i,j} U_{nij} \langle \hat{a}_i^\dagger(\tau) \hat{b}_j(\tau) \rangle, \end{aligned} \quad (6.20)$$

and $\tilde{U}_0 = U_0/\hbar\omega_+$ is a dimensionless interaction strength.

The effect of collisions is illustrated in Figs. 6.3(a),(b), which show the population inversion $\Delta N(\tau)$ for two values of the interaction strength \tilde{U}_0 .

For weak enough collisions, the dynamics of the system is not significantly altered, as should of course be expected. However, we observe a quantitative change in the dynamics of ΔN as \tilde{U}_0 is increased. Instead of a collapse and revivals, $\Delta N(\tau)$ now undergoes nearly full Rabi oscillations.

A first hint at the cause of this changed behavior is offered by Fig. 6.4, which shows a snapshot of the level populations in the “+”-trap for the cases of Fig. 6.3(a) and 6.3(b), respectively. We observe that the smaller value of \tilde{U}_0 corresponds to an inhomogeneous level population distribution, whereas the higher nonlinearity causes the trap levels to be almost equally populated.

A more quantitative understanding of the role of collisions can be gained by estimating how the nonlinear terms in Eq. (6.19) modify the (collisionless) Rabi frequency. A numerical evaluation of the coefficients U_{ijkl} shows that elastic collisions, $i = j = k = l$, dominate the dynamics of the system. In addition, U_{nnnn} turns out to be a decreasing function of n . Keeping the elastic contributions to the collision-induced dynamics only, and neglecting as in the strong-coupling regime of Section 6.3 the effects of intra-trap coupling terms $\hat{b}_{n\pm 2}$, one finds that as a result of collisions Eq. (6.14) is approximately changed to

$$\Omega_n^{NL}(\tau) = \sqrt{g^2 + \frac{1}{4}(A_n - B_n + Q_{nn}^{bb}(\tau) - Q_{nn}^{aa}(\tau))^2}. \quad (6.21)$$

Fig. 6.5 shows, as a function of \tilde{U}_0 , the time-dependent Rabi frequencies $\Omega_n^{NL}(\tau)$ averaged over a time interval Θ large compared to their inverse,

$$\bar{\Omega}_n = \frac{1}{\Theta} \int_0^\Theta d\tau \Omega_n^{NL}(\tau). \quad (6.22)$$

Because U_{nnnn} is a decreasing function of n , its contribution tends to compensate the n^2 dependence of Eq. (6.14). As a result, there is a range of collision strengths for which the dependence of $\Omega_n^{NL}(\tau)$ on n largely disappears. In this range, paradoxically, the dynamics of the collision-dominated Fermi system resembles that of a collisionless Bose system. From this admittedly crude argument – which is however consistent with our full numerical results – we also conjecture that for even larger \tilde{U}_0 , the approximate cancellation of the n -dependence of the Rabi frequencies will disappear and we expect an overall dephasing and decay of the population difference $\Delta N(t)$. It has unfortunately proven prohibitive to try and check this conjecture numerically.

6.4.2 Bosons

We now turn to the case of bosonic atoms. Bose statistics allows for s -wave collisions between atoms in the same spin state, so that the collisional Hamiltonian is now

$$\begin{aligned} \hat{\mathcal{H}}_{\text{col}} &= U_+ \int dx \hat{\Psi}_+^\dagger(x) \hat{\Psi}_+^\dagger(x) \hat{\Psi}_+(x) \hat{\Psi}_+(x) \\ &+ U_- \int dx \hat{\Psi}_-^\dagger(x) \hat{\Psi}_-^\dagger(x) \hat{\Psi}_-(x) \hat{\Psi}_-(x) \\ &+ 2U_x \int dx \hat{\Psi}_+^\dagger(x) \hat{\Psi}_-^\dagger(x) \hat{\Psi}_+(x) \hat{\Psi}_-(x), \end{aligned} \quad (6.23)$$

where the U_i , $i = \{+, -, x\}$ characterize the strength of the collisions. In the following we assume for simplicity $U_+ = U_- = U_0$ and $U_x = \eta_x U_0$.

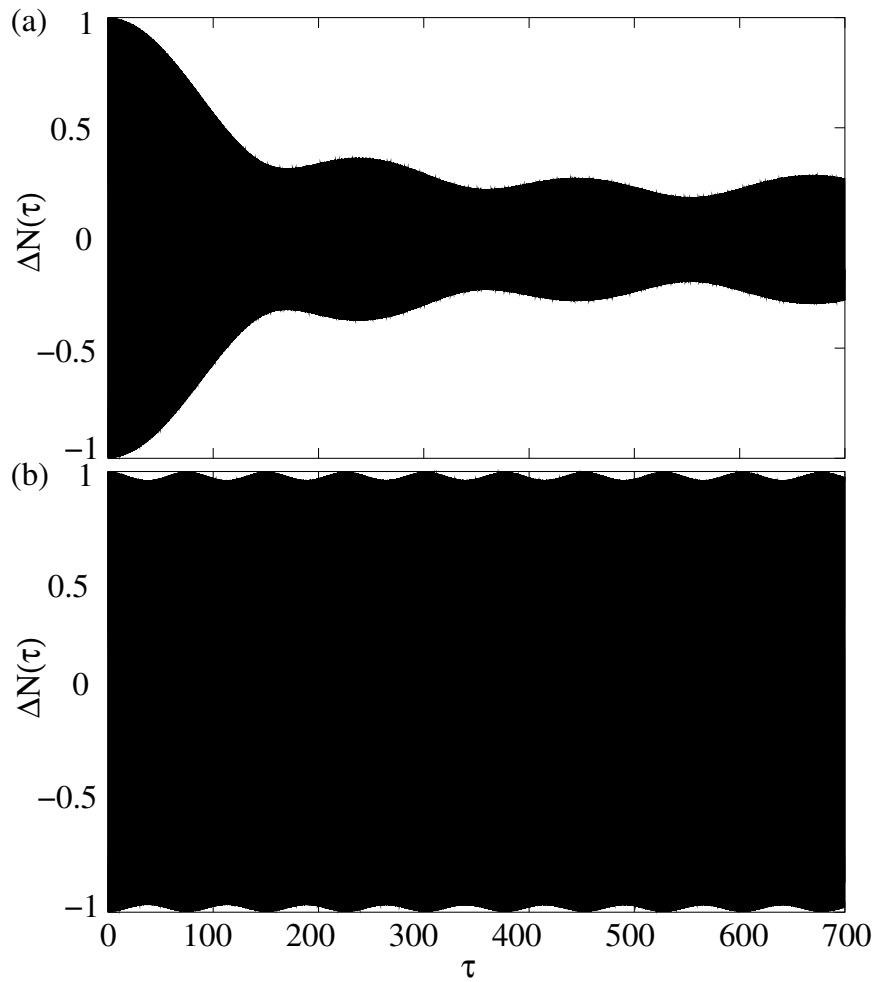


Figure 6.3: Population difference $\Delta N(\tau)$ for $N = 10$ fermions, a trap ratio $\beta = 0.9$ and in the strong-coupling regime $\tilde{g} = 10.0$. The plots, which result from the numerical integration of Eqs. (6.19), are for different strengths of the two-body collisions: (a) $\tilde{U}_0 = 0.01$; (b) $\tilde{U}_0 = 0.1$. Time τ is given in units of $1/\omega_+$.

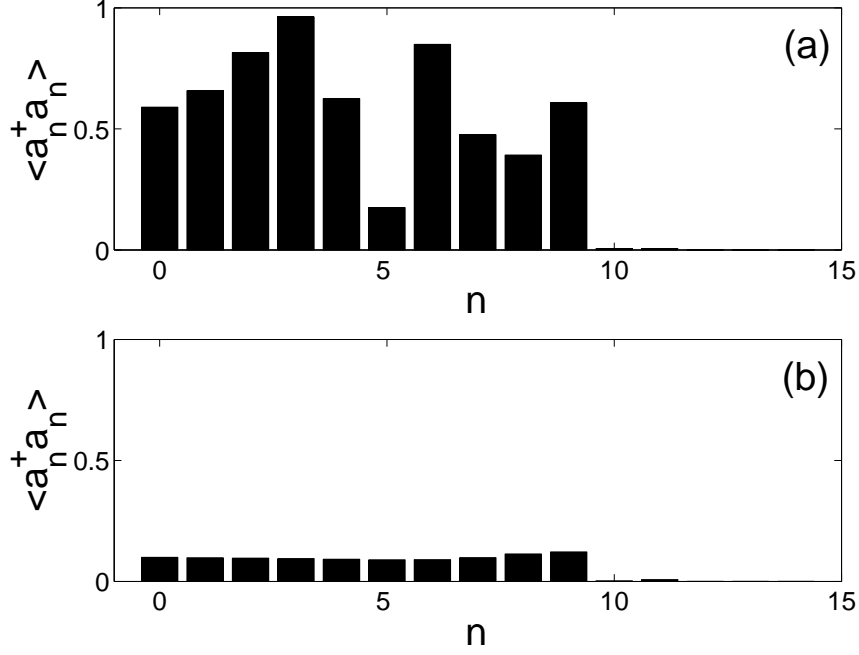


Figure 6.4: Occupation of the first 15 upper trap levels at time $\tau = 490$ (in units of $1/\omega_+$), (a) for the parameters of Fig. 6.3(a); (b) for the parameters of Fig. 6.3(b).

To truncate the Heisenberg equations of motion for the field operators, we now invoke a mean-field approximation, factorize all products of operators, and replace the resulting expectation values by time-dependent c -numbers. This gives

$$\begin{aligned}
 i \frac{d\langle \hat{a}_n \rangle}{d\tau} &= \sum_k (A_n \delta_{nk} + Q_{nk}^{aa} + \eta_x Q_{nk}^{bb}) \langle \hat{a}_k \rangle + \tilde{g} \langle \hat{b}_n \rangle, \\
 i \frac{\partial \langle \hat{b}_n \rangle}{\partial \tau} &= \sum_k (B_n \delta_{nk} + Q_{nk}^{bb} + \eta_x Q_{nk}^{aa}) \langle \hat{b}_k \rangle + \tilde{g} \langle \hat{a}_n \rangle \\
 &\quad + C_n \langle \hat{b}_{n+2} \rangle + D_n \langle \hat{b}_{n-2} \rangle,
 \end{aligned} \tag{6.24}$$

where

$$\begin{aligned}
 Q_{nk}^{aa}(\tau) &= 2\tilde{U}_0 \sum_{i,j} U_{nij} \langle \hat{a}_i(\tau) \rangle^* \langle \hat{a}_j(\tau) \rangle, \\
 Q_{nk}^{bb}(\tau) &= 2\tilde{U}_0 \sum_{i,j} U_{nij} \langle \hat{b}_i(\tau) \rangle^* \langle \hat{b}_j(\tau) \rangle,
 \end{aligned} \tag{6.25}$$

and the expectation values are with respect to the state $|\psi_B(0)\rangle$. Figure 6.6 shows the inversion $\Delta N(\tau)$ for a sample of bosonic atoms initially in the internal state $|+\rangle$ for a nonlinear parameter $\tilde{U}_0 = 0.5$. In contrast to the case where collisions are absent and we have full Rabi oscillations, see Section 6.3, here one starts observing a damping of the oscillations. This is clearly a result of the scattering of atoms into higher trap states. This is illustrated in Fig. 6.7, which shows the population of the first upper trap levels at a fixed time. The transitions between the populated trapped states are characterized by n -dependent Rabi-frequencies, leading to the

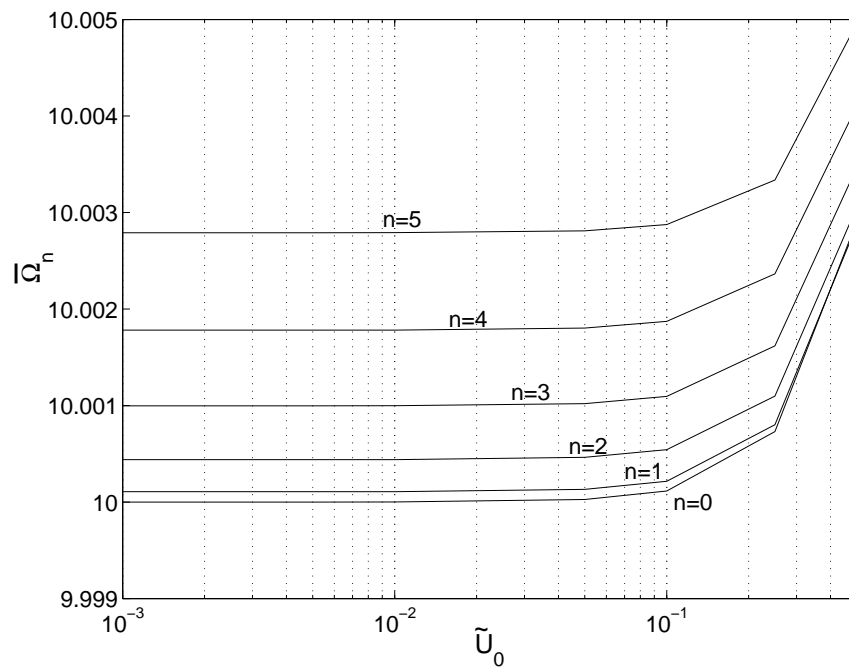


Figure 6.5: Semi-logarithmic plot of the time-averaged generalized Rabi frequencies for the six lowest trap levels as a function of the nonlinear parameter, otherwise the same parameters as in Fig. 6.3 are used. $\bar{\Omega}_n$ is given in units ω_+ , \tilde{U}_0 in units of $\hbar\omega_+$.

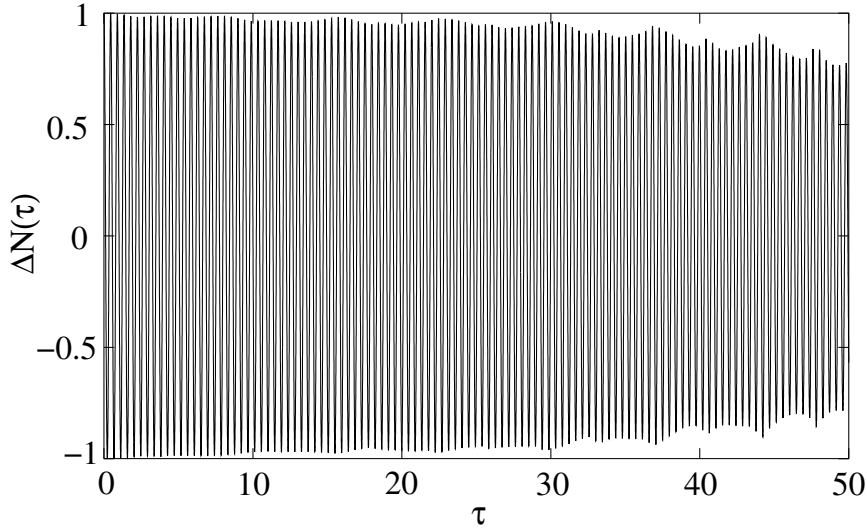


Figure 6.6: $\Delta N(\tau)$ for $N = 20$ bosons, trap ratio $\beta = 0.9$, linear coupling $\tilde{g} = 7.0$ and $\eta_x = 1.5$, from the numerical solution of Eq. (6.24) with $\tilde{U}_0 = 0.5$. Time τ is given in units of $1/\omega_+$

onset of a dephasing process resembling the situation for noninteracting fermions.⁴ We see, then, that in the case of interacting bosons, intra-trap scattering is an important element of the dynamics of the Raman coupler, which rapidly evolves to a multimode behavior; in contrast to the intrinsically multimode fermionic case U_{ijkl} tends to reduce the spread in Rabi frequencies and thus inhibits dephasing.

A remarkable property of the bosonic trap population distribution is that only even trap levels are occupied, see Fig. 6.7. This is a combined result of three facts: (a) at $T = 0$ all atoms are initially in the ground state of one of the traps; (b) s -wave scattering only couples trap states of same parity, as expressed by the symmetry properties of the collision matrix from Eq. 6.17; (c) intra-trap coupling only couples trap levels with $\Delta n = 2$, see Eq. (6.6).

It is known from nonlinear optics [169] and atom optics [170] that systems governed by a pair of coupled nonlinear Schrödinger equations can reach a regime where the nonlinear phase shifts dominate their dynamics. Such two-mode systems exhibit Rabi oscillations for small nonlinearities, but mode-coupling is inhibited above a certain strength of the nonlinearity. This effect is absent in the present multimode system, a result of the strong inter-mode scattering.

⁴The choice of a given number of modes in the numerical simulations limits the evolution time to values such that the population of modes close to the numerical cut-off point remains small.

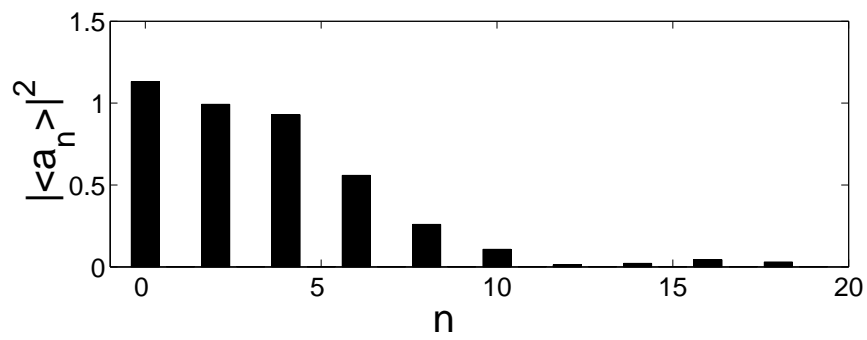


Figure 6.7: Level population of the “+”-trap at time $\tau = 25$ (in units of $1/\omega_+$) for the parameters of Fig. 6.6.

Chapter 7

Summary and Conclusion

In this dissertation, we presented a variety of momentum state manipulation techniques for matter waves, reaching from constantly accelerating Bose-Einstein condensates to introducing optimization schemes to create arbitrary coherent momentum state superpositions. Using these tools we were also able to show efficient excitation of atomic gap solitons.

Shortly after the publication of our results for the coherent acceleration of Bose-Einstein condensates, its experimental feasibility was demonstrated by two different research groups [1, 2] in agreement with our predictions. Besides emphasizing the timeliness of the theoretical analysis this also shows the necessity in current research to control the motion of a condensate. Very recently, even atomic gap solitons were experimentally excited, again in good agreement with our predictions and numerical simulations [3]. It is very likely that, together with the rapid improvement in the field of integrated atom optics, these achievements soon lead to unprecedented controlled guiding of condensate wave packets on microfabricated atom waveguides.

From a theoretical point of view there still remain open issues that could evolve into new tools for coherent manipulation. As for the acceleration of Bose-Einstein condensates, it seems possible to combine the ideas of adiabaticity and non-trivial lattice acceleration to create a counterintuitive process similar to STIRAP (stimulated Raman adiabatic passage). Specifically, controlling the time-dependent acceleration of the lattice such that the Bragg resonances are swept continuously from higher to lower momentum modes of the condensate, thereby building up a coherence between these modes, should then result in an efficient transfer from an initial state of low momentum to one of high momentum. Preliminary investigations indicate that this method could be well suited for the construction of large-momentum beam splitters. Another direction besides the counterintuitive acceleration is to go past the mean-field theory in order to determine the higher-order coherence properties of the accelerated beams. With this understanding one can imagine to be able to generate non-classical matter wave fields during the acceleration process.

Furthermore, genetic algorithm optimization, that we used for the acceleration of condensates and the excitation of gap solitons, is expected to play an important role in the preparation of quantum states of ultracold or condensed atomic systems. After being a well-established tool in e.g. physical chemistry, other groups now also started to theoretically apply control optimization to manipulate Bose-Einstein condensates. As an example, Ref. [171] demonstrates the creation of a flat spatial phase with the help of an optical lattice. However, there are some issues that have to be resolved, such as the inclusion of laser and atom number fluctuations into the numerical simulations. This is necessary so that the calculated control pulses can be used in actual experiments. A first step towards this goal has been achieved in optimal control theory [172], where uncertainties in pulse duration are admitted.

However, apart from numerical simulations, feedback optimization can also directly be used in experimental setups. Especially the short production times for Bose-Einstein condensates on microfabricated chips and the possibility to design interesting spatial and time-dependent potentials makes these systems good candidates for these techniques. Besides quantum state engineering it also seems possible to use genetic algorithm feedback loops for the optimization of experimental procedures that need many trial-and-error adjustments, such as finding optimal ramping times for the cooling of fermions.

In the last part of the dissertation we gave an outlook on possible quantum state manipulation techniques with fermions. We found that the Raman coupling between two internal states of a trapped Fermi gas exhibits rich dynamics, quite different from its bosonic counterpart. This is of course due primarily to the fact that a Fermi gas occupies a large number of trap states, and hence can never be approximated as a two-mode system. Surprisingly perhaps, we also found that two-body collisions can under appropriate conditions inhibit collapses and revivals. Despite the limitation of restricting the numerical simulations to fairly small numbers of atoms on the order of 10, the analysis sheds some light on the dynamics of trapped Fermi systems. This might provide useful guidance in understanding more realistic trapped Fermi gases in three dimensions and with a large number of fermionic atoms, so one can start developing coherent manipulation tools also for fermionic systems.

In conclusion, one needs to harness atomic properties in order to succeed building atom-optical devices, such as integrated atomic sensors or robust quantum computers. We introduced some new techniques and pointed out possible extensions of these schemes. The major challenge is now to combine several tools introduced by different groups to advance the field of atom optics step by step.

Appendix A

Numerical Methods

It is possible to obtain approximate solutions or reasonable analytical estimates for the momentum control schemes we demonstrate throughout this dissertation. However, numerical verification of these control schemes is necessary, especially in the presence of nonlinear atom-atom interactions. In this Appendix we review the most important numerical methods we used. We discuss a finite-difference scheme used to calculate ground states of the nonlinear GPE. For propagation in time, we introduce a split-step Fourier method for the one-dimensional case and a finite-difference scheme for three-dimensional cylindrically symmetric geometries.

A.1 Discretization

Domain and function discretization

We discretize the equations for numerical treatment by defining a grid of space-time points for the one-dimensional Cartesian coordinate z and the three-dimensional cylindrical coordinates r and z .¹ We divide the domain along the r -axis into M sections of length Δr and the domain along the z -axis into $L-1$ pieces of length Δz . For convenience we choose M an odd and L to be an even integer. The temporal step size is denoted by Δt . We then write for a space-time point on the grid

$$(r, z, t) \rightarrow (i\Delta r, [2j - L + 1]\Delta z/2, n\Delta t), \quad (\text{A.1})$$

where i, j, n are integers with $0 \leq i \leq M$, $0 \leq j < L$ and $n \geq 0$. Thus, the grid points cover a finite domain for the coordinates r and z , bounded by $0 \leq r \leq M\Delta r$ and $-(L-1)\Delta z/2 \leq z \leq (L-1)\Delta z/2$.

We introduce the following notation for a discretized arbitrary function f , that depends on the spatial variable r or z or on both:

$$\begin{aligned} f_i^n &\equiv f(i\Delta r, n\Delta t), \\ f_j^n &\equiv f([2j - L + 1]\Delta z/2, n\Delta t), \\ f_{i,j}^n &\equiv f(i\Delta r, [2j - L + 1]\Delta z/2, n\Delta t), \end{aligned} \quad (\text{A.2})$$

the upper index corresponding to time, the lower indices to space.

Derivative discretization

Having introduced the discretized space-time grid, we can now approximate derivatives by their most simple symmetric finite-difference approximation[173]. A first-

¹Since we only consider radially symmetric situations in three dimensions, we drop the angular dependence, as explained in Section 5.3.2.

order spatial derivative in r can be written as

$$\frac{\partial}{\partial r} f(r) \approx \frac{f_{i+1} - f_{i-1}}{2\Delta r}, \quad (\text{A.3})$$

whereas a second-order derivative is given by

$$\frac{\partial^2}{\partial r^2} f(r) \approx \frac{f_{i+1} - 2f_i + f_{i-1}}{\Delta r^2}. \quad (\text{A.4})$$

One obtains the corresponding derivatives in the z -space by replacing the coordinate r by z and the index i by j .

A.2 Nonlinear ground state method

Following Ref. [174], we discuss a numerical method to calculate the ground state solution of the nonlinear GPE. The stationary GPE from Eq. (2.11), reduced to one dimension, reads

$$H\psi = \mu\psi, \quad (\text{A.5})$$

with the Hamiltonian H given by

$$H = -\frac{\hbar^2}{2M} \frac{\partial^2}{\partial z^2} + V(z) + NU_0 |\psi(z)|^2. \quad (\text{A.6})$$

Using Eqs. (A.2) and (A.4), we write the discretized version of Eq. (A.5) as

$$\frac{-\hbar^2}{2M\Delta z^2} (\psi_{j+1} - 2\psi_j + \psi_{j-1}) + V_j \psi_j + NU_0 |\psi_j|^2 \psi_j = \mu\psi_j. \quad (\text{A.7})$$

We can then rewrite the Hamiltonian in form of a tridiagonal matrix,

$$H = \begin{pmatrix} \ddots & & & & & & \\ & \ddots & & & & & \\ & & d_{j-1} & \kappa & & & \\ & & \kappa & d_j & \kappa & & \\ & & & \kappa & d_{j+1} & \ddots & \\ & & & & \ddots & \ddots & \\ & & & & & & \ddots \end{pmatrix}, \quad (\text{A.8})$$

where we used $d_j = \hbar^2/M\Delta z^2 + V_j + NU_0 |\psi_j|^2$ and $\kappa = -\hbar^2/2M\Delta z^2$. We apply free boundary conditions by setting $\psi_j = 0$ outside the domain, i.e. for $j < 0$ or $j \geq L$.

Without the nonlinear term, the problem is readily solved by calculating the eigenvalues and eigenvectors² of the matrix H in Eq. (A.8): the lowest eigenvalue corresponds to the ground state energy and the associated eigenvector is the discretized ground state wave function. Including the nonlinearity, we have to use an iterative method. Starting with a trial wave function $\psi_j^{(0)}$, we calculate the eigenvector $\psi_j^{(EV)}$ corresponding to the lowest eigenvalue. We then construct a new trial function from the first trial function and the calculated eigenfunction by letting

$$\psi_j^{(1)} = \sqrt{\epsilon \left[\psi_j^{(0)} \right]^2 + (1 - \epsilon) \left[\psi_j^{(EV)} \right]^2}, \quad (\text{A.9})$$

²The eigenvalues and eigenvectors of the matrix can efficiently be calculated by software packages such as MATLAB or LAPACK.

with $0 < \epsilon < 1$ is. The above procedure is then iterated with the newly constructed trial function until the trial function agrees with the calculated eigenfunction $\psi_j^{(EV)}$ within a certain range, yielding the nonlinear ground state. Crucial parameters are the mixing parameter ϵ and the choice of the first trial function. In general, a small ϵ leads to a slow but stable convergence. A good choice for $\psi_j^{(0)}$ is the harmonic oscillator ground state if the trapping potential can be Taylor-expanded around its minimum.

A.3 Split-operator method

A very powerful method for numerical propagation in the time domain is the so-called split-operator method. We assume that the Hamiltonian of the system can be decomposed into a sum of two operators that are allowed to be nonlinear and time-dependent,

$$H(t) = \mathcal{L}_1(t) + \mathcal{L}_2(t). \quad (\text{A.10})$$

The system evolution is governed by the Schrödinger equation

$$i\hbar \frac{\partial}{\partial t} \psi(t) = H(t) \psi(t), \quad (\text{A.11})$$

which is formally be solved by

$$\psi(t + \Delta t) = \hat{T} \left\{ \exp \left[-\frac{i}{\hbar} \int_t^{t+\Delta t} dt' H(t') \right] \right\} \psi(t), \quad (\text{A.12})$$

where \hat{T} is the time-ordering operator. If the equal-time commutator of the Hamiltonian H vanishes, we can neglect terms of order $\mathcal{O}(\Delta t^3)$ in Eq. (A.12) and approximate the integral by evaluating H at time t , leaving us with

$$\begin{aligned} \psi(t + \Delta t) &\approx \exp \left[-\frac{i}{\hbar} H(t) \Delta t \right] \psi(t) \\ &= \exp \left[-\frac{i}{\hbar} (\mathcal{L}_1 + \mathcal{L}_2) \Delta t \right] \psi(t). \end{aligned} \quad (\text{A.13})$$

Here, we made use of the decomposition in Eq. (A.10). According to the Baker-Hausdorff formula we can write

$$\begin{aligned} &\exp \left(-\frac{i}{\hbar} \mathcal{L}_1 \Delta t \right) \exp \left(-\frac{i}{\hbar} \mathcal{L}_2 \Delta t \right) \\ &= \exp \left\{ -\frac{i}{\hbar} (\mathcal{L}_1 + \mathcal{L}_2) \Delta t - \frac{1}{2\hbar^2} [\mathcal{L}_1, \mathcal{L}_2] \Delta t^2 + \mathcal{O}(\Delta t^3) \right\} \\ &\approx \exp \left[-\frac{i}{\hbar} (\mathcal{L}_1 + \mathcal{L}_2) \Delta t \right], \end{aligned}$$

where we neglected terms of order $\mathcal{O}(\Delta t^2)$ in the last step. Using this identity in Eq. (A.13), we can calculate $\psi(t + \Delta t)$ by successively applying the exponentials containing \mathcal{L}_1 and \mathcal{L}_2 to the initial wave function $\psi(t)$,

$$\psi(t + \Delta t/2) = \exp \left[-\frac{i}{\hbar} \mathcal{L}_1(t) \Delta t \right] \psi(t), \quad (\text{A.14})$$

$$\psi(t + \Delta t) = \exp \left[-\frac{i}{\hbar} \mathcal{L}_2(t + \Delta t/2) \Delta t \right] \psi(t + \Delta t/2). \quad (\text{A.15})$$

The total Hamiltonian evolution is divided into two parts: first, the function ψ is computed at the intermediate time $t + \Delta t/2$ by evolving the system according to \mathcal{L}_1 . Then, in a second step, the final function at $t + \Delta t$ is obtained by evolving the intermediate result according to \mathcal{L}_2 .

A.4 Split-operator method for one-dimensional GPE

We are now ready to apply the split-operator solutions from Eqs. (A.14) and (A.15) to the one-dimensional time-dependent GPE from Eq. (2.28),

$$i\hbar \frac{\partial}{\partial t} \psi(z, t) = \left[-\frac{\hbar^2}{2M} \frac{\partial^2}{\partial z^2} + V(z, t) \right] \psi(z, t) + NU_0 |\psi(z, t)|^2 \psi(z, t). \quad (\text{A.16})$$

Operator splitting and solutions

We split the Hamiltonian into a part \mathcal{L}_1 , consisting of the kinetic energy term, and a part \mathcal{L}_2 , which contains the linear and nonlinear potential, by defining

$$\mathcal{L}_1 = -\frac{\hbar^2}{2M} \frac{\partial^2}{\partial z^2}, \quad (\text{A.17})$$

$$\mathcal{L}_2(t) = V(z, t) + NU_0 |\psi(z, t)|^2. \quad (\text{A.18})$$

The propagation of the wave function from time t to $t + \Delta t/2$ with the operator \mathcal{L}_1 according to Eq. (A.14) is best done by introducing the Fourier transform $\phi(k, t)$, defined as

$$\phi(k, t) = \frac{1}{\sqrt{2\pi}} \int_{-\infty}^{\infty} dz \psi(z, t) e^{-ikz}. \quad (\text{A.19})$$

After the transformation of the wave function $\psi(z, t)$ to momentum space, the evolution according to \mathcal{L}_1 is then given by

$$\phi(k, t + \Delta t/2) = \exp\left(-i \frac{\hbar}{2M} k^2 \Delta t\right) \phi(k, t). \quad (\text{A.20})$$

Transforming $\phi(k, t + \Delta t/2)$ back to coordinate space, we can apply the second computational step. The propagation with operator \mathcal{L}_2 according to Eq. (A.15) is then simply

$$\begin{aligned} \psi(z, t + \Delta t) &= \exp\left[-\frac{i}{\hbar} V(z, t + \Delta t/2) \Delta t\right] \\ &\times \exp\left[-\frac{i}{\hbar} NU_0 |\psi(z, t + \Delta t/2)|^2 \Delta t\right] \\ &\times \psi(z, t + \Delta t/2). \end{aligned} \quad (\text{A.21})$$

Discretized scheme

Implementation of this propagation method from time t to $t + \Delta t$ on the one-dimensional grid requires the values of the wave function ψ_j^n for all j to be known at time $t = n\Delta t$ as an initial condition. For the evolution according to the kinetic energy operator \mathcal{L}_1 we first use a discrete Fourier transform³ to obtain ϕ_l^n , with $-L/2 \leq l < L/2$, from ψ_j^n . Properly discretized, the solution from Eq. (A.20) is written as

$$\phi_l^{n+1/2} = \exp\left[-i \frac{\hbar}{2M} (l\Delta k)^2 \Delta t\right] \phi_l^n, \quad (\text{A.22})$$

³For computational efficiency a Fast Fourier Transform algorithm is recommended [175].

with the step size in momentum space given by $\Delta k = 2\pi/(L-1)\Delta z$. Dcretization of the second computational step in Eq. (A.21) yields

$$\psi_j^{n+1} = \exp \left[-\frac{i}{\hbar} \left(V_j^{n+1/2} + NU_0 |\psi_j^{n+1/2}|^2 \right) \Delta t \right] \psi_j^{n+1/2}. \quad (\text{A.23})$$

A.5 Finite-difference scheme for cylindrical symmetry

In Cartesian coordiantes, the above stated Fourier method can easily be extended to three dimensions, whereas in cylindrical coordinates the Fourier transform has to be replaced by a Hankel transform. However, numerical implementations of the Hankel transform are less accurate than the fast Fourier algorithms and require an exponentially spaced grid along the r -axis [176]. Therefore, we employ a different approach based on a finite-difference scheme.

In Section 5.3.2, we need to propagate the GPE in cylindrical coordinates,

$$\begin{aligned} i\hbar \frac{\partial}{\partial t} \psi(r, z, t) &= -\frac{\hbar^2}{2M} \left(\frac{\partial^2}{\partial r^2} + \frac{1}{r} \frac{\partial}{\partial r} + \frac{\partial^2}{\partial z^2} \right) \psi(r, z, t) \\ &+ \left[V(r, z) + NU |\psi(r, z, t)|^2 \right] \psi(r, z, t). \end{aligned} \quad (\text{A.24})$$

We assume a time-indepnent potential of the form

$$V(r, z) = V(r) + V(z), \quad (\text{A.25})$$

which is the case for the situation discussed in Section 5.3.2. There, the radial part $V(r)$ corresponds to a harmonic trapping potential and the longitudinal potential $V(z)$ models the optical lattice along the z -axis.

Operator splitting and solutions

We apply the operator splitting as discussed in Section A.3 and divide the Hamiltonian into a a nonlinear part \mathcal{L}_1 and a linear part \mathcal{L}_2 , containing the kinetic energy contributions as well as the trapping and lattice potential,

$$\mathcal{L}_1(t) = NU |\psi(r, z, t)|^2, \quad (\text{A.26})$$

$$\mathcal{L}_2 = -\frac{\hbar^2}{2M} \left(\frac{\partial^2}{\partial r^2} + \frac{1}{r} \frac{\partial}{\partial r} + \frac{\partial^2}{\partial z^2} \right) + V(r, z). \quad (\text{A.27})$$

The solution of the the nonlinear operator \mathcal{L}_1 , according to Eq. (A.14), is readily given by

$$\psi(r, z, t + \Delta t/2) = \exp \left(-\frac{i}{\hbar} NU |\psi(r, z, t)|^2 \Delta t \right) \psi(r, z, t), \quad (\text{A.28})$$

propagating the wave function from time t to $t + \Delta t/2$. The solution of the linear term \mathcal{L}_2 is more complicated since it contains derivatives of both coordinates r and z . A common scheme to solve the propagation from $t + \Delta t/2$ to $t + \Delta t$ is to apply another operator splitting, this time separating the coordinates,

$$\mathcal{L}_2 = \mathcal{L}_r + \mathcal{L}_z, \quad (\text{A.29})$$

with

$$\mathcal{L}_r = -\frac{\hbar^2}{2M} \left(\frac{\partial^2}{\partial r^2} + \frac{1}{r} \frac{\partial}{\partial r} \right) + V(r), \quad (\text{A.30})$$

$$\mathcal{L}_z = -\frac{\hbar^2}{2M} \frac{\partial^2}{\partial z^2} + V(z), \quad (\text{A.31})$$

where we made use of the decomposition of the potential $V(r, z)$ in Eq. (A.25). We are now able to use the *Alternate Direction Implicit* (ADI) scheme [173]. This powerful method reduces the two-dimensional problem to a succession of two one-dimensional problems, similar to the operator splitting in time. The specific implementation we use is based on work by Peaceman and Rachford and uses the formulas

$$\left(I + i\frac{\Delta t}{2\hbar}\mathcal{L}_r\right)\psi(t + 3\Delta t/4) = \left(I - i\frac{\Delta t}{2\hbar}\mathcal{L}_z\right)\psi(t + \Delta t/2), \quad (\text{A.32})$$

$$\left(I + i\frac{\Delta t}{2\hbar}\mathcal{L}_z\right)\psi(t + \Delta t) = \left(I - i\frac{\Delta t}{2\hbar}\mathcal{L}_r\right)\psi(t + 3\Delta t/4), \quad (\text{A.33})$$

where I is the identity matrix. First, the wave function is propagated from time $t + \Delta t/2$ to $t + 3\Delta t/4$ with the operator \mathcal{L}_z . Then, application of \mathcal{L}_r yields the final wave function at $t + \Delta t$. Since the method is derived from the famous Crank-Nicolson scheme for parabolic partial differential equations [175], it is unconditionally stable [173].

Discretized scheme

The discretized version of the split operator solution for \mathcal{L}_1 in Eq. (A.28) simply reads

$$\psi_{i,j}^{n+1/2} = \exp\left(-\frac{i}{\hbar}NU|\psi_{i,j}^n|^2\Delta t\right)\psi_{i,j}^n, \quad (\text{A.34})$$

where the values $\psi_{i,j}^n$ for all i, j serve as the initial condition and are assumed to be known.

For the discretization of the ADI method in Eqs. (A.32) and (A.33) we introduce the abbreviations

$$\mu = \frac{\Delta t}{2\hbar}, \quad \mu_r = \frac{\hbar\Delta t}{2M\Delta r^2} \quad \text{and} \quad \mu_z = \frac{\hbar\Delta t}{2M\Delta z^2}. \quad (\text{A.35})$$

According to Eq. (A.32), the first propagation step is then properly discretized by

$$\begin{aligned} & \mu_r \frac{2i+1}{4i} \psi_{i+1,j}^{n+3/4} + (i - \mu_r - \mu V_i) \psi_{i,j}^{n+3/4} + \mu_r \frac{2i-1}{4i} \psi_{i-1,j}^{n+3/4} \\ &= -\frac{\mu_z}{2} \psi_{i,j+1}^{n+1/2} + (i + \mu_z + \mu V_j) \psi_{i,j}^{n+1/2} - \frac{\mu_z}{2} \psi_{i,j-1}^{n+1/2}, \end{aligned}$$

for $1 \leq i \leq M-1$ and $1 \leq j \leq L-2$. These equations correspond to $L-2$ tridiagonal systems, one for each value of j . Each tridiagonal system can be solved for the values $\psi_{i,j}^{n+3/4}$ with $0 \leq i \leq M$, since the right hand side is completely known from Eq. (A.34). The Thomas algorithm [173] turned out to be an appropriate method to solve the tridiagonal systems at hand. Next, we specify the missing values at the boundaries by $\psi_{i,0}^{n+3/4} = \psi_{i,L-1}^{n+3/4} = 0$, corresponding to a vanishing wave function at the domain boundaries $z = \pm(L-1)\Delta z$. Having computed all values at time $t + 3\Delta t/4$ by this procedure, discretization of the second stage of the computation due to Eq. (A.33) yields $M-1$ tridiagonal systems,

$$\begin{aligned} & \frac{\mu_z}{2} \psi_{i,j+1}^{n+1} + (i - \mu_z - \mu V_j) \psi_{i,j}^{n+1} + \frac{\mu_z}{2} \psi_{i,j-1}^{n+1} \\ &= -\mu_r \frac{2i+1}{4i} \psi_{i+1,j}^{n+3/4} + (i + \mu_r + \mu V_i) \psi_{i,j}^{n+3/4} - \mu_r \frac{2i-1}{4i} \psi_{i-1,j}^{n+3/4}, \end{aligned}$$

for $1 \leq i \leq M-1$ and $1 \leq j \leq L-2$. Again, we use the Thomas algorithm to solve these system of equations to obtain the values $\psi_{i,j}^{n+1}$ for $0 \leq j < L$. The boundaries in this case are then specified by $\psi_{0,j}^{n+1} = \psi_{1,j}^{n+1}$, which assures a vanishing derivative at $r = 0$, and $\psi_{M,j}^{n+1} = 0$, corresponding to a vanishing wave function at the domain boundary $r = M\Delta r$.

Appendix B

Details of Genetic Algorithm

In this Appendix we give specific details of the implementation of the genetic algorithm in the problem of BEC state engineering in an optical lattice from Chapter 4.

Over the course of the optimization we monitor the maximum fitness f_{\max} of a population,

$$f_{\max} = \max\{f(c_i) : i = 1, \dots, \mathcal{N}\}. \quad (\text{B.1})$$

Obviously, if at least the best chromosome is kept from the old generation, the maximum fitness is a monotonically increasing function. This feature, referred to as *elitism*, is used throughout our simulations. Another observable of interest is the mean fitness f_{mean} of a population,

$$f_{\text{mean}} = \frac{1}{\mathcal{N}} \sum_{i=1}^{\mathcal{N}} f(c_i). \quad (\text{B.2})$$

A typical evolution of these two quantities is shown in Fig. B.1(a). The maximum fitness increases monotonically to reach a value close to the optimum after about 40 generations. In contrast, the mean fitness rises over the course of the first 10 generations and then exhibits fluctuations due to the stochastic character of the genetic algorithm: Parts of the population are replaced by randomly created chromosomes from one generation to the next and randomize the mean fitness value. In our simulations we used populations of size $\mathcal{N} = 50 - 100$ and performed the optimization over 50 - 100 generations. We always kept the best chromosomes of a generation and replaced 80% - 90% of the population by newly generated chromosomes. For the population transfer of Section 4.2 we used 16, and for the superposition state engineering of Section 4.3 26 genes per chromosome. The gene boundaries were chosen as $-1.4\omega_R \leq a_{i\nu}, b_{i\nu} \leq 1.4\omega_R$.

As mentioned in Section 4.1, we use an adaptive operator technique, where the operators themselves are dynamically assigned a fitness based on their performance. Choosing a particular mating operator via a roulette-wheel method [102] then assures that good operators are employed more often in the mating process, just the same way as good parent chromosomes reproduce more often. If any operator produces an offspring that is better than the best chromosome of the previous generation, we reward this operator by giving it a credit proportional to the increase in fitness it caused. Also, we pass half of this given credit back to the operator that created the parent chromosome involved in producing the better offspring. Thus operators that perform well and also their direct ancestors can accumulate credit over the run of the simulation. Passing credit back to previous operators enables us to reward pairs of operators that work well together at a certain stage of the optimization process. In our simulations we adjust the fitness of all operators every

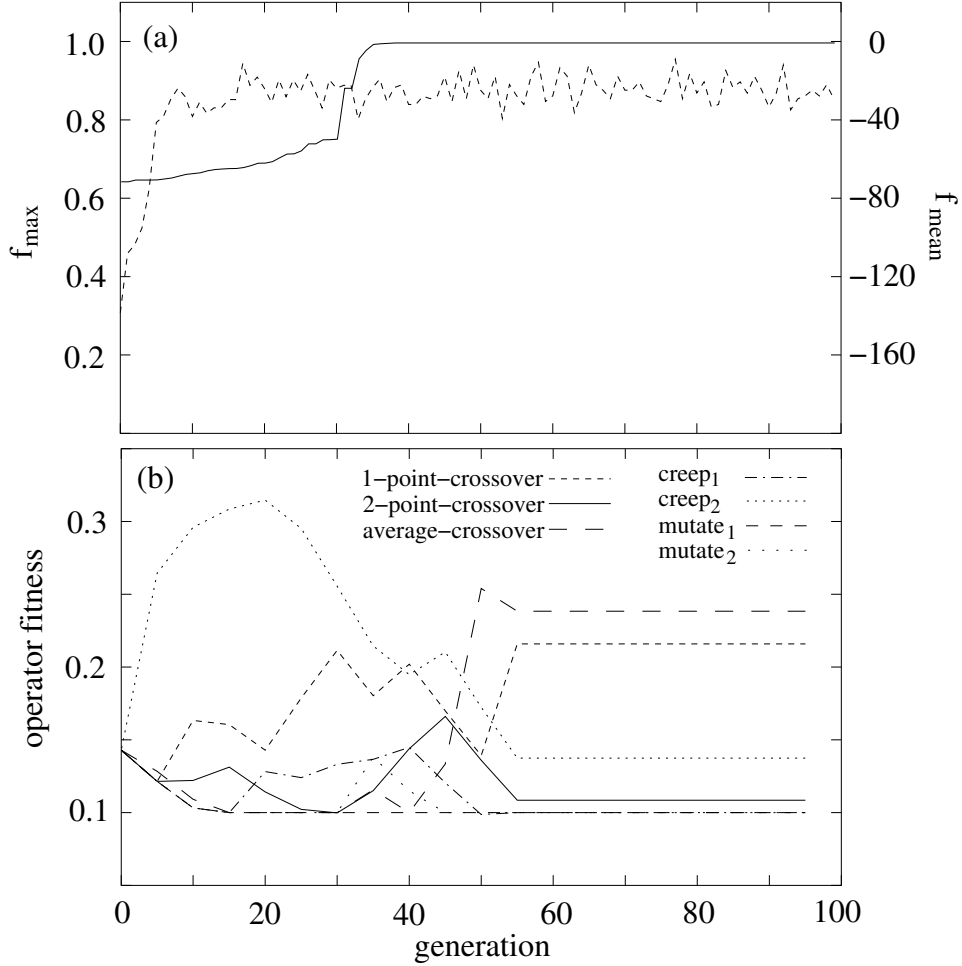


Figure B.1: A typical run of the genetic algorithm for the superposition state engineering: (a) Maximum fitness (solid) and mean fitness (dashed) of the population as a function of the generation. We started the optimization with pre-optimized chromosomes from previous simulations, which explains the high initial maximum fitness of over 60%. (b) Operator fitness as a function of the generation, starting with equal fitness for all operators. The minimum operator fitness is set equal to 0.1 for all operators.

five generations based on the credit they accumulated during that period: The new operator fitness is then a weighted sum of the old fitness (the *basis portion*, in our case 85%) and the accumulated credit (the *adaptive portion*, in our case 15%). The more credit an operator accumulates the higher will be its new fitness and the more likely it is that it will be chosen in future mating processes. Since the total operator fitness is set constant, we introduce a lower bound of 0.1 to the operator fitness, thereby preventing operators that do not perform well over several generations from being practically expelled from the pool of operators.

Fig. B.1(b) shows a typical evolution of the fitness of the individual mating operators in the superposition state engineering problem from Section 4.3. The creep and one-point-crossover operators perform well for the first 30 generations. For subsequent generations the two-point-crossover and the average-crossover operators take over and help increasing the maximum fitness, which approaches its optimum value (unity in the present example). There is no further improvement in the remaining 50 generations, the fitness of the various operators staying constant. The random mutation operators never perform well in the problem at hand. Consequently their fitness is quickly reduced to the lower bound. The creep operators, which are basically controlled mutations, perform much better and could replace the pure mutation operators.

Appendix C

Method of Multiple Scales

In this Appendix we derive soliton solutions of the nonlinear coupled mode equations in Eq. (5.10) by using a multiple scales approach.

C.1 Properties of the linear eigensolutions

Before solving the full nonlinear problem, we recall useful properties of the solutions of the linear system in Eq. (5.31). The eigenvectors of this system \mathbf{A}^\pm in Eq. (5.34) are orthonormal,

$$\begin{aligned}\mathbf{A}^+(k) \cdot \mathbf{A}^+(k) &= \mathbf{A}^-(k) \cdot \mathbf{A}^-(k) = 1, \\ \mathbf{A}^+(k) \cdot \mathbf{A}^-(k) &= \mathbf{A}^-(k) \cdot \mathbf{A}^+(k) = 0.\end{aligned}\tag{C.1}$$

Furthermore, we evaluate the following expressions using the Pauli matrix σ_3 as defined in Section 5.2.1,

$$\mathbf{A}^\pm(k) \cdot \sigma_3 \cdot \mathbf{A}^\pm(k) = \frac{v_R k}{\omega^\pm},\tag{C.2}$$

$$\mathbf{A}^\pm(k) \cdot \sigma_3 \cdot \mathbf{A}^\mp(k) = \mp \frac{V_0}{2\hbar\omega^\pm},\tag{C.3}$$

and the derivatives of the linear dispersion curve

$$\frac{d\omega^\pm}{dk} = \frac{v_R^2 k}{\omega^\pm},\tag{C.4}$$

$$\frac{d^2\omega^\pm}{dk^2} = \frac{v_R^2 V_0^2}{4\hbar^2 (\omega^\pm)^3}.\tag{C.5}$$

C.2 Nonlinear envelope equation

The eigenvectors \mathbf{A}^\pm with eigenenergies ω^\pm solve the linear system in Eq. (5.31) but not the full nonlinear system in Eq. (5.10). We now seek for solutions where the linear solutions are modified by the nonlinearity that is assumed to be weak. The effect of the nonlinearity will be to modulate the linear solutions on different temporal and spatial scales. In order to separate these scales, we use the method of multiple scales, following Ref. [117]. We start by introducing a new set of temporal and spatial variables

$$t_n = \mu^n t, \quad z_n = \mu^n z,\tag{C.6}$$

where $\mu \ll 1$ and $n = 0, 1, \dots$ an integer. Both the t_n and z_n are treated as independent variables. The temporal and spatial derivatives are then written as

$$\frac{\partial}{\partial t} = \sum_{n=0} \mu^n \frac{\partial}{\partial t_n}, \quad (\text{C.7})$$

$$\frac{\partial}{\partial z} = \sum_{n=0} \mu^n \frac{\partial}{\partial z_n}. \quad (\text{C.8})$$

$$(\text{C.9})$$

In order to solve the full nonlinear equation we seek for solutions of the form

$$\begin{aligned} \psi &= \mu \chi_1(z_1, z_2, \dots, t_1, t_2, \dots) \mathbf{A}^- e^{-i(\omega^- t_0 - \tilde{k} z_0)} \\ &+ \mu^2 \chi_2(z_1, z_2, \dots, t_1, t_2, \dots) \mathbf{A}^+ e^{-i(\omega^- t_0 - \tilde{k} z_0)} \\ &+ \mu^3 \chi_3(z_1, z_2, \dots, t_1, t_2, \dots) \mathbf{A}^+ e^{-i(\omega^- t_0 - \tilde{k} z_0)} \\ &+ \mathcal{O}(\mu^4), \end{aligned} \quad (\text{C.10})$$

where \mathbf{A}^\pm and ω^- are understood to be evaluated at $k = \tilde{k}$. Equation (C.10) constructs a wave packet with a central wave vector \tilde{k} that consists of a superposition of the linear solutions. By introducing the envelope functions χ_i we allow the nonlinearity to modulate these linear solutions on spatial and temporal scales. Since we consider the nonlinearity to be weak, these envelopes are expected to be slowly varying. The term of order μ^1 gives the major contribution since $\mu \ll 1$, so ψ is mainly located in the lower energy band of the dispersion curve with small admixtures of the upper band.

We now substitute Eq. (C.10) into the nonlinear system in Eq. (5.10) and identify terms with corresponding powers of μ .

Order μ

For order μ^1 we obtain the equation

$$\left(i \frac{\partial}{\partial t_0} + i v_R \sigma_3 \frac{\partial}{\partial z_0} - \sigma_1 \frac{V_0}{2\hbar} \right) \mathbf{A}^- e^{-i(\omega^- t_0 - \tilde{k} z_0)} = 0, \quad (\text{C.11})$$

which is identically satisfied.

Order μ^2

For order μ^2 we find

$$\left(i \frac{\partial}{\partial t_1} + i v_R \sigma_3 \frac{\partial}{\partial z_1} \right) \chi_1 \mathbf{A}^- + (\omega^- - \omega^+) \chi_2 \mathbf{A}^+ = 0. \quad (\text{C.12})$$

Projecting this equation to the left onto \mathbf{A}^- and using Eqs. (C.1) and (C.2) we obtain

$$\left(\frac{\partial}{\partial t_1} + \frac{v_R^2 \tilde{k}}{\omega^-} \frac{\partial}{\partial z_1} \right) \chi_1 = 0. \quad (\text{C.13})$$

This can be rewritten with help of Eq. (C.4) in terms of the slope of the dispersion curve at $k = \tilde{k}$ as

$$\left(\frac{\partial}{\partial t_1} + \frac{d\omega^-}{dk} \Big|_{\tilde{k}} \frac{\partial}{\partial z_1} \right) \chi_1 = 0. \quad (\text{C.14})$$

Solving this equation leaves us with

$$\chi_1 = \chi_1 \left(z_1 - \frac{d\omega^-}{dk} \Big|_{\bar{k}} t_1, z_1, \dots, t_2, \dots \right). \quad (\text{C.15})$$

To lowest order in μ we obtain an envelope χ_1 of arbitrary shape moving at the group velocity determined by the lower energy band. Projecting Eq. (C.12) to the left onto \mathbf{A}^+ and using Eqs. (C.1) and (C.3) leaves us with a relation between the envelope functions χ_1 and χ_2 ,

$$\chi_2 = -i \frac{v_R V_0}{4\hbar (\omega^-)^2} \frac{\partial}{\partial z_1} \chi_1. \quad (\text{C.16})$$

Order μ^3

Identifying terms of order μ^3 we are left with

$$\begin{aligned} 0 &= \left(i \frac{\partial}{\partial t_2} + i v_R \sigma_3 \frac{\partial}{\partial z_2} \right) \chi_1 \mathbf{A}^- \\ &+ \left(i \frac{\partial}{\partial t_1} + i v_R \sigma_3 \frac{\partial}{\partial z_1} \right) \chi_2 \mathbf{A}^+ \\ &+ (\omega^- - \omega^+) \chi_3 \mathbf{A}^+ \\ &- \frac{NU_0}{2\hbar} \left[3 - \sigma_3 \frac{1}{v_R} \frac{d\omega^-}{dk} \Big|_{\bar{k}} \right] |\chi_1|^2 \chi_1 \mathbf{A}^-. \end{aligned} \quad (\text{C.17})$$

Note that this is the lowest order for nonlinear terms to appear. Projecting this equation to the left onto \mathbf{A}^- and using Eqs. (C.1), (C.2) and (C.3), we get

$$\left[i \frac{\partial}{\partial t_2} + i \frac{d\omega^-}{dk} \Big|_{\bar{k}} \frac{\partial}{\partial z_2} - \frac{g}{\hbar} |\chi_1|^2 \right] \chi_1 + i \frac{v_R V_0}{2\hbar \omega^-} \frac{\partial}{\partial z_1} \chi_2 = 0, \quad (\text{C.18})$$

where the nonlinear interaction strength g is defined as

$$g = \frac{NU_0}{2} \left[3 - \frac{k}{\omega^-} \frac{d\omega^-}{dk} \Big|_{\bar{k}} \right]. \quad (\text{C.19})$$

Again, we rewrite Eq. (C.18) by using the derivatives of the linear dispersion curve, Eqs. (C.4) and (C.5), and the result from Eq. (C.16) to end up with

$$\left[i\hbar \frac{\partial}{\partial t_2} + i\hbar \frac{d\omega^-}{dk} \Big|_{\bar{k}} \frac{\partial}{\partial z_2} + \frac{\hbar}{2} \frac{d^2\omega^-}{dk^2} \Big|_{\bar{k}} \frac{\partial^2}{\partial z_1^2} - g |\chi_1|^2 \right] \chi_1 = 0. \quad (\text{C.20})$$

We now let $\mu \rightarrow 1$ in the usual spirit of perturbation theory and end up with an equation of motion for the envelope function $\chi(z, t)$

$$\left[i\hbar \frac{\partial}{\partial t} + i\hbar v \frac{\partial}{\partial z} + \frac{\hbar^2}{2M^*} \frac{\partial^2}{\partial z^2} - g |\chi_1(z, t)|^2 \right] \chi_1(z, t) = 0. \quad (\text{C.21})$$

Here, we associate the derivatives with the group velocity v and the effective mass M^* according to the definitions in Eqs. (2.67) and (2.69),

$$v = \frac{d\omega^-}{dk} \Big|_{\bar{k}} \quad \text{and} \quad \frac{1}{M^*} = \frac{1}{\hbar} \frac{d^2\omega^-}{dk^2} \Big|_{\bar{k}}. \quad (\text{C.22})$$

C.3 General soliton solution

Equation (C.21) is identical to Eq. (5.1) except the additional term containing the group velocity. As we know from Section 5.1.2, this equation has general bright soliton solutions with the soliton wave function $\chi(z, t)$ and the phase $\phi(z, t)$ given by

$$\begin{aligned}\chi_1(z, t) &= \sqrt{-\frac{M^*v_1^2}{g}} e^{i\phi(z, t)} \operatorname{sech} \left[\frac{M^*v_1}{\hbar} (z - vt - v_2t) \right], \\ \phi(z, t) &= \frac{M^*}{\hbar} \left[v_2(z - vt) - \frac{v_2^2 t}{2} + \frac{v_1^2 t}{2} \right],\end{aligned}\quad (\text{C.23})$$

with the velocity parameters v_1 and v_2 . The parameter v_1 determines the soliton amplitude and width, the combination of v_2 and v determines the soliton velocity. In order to satisfy the slowly varying envelope assumption we rewrite the velocity parameters as $v_1 = \alpha v_R$ and $v_2 = \beta v_R$ with the dimensionless parameters $\alpha, \beta \ll 1$. The bright soliton solution in Eqs. (C.23) only exists if either the nonlinear coefficient or the effective mass is negative, i.e. $gM^* < 0$.

C.4 Stationary soliton solution

For illustration purposes we now focus on the stationary soliton solution, which can be achieved with $v = v_2 = 0$ in Eq. (C.23). At time $t = 0$ we then obtain

$$\chi_1(z, t = 0) = \alpha v_R \sqrt{-\frac{M^*}{g}} \operatorname{sech} \left(\frac{\alpha v_R M^*}{\hbar} z \right). \quad (\text{C.24})$$

The choice $v = 0$ determines \tilde{k} , with the help of Eqs. (C.4) and (C.22) we find

$$v = \left. \frac{d\omega^-}{dk} \right|_{\tilde{k}} = 0 \Rightarrow \tilde{k} = 0. \quad (\text{C.25})$$

The central wave vector \tilde{k} of the stationary soliton wave packet is thus located at the center of the Brillouin zone. We can now evaluate the nonlinear coefficient g and the effective mass M^* at $\tilde{k} = 0$ according to Eqs. (C.19) and (C.22),

$$g = \frac{3NU_0}{2} \quad \text{and} \quad M^* = -\frac{V_0}{2v_R^2}. \quad (\text{C.26})$$

Since we consider repulsive interatomic interactions, i.e. $U_0 > 0$, we have $gM^* < 0$ and the negative effective mass cancels the minus sign under the square root in Eq. (C.24). Since a region of negative effective mass only exists in the lower branch of the dispersion curve we chose the wave function in Eq. (C.10) to be mainly consisting of this branch.

Evaluation of the eigenvector \mathbf{A}^- at $\tilde{k} = 0$ yields

$$\mathbf{A}^- = \frac{1}{\sqrt{2}} \begin{pmatrix} 1 \\ -1 \end{pmatrix}. \quad (\text{C.27})$$

This enables us to write the full stationary soliton solution $\psi(z)$ according to Eq. (C.10) as

$$\begin{aligned}\psi(z, t = 0) &= \chi_1(z, t = 0) \mathbf{A}^- \\ &= \alpha \sqrt{\frac{V_0}{6NU_0}} \operatorname{sech} \left(\frac{V_0 \alpha}{2\hbar v_R} z \right) \begin{pmatrix} 1 \\ -1 \end{pmatrix}.\end{aligned}\quad (\text{C.28})$$

Appendix D

Complete list of publications

- *Atomic Solitons in Optical Lattices*,
S. Pötting, P. Meystre, and E. M. Wright.
In *Nonlinear Photonic Crystals*, edited by R. E. Slusher and B. J. Eggleton
(Springer-Verlag, Heidelberg, 2003).
- *Input-output theory for fermions in an atom cavity*,
C. P. Search, S. Pötting, W. Zhang, and P. Meystre,
Phys. Rev. A **66**, 043616 (2002).
- *Raman coupler for a trapped two-component quantum-degenerate Fermi gas*,
S. Pötting, M. Cramer, W. Zhang, and P. Meystre,
Phys. Rev. A **65**, 063620 (2002).
- *Momentum-state engineering and control in Bose-Einstein condensates*,
S. Pötting, M. Cramer, and P. Meystre,
Phys. Rev. A **64**, 063613 (2001).
- *Coherent acceleration of Bose-Einstein condensates*,
S. Pötting, M. Cramer, C. H. Schwalb, H. Pu, and P. Meystre,
Phys. Rev. A **64**, 023604 (2001).
- *Coherent transport of matter waves*,
C. Henkel and S. Pötting,
Appl. Phys. B **72**, 73 (2001).
- *Quantum coherence and interaction-free measurements*,
S. Pötting, E. S. Lee, W. Schmitt, I. Rumyantsev, B. Mohring, and P. Meystre,
Phys. Rev. A **62**, 060101 (2000).
- *Magneto-optical control of bright atomic solitons*,
S. Pötting, O. Zobay, P. Meystre, and E. M. Wright,
J. Mod. Opt. **47**, 2653 (2000).
- *PbS quantum-dot-doped glasses for ultrashort-pulse generation*,
K. Wundke, S. Pötting, J. Auxier, A. Schülzgen, N. Peyghambarian, and N. F.
Borrelli,
Appl. Phys. Lett. **76**, 10 (2000).
- *Loss and heating of particles in small and noisy traps*,
C. Henkel, S. Pötting, and M. Wilkens,
Appl. Phys. B **69**, 379 (1999).

- *Creation of gap solitons in Bose-Einstein condensates*,
O. Zobay, S. Pötting, P. Meystre, and E. M. Wright,
Phys. Rev. A **59**, 643 (1999).

Bibliography

- [1] O. Morsch, J. H. Müller, M. Cristiani, D. Ciampini, and E. Arimondo, *Phys. Rev. Lett.* **87**, 140402 (2001).
- [2] J. Hecker-Denschlag, J. E. Simsarian, H. Häffner, C. McKenzie, A. Browaeys, D. Cho, K. Helmerson, S. L. Rolston, and W. D. Phillips, *J. Phys. B: At. Mol. Opt. Phys.* **35**, 3095 (2002).
- [3] B. Eiermann, T. Anker, M. Albiez, M. Taglieber, P. Treutlein, K.-P. Marzlin, and M. K. Oberthaler, *Phys. Rev. Lett.* **92**, 230401 (2004).
- [4] L. de Broglie, *Comp. Rend. Ac. Sci.* **177**, 507 (1923).
- [5] M. Wilkens, *De Broglie Optics*. In *Atomic, Molecular and Optical Physics Handbook*, edited by G. W. F. Drake (AIP Press, Woodbury, 1996).
- [6] P. W. Hawkes and E. Kasper, *Principles of Electron Optics* (Academic Press, London, 1989).
- [7] V. F. Sears, *Neutron Optics, Oxford Series on Neutron Scattering in Condensed Matter* (Oxford University Press, Oxford, 1989).
- [8] C. Cohen-Tannoudji, *Atomic Motion in Laser Light*. In *Fundamental Systems in Quantum Optics*, edited by J. Dalibard, J.-M. Raimond, and J. Zinn-Justin (North-Holland, Amsterdam, 1992).
- [9] M. H. Anderson, J. R. Ensher, M. R. Matthews, C. E. Wieman, and E. A. Cornell, *Science* **269**, 198 (1995).
- [10] K. B. Davis, M.-O. Mewes, M. R. Andrews, N. J. van Druten, D. S. Durfee, D. M. Kurn, and W. Ketterle, *Phys. Rev. Lett.* **75**, 3969 (1995).
- [11] C. C. Bradley, C. A. Sackett, J. J. Tollett, and R. G. Hulet, *Phys. Rev. Lett.* **75**, 1687 (1995).
- [12] M. O. Mewes, M. R. Andrews, D. M. Kurn, D. S. Durfee, C. G. Townsend, and W. Ketterle, *Phys. Rev. Lett.* **78**, 582 (1997).
- [13] B. P. Anderson and M. A. Kasevich, *Science* **282**, 1686 (1998).
- [14] E. W. Hagley, L. Deng, M. Kozuma, J. Wen, K. Helmerson, S. L. Rolston, W. D. Phillips, *Science* **283**, 1706 (1999).
- [15] I. Bloch, T. W. Hänsch, and T. Esslinger, *Phys. Rev. Lett.* **82**, 3008 (1999).
- [16] L. Deng, E. W. Hagley, J. Wen, M. Trippenbach, Y. Band, P. S. Julienne, J. E. Simsarian, K. Helmerson, S. L. Rolston, and W. D. Phillips, *Nature* **398**, 218 (1999).

- [17] S. Inouye, T. Pfau, S. Gupta, A. P. Chikkatur, A. Görlitz, D. E. Pritchard, and W. Ketterle, *Nature* **402**, 641 (1999).
- [18] M. Kozuma, Y. Suzuki, Y. Torii, T. Sugiura, T. Kuga, E. W. Hagley, and L. Deng, *Science* **286**, 2309 (1999).
- [19] S. Burger, K. Bongs, S. Dettmer, W. Ertmer, K. Sengstock, A. Sanpera, G. V. Shlyapnikov, and M. Lewenstein, *Phys. Rev. Lett.* **83**, 5198 (1999).
- [20] J. Denschlag, J. E. Simsarian, D. L. Feder, C. W. Clark, L. A. Collins, J. Cubizolles, L. Deng, E. W. Hagley, K. Helmerson, W. P. Reinhardt, S. L. Rolston, B. I. Schneider, and W. D. Phillips, *Science* **287**, 97 (2000).
- [21] S. Inouye, A. P. Chikkatur, D. M. Stamper-Kurn, J. Stenger, D. E. Pritchard, and W. Ketterle, *Science* **285**, 571 (1999).
- [22] *Atom Interferometry*, edited by P. R. Berman (Academic Press, San Diego, 1997).
- [23] D. Müller, D. Z. Anderson, R. J. Grow, P. D. D. Schwindt, and E. A. Cornell, *Phys. Rev. Lett.* **83**, 5194 (1999).
- [24] N. H. Dekker, C. S. Lee, V. Lorent, J. H. Thywissen, S. P. Smith, M. Drndic, R. M. Westervelt, and M. Prentiss, *Phys. Rev. Lett.* **84**, 1124 (2000).
- [25] W. Hänsel, J. Reichel, P. Hommelhoff, and T. W. Hänsch, *Phys. Rev. Lett.* **86**, 608 (2001).
- [26] W. Hänsel, P. Hommelhoff, T. W. Hänsch, and J. Reichel, *Nature* **413**, 498 (2001).
- [27] H. Ott, J. Fortagh, G. Schlotterbeck, A. Grossmann, and C. Zimmermann, *Phys. Rev. Lett.* **87**, 230401 (2001).
- [28] J. Fujita, S. Mitake, and F. Shimizu, *Phys. Rev. Lett.* **84**, 4027 (2000).
- [29] A. Soroko, *J. Phys. B: At. Mol. Opt. Phys.* **30**, 5621 (1997).
- [30] O. Zobay, E. V. Goldstein, and P. Meystre, *Phys. Rev. A* **60**, 3999 (1999).
- [31] D. Jaksch, H. J. Briegel, J. I. Cirac, C. W. Gardiner, and P. Zoller, *Phys. Rev. Lett.* **82**, 1975 (1999).
- [32] O. Mandel, M. Greiner, A. Widera, T. Rom, T. W. Hänsch, and I. Bloch, *Nature* **425**, 937 (2003).
- [33] H. M. Wiseman and M. J. Collett, *Phys. Lett. A* **202**, 246 (1995).
- [34] R. J. C. Spreeuw, T. Pfau, U. Janicke, and M. Wilkens, *Europhys. Lett.* **32**, 469 (1995).
- [35] M. Olshani, Y. Castin, and J. Dalibard, *A model for an atom laser*. In *Proceedings of the 12th International Conference on Laser Spectroscopy*, edited by M. Inguscio, M. Allegrini, and A. Lasso (World Scientific, Singapore, 1995).
- [36] P. Meystre, *Atom Optics* (Springer-Verlag, New York, 2001).
- [37] R. J. Glauber, *Phys. Rev.* **130**, 2529 (1963).
- [38] I. Bloch, T. W. Hänsch, and T. Esslinger, *Nature* **403**, 166 (2000).

- [39] T. Esslinger, I. Bloch, M. Greiner, and T. W. Hänsch, *Generating and Manipulating Atom Laser Beams*. In *Bose Einstein Condensates and Atom Lasers*, edited by S. Martellucci, A. N. Chester, A. Aspect, and M. Inguscio (Kluwer, Dordrecht, 2000).
- [40] A. P. Chikkatur, Y. Shin, A. E. Leanhardt, D. Kielpinski, E. Tsikata, T. L. Gustavson, D. E. Pritchard, and W. Ketterle, *Science* **296**, 2193 (2002).
- [41] M. A. Olshanii, Y. B. Ovchinnikov, and V. S. Letokhov, *Opt. Comm.* **98**, 77 (1993).
- [42] S. Marksteiner, C. M. Savage, P. Zoller, and S. L. Rolston, *Phys. Rev. A* **50**, 2680 (1994).
- [43] M. J. Renn, D. Montgomery, O. Vdovin, D. Z. Anderson, C. E. Wieman, and E. A. Cornell, *Phys. Rev. Lett.* **75**, 3253 (1995).
- [44] M. J. Renn, E. A. Donley, E. A. Cornell, C. E. Wieman, and D. Z. Anderson, *Phys. Rev. A* **53**, R648 (1996).
- [45] H. Ito, T. Nakata, K. Sakaki, M. Ohtsu, K. I. Lee, and W. Jhe, *Phys. Rev. Lett.* **76**, 4500 (1996).
- [46] D. Müller, E. A. Cornell, D. Z. Anderson, and E. R. I. Abraham, *Phys. Rev. A* **61**, 033411 (2000).
- [47] M. Key, I. G. Hughes, W. Rooijackers, B. E. Sauer, E. A. Hinds, D. J. Richardson, and P. G. Kazansky, *Phys. Rev. Lett.* **84**, 1371 (2000).
- [48] J. Reichel, *Appl. Phys. B* **74**, 469 (2002).
- [49] C. Henkel and M. Wilkens, *Europhys. Lett.* **47**, 414 (1999).
- [50] A. E. Leanhardt, Y. Shin, A. P. Chikkatur, D. Kielpinski, W. Ketterle, and D. E. Pritchard, *Phys. Rev. Lett.* **90**, 100404 (2003).
- [51] C. Henkel, S. Pötting, and M. Wilkens, *Appl. Phys. B* **69**, 379 (1999).
- [52] P. Treutlein, P. Hommelhoff, T. Steinmetz, T. W. Hänsch, and J. Reichel, *Phys. Rev. Lett.* **92**, 203005 (2004).
- [53] P. Treutlein, P. Hommelhoff, T. Steinmetz, T. W. Hänsch, and J. Reichel, *Phys. Rev. Lett.* **93**, 219904 (2004).
- [54] M. D. Girardeau and E. M. Wright, *Phys. Rev. Lett.* **84**, 5691 (2000).
- [55] M. D. Girardeau and E. M. Wright, *Phys. Rev. Lett.* **87**, 210401 (2001).
- [56] J. Reichel and J. H. Thywissen, *J. Phys. IV France* **116**, 265 (2004).
- [57] C. R. Pollock, *Fundamentals of Optoelectronics* (Irwin, Chicago, 1995).
- [58] T. L. Gustavson, P. Bouyer, and M. A. Kasevich, *Phys. Rev. Lett.* **78**, 2046 (1997).
- [59] M. J. Snadden, J. M. McGuirk, P. Bouyer, K. G. Haritos, and M. A. Kasevich, *Phys. Rev. Lett.* **81**, 971 (1998).
- [60] M. B. Dahan, E. Peik, J. Reichel, Y. Castin, and C. Salomon, *Phys. Rev. Lett.* **76**, 4508 (1996).

- [61] E. Peik, M. Ben Dahan, I. Bouchoule, Y. Castin, and C. Salomon, *Appl. Phys. B* **65**, 685 (1997).
- [62] E. Peik, M. B. Dahan, I. Bouchoule, Y. Castin, and C. Salomon, *Phys. Rev. A* **55**, 2989 (1997).
- [63] C. F. Bharucha, K. W. Madison, P. R. Morrow, S. R. Wilkinson, B. Sundaram, and M. G. Raizen, *Phys. Rev. A* **55**, R857 (1997).
- [64] S. R. Wilkinson, C. F. Bharucha, K. W. Madison, Q. Niu, and M. G. Raizen, *Phys. Rev. Lett.* **76**, 4512 (1996).
- [65] K. W. Madison, C. F. Bharucha, P. R. Morrow, S. R. Wilkinson, Q. Niu, B. Sundaram, and M. G. Raizen, *Appl. Phys. B* **65**, 693 (1997).
- [66] O. Morsch and E. Arimondo, *Ultracold atoms and Bose-Einstein condensates in optical lattices*. In *Lecture Notes in Physics, Dynamics and Thermodynamics of Systems with Long-Range Interactions: An Introduction*, edited by T. Dauxois, S. Ruffo, E. Arimondo, and M. Wilkens (Springer-Verlag, Heidelberg, 2002).
- [67] D. S. Jin, J. R. Ensher, M. R. Matthews, C. E. Wieman, and E. A. Cornell, *Phys. Rev. Lett.* **77**, 420 (1996).
- [68] D. S. Jin, M. R. Matthews, J. R. Ensher, C. E. Wieman, and E. A. Cornell, *Phys. Rev. Lett.* **78**, 764 (1997).
- [69] L. Dobrek, M. Gajda, M. Lewenstein, K. Sengstock, G. Birkl, and W. Ertmer, *Phys. Rev. A* **60**, R3381 (1999).
- [70] K. E. Strecker, G. B. Partridge, A. G. Truscott, and R. G. Hulet, *Nature* **417**, 150 (2002).
- [71] L. Khaykovich, F. Schreck, G. Ferrari, T. Bourdel, J. Cubizolles, L. D. Carr, Y. Castin, and C. Salomon, *Science* **296**, 1290 (2002).
- [72] C. J. Pethick and H. Smith, *Bose-Einstein Condensation in Dilute Gases* (Cambridge University Press, Cambridge, 2002).
- [73] F. Bloch, *Z. Phys.* **52**, 555 (1928).
- [74] C. Zener, *Proc. R. Soc. London A* **145**, 523 (1934).
- [75] N. W. Ashcroft and N. D. Mermin, *Solid State Physics* (Saunders College Publishing, Orlando, 1976).
- [76] L. D. Landau and E. M. Lifschitz, *Quantum Mechanics*. Vol. 3, third (reprint) edition of *Course of Theoretical Physics* (Pergamon Press, New York, 1991).
- [77] J. D. Morgan III, *Thomas-Fermi and Other Density-Functional Theories*. In *Atomic, Molecular, and Optical Physics Handbook*, edited by G. W. F. Drake (AIP Press, Woodbury, 1966).
- [78] F. Dalfovo, L. Pitaevskii, and S. Stringari, *Phys. Rev. A* **54**, 4213 (1996).
- [79] M. E. Peskin and D. V. Schroeder, *An Introduction to Quantum Field Theory* (Westview Press, Boulder, 1995).
- [80] D. M. Stamper-Kurn, M. R. Andrews, A. P. Chikkatur, S. Inouye, H.-J. Miesner, J. Stenger, and W. Ketterle, *Phys. Rev. Lett.* **80**, 2027 (1998).

- [81] P. W. Milonni and J. H. Eberly, *Lasers* (Wiley, New York, 1988).
- [82] R. L. Liboff, *Introductory Quantum Mechanics* (Addison-Wesley, Boston, 1992).
- [83] H. Pu, L. O. Baksmaty, W. Zhang, N. P. Bigelow, and P. Meystre, *Phys. Rev. A* **67**, 043605 (2003).
- [84] P. Treutlein, *Dispersionsmanagement für Materiewellen*, Diplomarbeit, Universität Konstanz (2002).
- [85] B. Eiermann, P. Treutlein, T. Anker, M. Albiez, M. Taglieber, K. P. Marzlin, and M. K. Oberthaler, *Phys. Rev. Lett.* **91**, 060402 (2003).
- [86] A. Messiah, *Quantum Mechanics*, Vol. 2 (North-Holland, Amsterdam, 1962).
- [87] K.-P. Marzlin and J. Audretsch, *Europhys. Lett.* **36**, 43 (1996).
- [88] Q. Niu, X.-G. Zhao, G. A. Georgakis, and M. G. Raizen, *Phys. Rev. Lett.* **76**, 4504 (1996).
- [89] J. Zapata, A. M. Guzmán, M. G. Moore, and P. Meystre, *Phys. Rev. A* **63**, 023607 (2001).
- [90] W. H. Oskay, D. A. Steck, B. G. Klappauf, and M. G. Raizen, *Laser Phys.* **9**, 265 (1999).
- [91] D. L. Haycock, P. M. Alsing, I. H. Deutsch, J. Grondalski, and P. S. Jessen, *Phys. Rev. Lett.* **85**, 3365 (2000).
- [92] K. Berg-Sørensen and K. Mølmer, *Phys. Rev. A* **58**, 1480 (1998).
- [93] D. Choi and Q. Niu, *Phys. Rev. Lett.* **82**, 2022 (1999).
- [94] J. Stenger, S. Inouye, A. P. Chikkatur, D. M. Stamper-Kurn, D. E. Pritchard, and W. Ketterle, *Phys. Rev. Lett.* **82**, 4569 (1999).
- [95] E. W. Hagley, L. Deng, M. Kozuma, M. Trippenbach, Y. B. Band, M. Edwards, M. Doery, P. S. Julienne, K. Helmerson, S. L. Rolston, and W. D. Phillips, *Phys. Rev. Lett.* **83**, 3112 (1999).
- [96] E. V. Goldstein and P. Meystre, *Phys. Rev. A* **59**, 3896 (1999).
- [97] M. Trippenbach, Y. B. Band, P. S. Julienne, *Phys. Rev. A* **62**, 023608 (2000).
- [98] D. Jaksch, C. Bruder, J. I. Cirac, C. W. Gardiner, and P. Zoller, *Phys. Rev. Lett.* **81**, 3108 (1998).
- [99] M. Greiner, O. Mandel, T. Esslinger, T. W. Hänsch, and I. Bloch, *Nature* **415**, 39 (2002).
- [100] P. B. Blakie and R. J. Ballagh, *J. Phys. B: At. Mol. Opt. Phys.* **33**, 3961 (2000).
- [101] S. Pötting, M. Cramer, C. H. Schwalb, H. Pu, and P. Meystre, *Phys. Rev. A* **64**, 023604 (2001).
- [102] L. Ed. Davis, *Handbook of Genetic Algorithms* (Van Nostrand Reinhold, New York, 1991).
- [103] D. A. Coley, *An Introduction to Genetic Algorithms for Scientists and Engineers* (World Scientific, Singapore, 1999).

- [104] R. S. Judson and H. Rabitz, *Phys. Rev. Lett.* **68**, 1500 (1992).
- [105] T. C. Weinacht, J. Ahn, P. H. Bucksbaum, *Nature* **397**, 233 (1999).
- [106] H. Rabitz, R. de Vivie-Riedle, M. Motzkus, and K. Kompa, *Science* **288**, 824 (2000).
- [107] T. Hornung, M. Motzkus, and R. de Vivie-Riedle, *J. Chem. Phys.* **115**, 3105 (2001).
- [108] J. W. Nicholson, F. G. Omenetto, D. J. Funk, and A. J. Taylor, *Opt. Lett.* **24**, 490 (1999).
- [109] J. E. Simsarian, J. Denschlag, M. Edwards, C. W. Clark, L. Deng, E. W. Hagley, K. Helmerson, S. L. Rolston, and W. D. Phillips, *Phys. Rev. Lett.* **85**, 2040 (2000).
- [110] M. Kozuma, L. Deng, E. W. Hagley, J. Wen, R. Lutwak, K. Helmerson, S. L. Rolston, and W. D. Phillips, *Phys. Rev. Lett.* **82**, 871 (1999).
- [111] B. J. Pearson, J. L. White, T. C. Weinacht, and P. H. Bucksbaum, *Phys. Rev. A* **63**, 063412 (2001).
- [112] A. C. Scott, F. Y. F. Chu, and D. W. McLaughlin, *Proc. IEEE* **61**, 1443 (1973).
- [113] G. P. Agrawal, *Nonlinear Fiber Optics* (Academic Press, San Diego, 1995).
- [114] C. C. Bradley, C. A. Sackett, and R. G. Hulet, *Phys. Rev. Lett.* **78**, 985 (1997).
- [115] W. Chen and D. L. Mills, *Phys. Rev. Lett.* **58**, 160 (1987).
- [116] D. N. Christodoulides and R. I. Joseph, *Phys. Rev. Lett.* **62**, 1746 (1989).
- [117] C. M. de Sterke and J. E. Sipe, *Gap Solitons*. In *Progress in Optics*, Vol. XXXIII, edited by E. Wolf (Elsevier, Amsterdam, 1994).
- [118] B. J. Eggleton, R. E. Slusher, C. M. de Sterke, P. A. Krug, and J. E. Sipe, *Phys. Rev. Lett.* **76**, 1627 (1996).
- [119] S. Pötting, *Gap Solitons in Atomic Bose-Einstein Condensates*, Master thesis, University of Arizona (1998).
- [120] O. Zobay, S. Pötting, P. Meystre, and E. M. Wright, *Phys. Rev. A* **59**, 643 (1999).
- [121] W. P. Reinhardt and C. W. Clark, *J. Phys. B: At. Mol. Opt. Phys.* **30**, L785 (1997).
- [122] R. Dum, J. I. Cirac, M. Lewenstein, and P. Zoller, *Phys. Rev. Lett.* **80**, 2972 (1998).
- [123] P. O. Fedichev, A. E. Muryshev, and G. V. Shlyapnikov, *Phys. Rev. A* **60**, 3220 (1999).
- [124] T. Busch and J. R. Anglin, *Phys. Rev. Lett.* **84**, 2298 (2000).
- [125] J. L. Roberts, N. R. Claussen, J. P. Burke, Jr., C. H. Greene, E. A. Cornell, and C. E. Wieman, *Phys. Rev. Lett.* **81**, 5109 (1998).

- [126] S. Inouye, M. R. Andrews, J. Stenger, H.-J. Miesner, D. M. Stamper-Kurn, and W. Ketterle, *Nature* **392**, 151 (1998).
- [127] S. L. Cornish, N. R. Claussen, J. L. Roberts, E. A. Cornell, and C. E. Wieman, *Phys. Rev. Lett.* **85**, 1795 (2000).
- [128] Y. S. Kivshar and T. J. Alexander, *Trapped Bose–Einstein Condensates: Role of Dimensionality*. In *Proceedings of the APCTP-Nankai Symposium on Yang-Baxter Systems, Nonlinear Models and Their Applications*, edited by Q-H. Park *et al.* (World Scientific, Singapore, 1999).
- [129] G. Lenz, P. Meystre, E. M. Wright, *Phys. Rev. Lett.* **71**, 3271 (1993).
- [130] G. Lenz, P. Meystre, E. M. Wright, *Phys. Rev. A* **50**, 1681 (1994).
- [131] M. J. Steel and W. Zhang, *Bloch function description of a Bose–Einstein condensate in a finite optical lattice*, eprint cond-mat/9810284 (1998).
- [132] S. Pötting, P. Meystre, and E. M. Wright, *Atomic Solitons in Optical Lattices*. In *Nonlinear Photonic Crystals*, edited by R. E. Slusher and B. J. Eggleton (Springer-Verlag, Heidelberg, 2003).
- [133] S. Pötting, O. Zobay, P. Meystre, and E. M. Wright, *J. Mod. Opt.* **47**, 2653 (2000).
- [134] A. Trombettoni and A. Smerzi, *Phys. Rev. Lett.* **86**, 2353 (2001).
- [135] I. Carusotto, D. Embriaco, and G. C. La Rocca, *Phys. Rev. A* **65**, 053611 (2002).
- [136] R. G. Scott, A. M. Martin, T. M. Fromhold, S. Bujkiewicz, F. W. Sheard, and M. Leadbeater, *Phys. Rev. Lett.* **90**, 110404 (2003).
- [137] A. B. Aceves and S. Wabnitz, *Phys. Lett. A* **141**, 37 (1989).
- [138] D. J. Kaup and A. C. Newell, *Lett. Nuovo Cim.* **20**, 325 (1977).
- [139] *Optical Solitons*, edited by J. R. Taylor (Cambridge University Press, Cambridge, 1992).
- [140] K. M. Hilligsøe, M. K. Oberthaler, and K.-P. Marzlin, *Phys. Rev. A* **66**, 063605 (2002).
- [141] B. DeMarco and D. S. Jin, *Science* **285**, 1703 (1999).
- [142] B. DeMarco, S. B. Papp, and D. S. Jin, *Phys. Rev. Lett.* **86**, 5409 (2001).
- [143] A. G. Truscott, K. E. Strecker, W. I. McAlexander, G. B. Partridge, and R. G. Hulet, *Science* **291**, 2570 (2001).
- [144] F. Schreck, L. Khaykovich, K. L. Corwin, G. Ferrari, T. Bourdel, J. Cubizolles, and C. Salomon, *Phys. Rev. Lett.* **87**, 080403 (2001).
- [145] F. Schreck, G. Ferrari, K. L. Corwin, J. Cubizolles, L. Khaykovich, M.-O. Mewes, and C. Salomon, *Phys. Rev. A* **64**, 011402(R) (2001).
- [146] M. J. Holland, B. DeMarco, and D. S. Jin, *Phys. Rev. A* **61**, 053610 (2000).
- [147] C. A. Regal, M. Greiner, and D. S. Jin, *Phys. Rev. Lett.* **92**, 040403 (2004).
- [148] K. M. O’Hara, S. L. Hemmer, M. E. Gehm, S. R. Granade, and J. E. Thomas, *Science* **298**, 2179 (2002).

- [149] Z. Hadzibabic, S. Gupta, C. A. Stan, C. H. Schunck, M. W. Zwierlein, K. Dieckmann, and W. Ketterle, *Phys. Rev. Lett.* **91**, 160401 (2003).
- [150] K. E. Strecker, G. B. Partridge, and R. G. Hulet, *Phys. Rev. Lett.* **91**, 080406 (2003).
- [151] C. A. Regal, C. Ticknor, J. L. Bohn, and D. S. Jin, *Phys. Rev. Lett.* **90**, 053201 (2003).
- [152] C. A. Regal and D. S. Jin, *Phys. Rev. Lett.* **90**, 230404 (2003).
- [153] J. Bardeen, L. N. Cooper, and J. R. Schrieffer, *Phys. Rev.* **108**, 1175 (1957).
- [154] H. T. C. Stoof, M. Houbiers, C. A. Sackett, and R. G. Hulet, *Phys. Rev. Lett.* **76**, 10 (1996).
- [155] M. Houbiers, R. Ferwerda, H. T. C. Stoof, W. I. McAlexander, C. A. Sackett, and R. G. Hulet, *Phys. Rev. A* **56**, 4864 (1997).
- [156] G. Bruun, Y. Castin, R. Dum, and K. Burnett, *Eur. Phys. J. D* **7**, 433 (1999).
- [157] L. You and M. Marinescu, *Phys. Rev. A* **60**, 2324 (1999).
- [158] M. A. Baranov, *JETP Lett.* **64**, 301 (1996).
- [159] E. Timmermans, K. Furuya, P. W. Milonni, and A. K. Kerman, *Phys. Lett. A* **285**, 228 (2001).
- [160] M. Holland, S. J. J. M. F. Kokkelmans, M. L. Chiofalo, and R. Walser, *Phys. Rev. Lett.* **87**, 120406 (2001).
- [161] C. A. Regal, M. Greiner, and D. S. Jin, *Phys. Rev. Lett.* **92**, 083201 (2004).
- [162] C. A. Regal, C. Ticknor, J. L. Bohn, and D. S. Jin, *Nature* **424**, 47 (2003).
- [163] M. Greiner, C. A. Regal, and D. S. Jin, *Nature* **426**, 537 (2003).
- [164] S. Jochim, M. Bartenstein, A. Altmeyer, G. Hendl, S. Riedl, C. Chin, J. Hecker-Denschlag, and R. Grimm, *Science* **302**, 2101 (2003).
- [165] M. W. Zwierlein, C. A. Stan, C. H. Schunck, S. M. F. Raupach, S. Gupta, Z. Hadzibabic, and W. Ketterle, *Phys. Rev. Lett.* **91**, 250401 (2003).
- [166] M. W. Zwierlein, C. A. Stan, C. H. Schunck, S. M. F. Raupach, A. J. Kerman, and W. Ketterle, *Phys. Rev. Lett.* **92**, 120403 (2004).
- [167] F. W. Cummings, *Phys. Rev.* **140**, A1051 (1965).
- [168] A. L. Fetter and J. D. Walecka, *Quantum theory of many-particle systems* (McGraw-Hill, San Francisco, 1971).
- [169] S. M. Jensen, *IEEE Journal of Quantum Electronics* **QE-18**, 1580 (1982).
- [170] K. J. Schernthanner, G. Lenz, and P. Meystre, *Phys. Rev. A* **51**, 3121 (1995).
- [171] S. E. Sklarz and D. J. Tannor, *Phys. Rev. A* **66**, 053619 (2002).
- [172] Z. Murtha and H. Rabitz, *Eur. Phys. J. D* **14**, 141 (2001).
- [173] J. C. Strikwerda, *Finite Difference Schemes and Partial Differential Equations* (Wadsworth & Brooks, Belmont, 1989).
- [174] H. Pu and N. P. Bigelow, *Phys. Rev. Lett.* **80**, 1130 (1998).

- [175] W. H. Press, S. A. Teukolsky, W. T. Vetterling, and B. P. Flannery, *Numerical Recipes in C*, second edition (Cambridge University Press, Cambridge, 1999).
- [176] P. B. Blakie, *Optical Manipulation of Bose-Einstein Condensates*, PhD thesis, University of Otago (2001).

Curriculum vitae

Persönliche Angaben

Name	Sierk Pötting
Geburtstag	19. Januar 1973
Geburtsort	Salzkotten
Familienstand	Ledig
Staatsangehörigkeit	Deutsch

Ausbildung

1979 - 1983	Grundschule Josefschule, Paderborn
1983 - 1992	Gymnasium Schloss Neuhaus, Paderborn
Juni 1992	Abitur
1992 - 1993	Zivildienst (Rettungssanitäter, Freiwillige Feuerwehr Paderborn)
1993 - 1996	Studium Physik und Informatik, Eberhard-Karls Universität, Tübingen
1996	Vordiplom Physik und Informatik
1996 - 1998	Studium Optical Sciences, University of Arizona, Tucson (USA)
Dezember 1998	M.S. Optical Sciences
2000 - 2004	Promotion Physik, Ludwig-Maximilians Universität, München
Dezember 2004	Mündliche Prüfung Promotion Physik

Stipendien/Auszeichnungen

1994 - 1998	Stipendiat der Studienstiftung des deutschen Volkes
1998	Rolyn Optics Teaching Award
2000 - 2002	Research Scholar, University of Arizona, Tucson (USA)

Berufserfahrung

Seit 2003	Unternehmensberater bei McKinsey & Company, München
-----------	---

Acknowledgments

I would like to thank everybody who contributed to this dissertation.

Above all, I want to express my gratitude to both my advisors, Prof. Herbert Walther as well as Prof. Pierre Meystre. They both allowed me to benefit from the internationalization of the physics community by working on my thesis in two very different parts of the world - Munich and Tucson. For this unique opportunity and the outrageous support during the time of my dissertation work I want to thank both of them.

When in Germany, I enjoyed my stays at the Max-Planck Institute in Prof. Walther's group very much, being able to talk to many scientists in the German community. And - for a theorist even more important - I was invited to visit many interesting labs and was thus able to learn about the subtleties an experimentalist has to cope with. In Tucson, I experienced an open and adventurous group of theorists. Pierre Meystre always had an open door and an open ear for my thoughts and concerns. It was his persuasion ability that made me return to Tucson - a step I will never forget! Thanks for talking me into going back to Tucson and thanks for being a great mentor and friend!

During my research I gathered many impressions, thoughts, and developed ideas because of the many stimulating people I met. Let me try to name as many as possible: I would like to thank Ewan Wright for all the chats we had and the ideas we were jotting down on his whiteboard. Also, I learned from many discussions with various postdocs - in Tucson these were Mike Moore, Han Pu, Chris Search, and Weiping Zhang, in Munich I enjoyed talking to Almut Beige, Jiannis Pachos, and Pepijn Pinkse. Thanks for being there and helping me with so many questions and discussing so many things. Furthermore, I am glad that so many experimentalists gave me the opportunity to tour their labs and ask the typical theorist's question: "Is it actually possible to ...?". Especially, I would like to name the groups of Poul Jessen, Brian Anderson, Gerhard Rempe, Theodor Hänsch, and Jakob Reichel.

Special credits go to Jerry Moloney for letting me use his Silicon Graphics supercomputer. Without this computational power I would not have finished in time with the chapter on fermions. Furthermore, it was a pleasure to work with Martin Wilkens on several occasions in Tucson and in Potsdam and in Florence with Sven Burger and Massimo Inguscio, who revived my soliton research.

I am very glad that I was always able to count on my friends Marcus Cramer and John Lapeyre - I spent many hours inside and outside the *Gedanken Laboratory* together with them, discussing everything from physics to life in general. This being said, it is only natural to thank at this point the *Cafe Paraiso* for the continuous supply of coffee and *The Shelter* for providing the occasional drink.

I wish to thank my parents Renate and Werner Pötting for their continuous support - thanks for trusting me and for always being there for me. Lastly, I want to thank Marion Becker for the time we spent together and for all the energy that she also put into this dissertation.